The implementation of glaciation-induced rotational behavior of the Earth in a numerical model

AE5810/AESM2640 Master Thesis

M.F.M. Weerdesteijn

TU Delft

The implementation of glaciation-induced rotational behavior of the Earth in a numerical model

AE5810/AESM2640 Master Thesis

by

M.F.M. Weerdesteijn

to obtain the degree of Master of Science
at the Delft University of Technology,
to be defended publicly on Thursday January 31, 2019 at 13:30 PM.

Student number:	4157427	
Project duration:	April 16, 2018 – January 31, 2018	
Thesis committee:	Prof. Dr. L. L. A. Vermeersen,	TU Delft, chair
	Assoc. Prof. Dr. W. van der Wal,	TU Delft, supervisor
	Ass. Prof. Dr. R. E. M. Riva,	TU Delft, supervisor
	Dr. J. M. J. F. van Campen,	TU Delft

Cover: a color image of the Earth created from MODIS data, obtained from NASA.

An electronic version of this thesis is available at `http://repository.tudelft.nl/`.

TU Delft

Preface

This report concludes the work done on my MSc Thesis entitled "The implementation of glaciation-induced rotational behavior of the Earth in a numerical model" at Delft University of Technology. Performing this research has been a challenge, but also rewarding. I would like to thank my thesis supervisors, Wouter and Riccardo, for their guidance and support. Your expertise and confidence in this research were very important to me for making this research into a success. I would also like to thank the PhD candidates, Haiyang and Bas, in the room across for taking the time to answer any of my questions. Haiyang for explaining the rotational behavior of planetary bodies and for providing me with his ideas on the polar wander implementation, and Bas for explaining choices made on the model generation in the current FE model.

This report also marks the end of my time in Delft as a student. I have tried to extend my stay by taking up two Master's, but now the time has come for new challenges. I have learned much along the way, in terms of life experience and expanding my knowledge. I would like to thank all the people whom I share great memories with: I wouldn't have wanted to miss a single minute.

I would also like to thank my family and in particular my parents. You have taught me to follow my dreams. You have always supported my decisions, even though in hindsight some of those sound ridiculously dangerous from a parents' perspective, and when I needed it the most you steered me in the right direction. I don't know where the road will take me, but I hope to stay close to family and friends, wherever that may be.

M.F.M. Weerdesteijn
Delft, January 2019

Summary

Mass redistribution on the Earth's surface and inside the Earth causes the Earth's gravity field to change. Gravimetry observations include the Earth's deformation due to glacial isostatic adjustment (GIA), which is a response to changes in ice mass distribution over a period from the late Pleistocene up to present. The gravimetry observations need to be corrected for the ongoing GIA-induced deformation of the solid Earth for the present-day mass changes to be revealed, which are of importance for climate change studies on for example ice mass losses and sea level rise. The $C_{2,1}$ and $C_{2,-1}$ spherical harmonic coefficients of the mass change signal are affected by true polar wander (TPW), the secular drift of the position of the Earth's rotational axis with respect to the Earth's surface. Current GIA models give a wide range in corrections for the $C_{2,1}$ and $C_{2,-1}$ spherical harmonic coefficients. A realistic range for these coefficients for GIA models, based on realistic Earth viscosity profiles, lithospheric characteristics, and ice loading histories would lead to more consistent GIA models, and thus to more consistent determination of present-day mass change signals.

The rotational state of the Earth and its interior are closely related. A mass redistribution on the rotating body will break the balance between the centrifugal force and the self-gravitational force. To conserve angular momentum the rotational axis moves in the direction of the axis of maximum moment of inertia. Simultaneously, since the Earth is not spherical, the equatorial bulge readjusts to the position perpendicular to the rotational axis. The deformation of the body induced by the mass redistribution depends on the local viscosity. On the other hand, the equatorial bulge readjustment is dependent on the average global viscosity. Therefore, lateral viscosity variations could play a role in GIA-induced TPW. When heterogeneity is taken into account the resulting deformation cannot be solved analytically. Numerical methods such as the finite element method (FEM) are required to model the Earth's response to loading. The goal is to extend an existing GIA model based on FEM (Wu, 2004; Wu and Wang, 2006) with a simulation for TPW, using state-of-the-art rotational theory (Hu et al., 2017a; Wu and Peltier, 1984).

The TPW algorithm implemented is based on the assumption that during the process of TPW the equatorial bulge readjustment is fast enough, such that the equatorial bulge is always nearly perpendicular to the rotational axis. In that case the linearized Liouville equation can be used by using coordinate transformations for each time step. This method allows for large angle TPW and takes into account non-stationary surface loads with respect to the rotational axis. The model is based on FE software `Abaqus` coupled to the solution of the Laplace equation. The perturbed gravitational potential is a function of the radial displacements. Therefore, an iterative process is required to solve for the displacements in the body. The GIA model, which is expanded with TPW, functions such that the iterations for the radial displacements and perturbed gravitational potential occur over all time steps simultaneously.

It is shown that this model performs well solely for deformation due to a surface load on a non-rotating Earth and due to a change in centrifugal force from a forced movement of the rotational axis. Resemblance with analytical solutions improve for finer mesh resolutions. In the spin-up phase the flattening of the Earth is simulated by applying a centrifugal force for a long-enough duration. It is found that after hydrostatic equilibrium, over a period representing the glaciation history, the change in moment of inertia is negligible compared to the numerical error. The numerical error propagates to the determination of TPW. It is also shown that the TPW solution depends on the accuracy of the change in moment of inertia around the principal axes.

Regarding the TPW implementation, it is found that including the change in the rotational rate per time step is a crucial step for the TPW solution to converge over the iterations in the FE analysis. The new rotational vector needs to be normalized using the new rotational rate. Furthermore, it is found that when the perturbed gravitational potential in the spin-up phase is not fully converged, it affects the perturbed gravitational potential in future time steps and thus TPW. Moreover, when a surface ice load is applied to the model, TPW is triggered. The centrifugal potential changes based on the new position of the rotational axis, and this also affects the perturbed gravitational potential for the following time steps. As a result, the iteration for the perturbed gravitational potential and centrifugal potential cannot occur over all time steps simultaneously using this TPW approach. To be able to study the effect of lateral viscosity variations on GIA-induced TPW, this iteration needs to occur per time step. With an adjusted model based on this finding the ability to perform further research on the implementation of TPW in a numerical model would much improve.

Contents

List of Figures ix

List of Tables xiii

1 Introduction 1
- 1.1 Deformation behavior of the Earth . . . 1
- 1.2 Rotational behavior of the Earth . . . 2
- 1.3 Need for numerical modeling . . . 4
- 1.4 Research objective and research questions . . . 6

2 Finite element method and model 9
- 2.1 Finite element method . . . 9
- 2.2 Modified stiffness equation . . . 9
- 2.3 Boundary conditions . . . 10
  - 2.3.1 Earth's surface . . . 10
  - 2.3.2 Solid-solid internal boundaries . . . 11
  - 2.3.3 Core-mantle boundary . . . 11
  - 2.3.4 Complete set of boundary conditions . . . 12

3 Model definition and generation 13
- 3.1 Model definition . . . 13
  - 3.1.1 Model data . . . 13
  - 3.1.2 Model options . . . 14
- 3.2 Model generation . . . 16
  - 3.2.1 Layer parts creation . . . 16
  - 3.2.2 Viscoelastic material definition . . . 17
  - 3.2.3 Assembly and mesh generation . . . 17
  - 3.2.4 Viscoelastic time step definition . . . 19
  - 3.2.5 Winkler foundation application . . . 20
  - 3.2.6 Pressure application from centrifugal potential . . . 20
  - 3.2.7 Pressure application from input surface load . . . 21
  - 3.2.8 Analysis job definition . . . 24

4 Coupling of FE model to Laplace equation 25
- 4.1 Grid of radial displacements from FE analysis output . . . 25
  - 4.1.1 Radial displacements at layer surfaces . . . 26
  - 4.1.2 Grid of radial displacements in local coordinate system . . . 26
- 4.2 Change in moment of inertia from radial displacements . . . 27
- 4.3 Solution to the Laplace equation . . . 28
- 4.4 Iterative process . . . 29
  - 4.4.1 Schematic overview iterative process . . . 30
  - 4.4.2 Inclusion of the sea level equation . . . 30
  - 4.4.3 Pressure from perturbed gravitational potential . . . 31
- 4.5 Python scripts information . . . 31

5 Implementation of true polar wander 33
- 5.1 Liouville equation . . . 33
- 5.2 Tidal and load Love numbers . . . 34
- 5.3 Moment of inertia equation . . . 34
- 5.4 Linearized Liouville equation . . . 35
  - 5.4.1 Hydrostatic equilibrium of the rotating Earth . . . 35
  - 5.4.2 True polar wander equations . . . 36

5.5 Implementation in numerical model . . . 38
5.5.1 Model in hydrostatic equilibrium . . . 38
5.5.2 Algorithm for implementing true polar wander . . . 38

6 Code verification tests: results and discussion 45
6.1 Decoupling rotational axis movement from surface load . . . 46
6.1.1 Test 1: change in moment of inertia from forced movement of rotational axis . . . 46
6.1.2 Test 2: change in moment of inertia from surface load . . . 49
6.1.3 Test 3: radial displacements from ICE-3G . . . 52
6.2 Model in hydrostatic equilibrium . . . 55
6.2.1 Test 4: fluid Love number . . . 55
6.2.2 Test 5: change in moment of inertia . . . 58
6.3 True polar wander implementation . . . 60
6.3.1 Test 6: TPW direction and magnitude . . . 60
6.3.2 Test 7: TPW accuracy to moment of inertia around the principal axes . . . 65
6.3.3 Test 8: TPW accuracy to time step size . . . 67
6.3.4 Test 9: simultaneous iteration of the centrifugal and gravitational potential . . . 69

7 Conclusion 73

8 Recommendations 77

Bibliography 79

A Appendix A 83
A.1 Number of time steps until hydrostatic equilibrium . . . 83

B Appendix B 85
B.1 Change in moment of inertia of a point mass . . . 85
B.2 Change in moment of inertia of a distributed mass . . . 86

C Appendix C 89
C.1 Local coordinate systems implementation . . . 89

D Appendix D 91
D.1 TPW sensitivity to mantle viscosity . . . 91

E Appendix E 93
E.1 TPW accuracy to the Earth's rotational rate update . . . 93
E.2 TPW accuracy to maximum spherical harmonic degree . . . 94

List of Figures

1.1 Visual representation of the process of TPW in the body-fixed co-rotating frame viewed in the cross-section of the body, for a body with a dominant relaxation time much longer than its Chandler wobble period. The blue dashed line is the rotational axis, the blue solid line the position of the equatorial bulge, the black dots the original north and south poles, and the red with black encircled dot the mass anomaly. . . . 3

3.1 Schematic overview of the implication of $flag\_lc$ on the direction and the surface used of the centrifugal force for a two-layer Earth model. The red arrows perpendicular to the surface indicate the direction and magnitude of the centrifugal force. The core is indicated in grey. ω indicates the rotation about the rotational axis. . . . 14
3.2 Schematic overview of the instant load on the left and the ramp load on the right for a time step with t_i at the start of the time step and t_{i+1} at the end of the time step. . . . 15
3.3 Partitioning of the core using three perpendicular planes. . . . 16
3.4 Global and local coordinate systems. . . . 17
3.5 Shape of tetrahedral mesh elements and hexahedral mesh elements. . . . 18
3.6 Definition of the time steps $step_i$ from the $Time$ array and the time indices t_i at the end of each time step. . . . 19
3.7 Discrete visualization of a part of the Earth with in grey the area where the mass load is located Ω. Also shown are the area elements $d\Omega$ on a longitude-latitude grid with step sizes $d\theta$ in colatitude and $d\lambda$ in longitude. . . . 21
3.8 Grid of ice heights at specific locations (θ,λ) and corresponding grid cell area. The black dots represent the grid points and the dashed lines represent the boundaries of the grid cells. The arrows indicate to which grid cell the grid point is assigned to. . . . 21
3.9 Zonal (left), sectorial (center) and tesseral (right) surface spherical harmonics. . . . 22
3.10 Timeline of the applied surface load in which the red colored areas represent the total load fields and the white areas under the red curve the load difference fields. . . . 23

4.1 Relation between the Cartesian (x,y,z) and spherical (r,θ,λ) local coordinate systems. . . . 26
4.2 Padding of the π (blue dot) and -π (red dot) longitude at 0° latitude for interpolation of the radial displacements on a 2-D grid representing the spherical Earth. The dots represent the grid points. 27
4.3 Schematic overview of the coupling of the FE model to the Laplace equation. . . . 30

5.1 Exaggerated drawing of the shapes of the spherical non-rotating Earth model and the flattened rotating Earth model in hydrostatic equilibrium. . . . 38
5.2 Schematic overview of the process of true polar wander induced by a surface load and the different reference frames. . . . 39
5.3 The definition of the new rotational axis z' from $(\omega_1,\omega_2,\omega_3)$. . . . 41
5.4 Schematic overview of the coupling of the FE model to the Laplace equation including true polar wander. . . . 43

6.1 Schematic overview of the parts of the code tested in Test 1 on the forced movement of the rotational axis, in which surface loads are not introduced. . . . 46
6.2 Schematic overview of the parts of the code tested in Test 2 on the surface load, in which rotation is not introduced. . . . 46
6.3 Visual representation of the forced axis movement in the x-z plane. z' is the moved rotational axis, Ω the rotational rate, ω_i the rotational vector elements with $i = 1,2,3$ corresponding to the initial x-, y-, and z-axis, respectively, and θ the angle of colatitude over which the rotational axis has moved. . . . 47

6.4 Change in moment of inertia for a two-layer Earth model with the rotational axis drifting from 0° to 45° colatitude in the x-z plane over 5000 years with a constant speed with the analytical solution in blue, and the numerical solutions after 10 iterations with a coarse time array 'Time 1' in green, and with a fine time array 'Time 2' in red. 48
6.5 Change in moment of inertia for a two-layer Earth model with the rotational axis drifting from 0° to 45° colatitude in the x-z plane over 5000 years with a constant speed with the analytical solution in blue, and the numerical solutions per iteration indicated by the other colors with a fine time array 'Time 2'. 49
6.6 Change in moment of inertia for a two-layer Earth model with a constant surface load centered around the south pole with increasing ice thickness towards the pole with the analytical solution in blue, and the numerical solution after 3 iterations for different mesh resolutions of 400 km, 300 km, 200 km, and 150 km. 50
6.7 Change in moment of inertia for a two-layer Earth model with a constant surface load centered around the south pole with increasing ice thickness towards the pole with the analytical solution in blue, and the numerical solutions per iteration indicated by the other colors using a 200 km mesh resolution. 51
6.8 Schematic overview of the parts of the code tested in Test 3 on the radial displacements induced by the ICE-3G ice history. 52
6.9 ICE-3G ice height history at LGM, 18 ka before present (bp), at present day, 0 ka bp, and the difference between LGM and present day. 53
6.10 Test 3 linearly decreasing surface load application over 10 ka. 53
6.11 Surface radial displacements from the numerical method for a mesh resolution of 400 km and after 5 iterations and from the analytical method at 90 ka and 100 ka after hydrostatic equilibrium for which the ICE-3G LGM minus present day load linearly decreases over the last 10 ka. . 54
6.12 Surface radial displacements from the numerical method for a mesh resolution of 400 km and after 5 iterations and from the analytical method at 90 ka and 100 ka after hydrostatic equilibrium for which the ICE-3G LGM minus present-day load linearly decreases over the last 10 ka, at the 77.344°W longitude of largest displacements. 54
6.13 Schematic overview of the parts of the code tested in Test 4 on the model in hydrostatic equilibrium from the fluid Love number. 55
6.14 Schematic overview of the parts of the code tested in Test 4 on the model in hydrostatic equilibrium from the change in moment of inertia. 55
6.15 The fluid Love number of 1.0461 in dashed blue, the degree 2 tidal love number for 0 to 10 ka from the analytical approach in solid blue and from the numerical approach for 12 iterations indicated by the other colors using a 400 km mesh resolution. 56
6.16 Schematic overview of the parts of the code tested in Test 6 to Test 9 on TPW without deformation from the surface load. 60
6.17 TPW direction for a point mass located at 0° longitude and 45° colatitude. The red dot with black encircled is the positive mass anomaly, the red half arc the path the rotational axis will move along when the mass anomaly is located in the x-z plane, at 0° longitude, and z' the new position of the rotational axis. 61
6.18 TPW path for a $2{\cdot}10^{19}$ kg point mass located at 0° longitude and 45° colatitude from the TPW algorithm implementation in the numerical model for 10 iterations and the analytical approach from Hu et al. (2017b) in blue. The dots indicate the data points. The x-axis indicates the time in ka after 10 Ma. The black dots indicate the end of the time steps. 62
6.19 TPW triggered by the ICE-3G LGM minus present day ice history over 5 ka for 10 iterations for the four-layer Earth model. Black dots indicate the end of time steps. The pole position reaches the top left of the plot at 5 ka after hydrostatic equilibrium. 64
6.20 TPW triggered by ICE-3G over a period extending from the onset of glaciation, the origin of the plot, through 8 glacial cycli. The pole position reaches the top left portion of the plot at LGM, and the solid dot at present day. (Mitrovica et al., 2001) 64
6.21 TPW triggered by a $2{\cdot}10^{19}$ kg point mass at 0° longitude and 45° colatitude over 5 ka for 5 iterations for the four test cases. 66
6.22 The unit vector elements of the x-axis in the initial local frame for each time step and for 5 iterations for test 7-1. 67

6.23 The unit vector elements of the x-axis in the initial local frame for each time step and for 5 iterations for test 7-3. 67
6.24 Visualization of TPW triggered by point mass for different time step sizes. 68
6.25 TPW triggered by a $2{\cdot}10^{19}$ kg point mass at 0° longitude and 45° colatitude over 5 ka after 5 iterations for 0.25 ka time steps, 0.5 ka time steps, and 1.0 ka time steps. 68
6.26 TPW triggered by a $2{\cdot}10^{19}$ kg point mass at 0° longitude and 45° colatitude over 5 ka after 12 iterations for the reference test and the 6 tests in which the iterations do not occur for all time steps simultaneously for the centrifugal and perturbed gravitational potential. 70
6.27 TPW triggered by a $2{\cdot}10^{19}$ kg point mass at 0° longitude and 45° colatitude over 5 ka after 12 iterations for the analytical approach from Hu et al. (2017b), and Test 9-6 and the reference test in which the iterations do and do not occur for all time steps simultaneously, respectively, for the centrifugal potential and the perturbed gravitational potential. 71

B.1 Schematic overview of the parts of the code tested in Test B.1 and B.2 on the surface load to the change in moment of inertia from the load $\Delta\mathbf{I}_L$, for a point mass and distributed mass respectively. 85

C.1 Schematic overview of the parts of the code tested in Test C.1 on the implementation of the local coordinate systems for each time step to which the centrifugal potential is applied. 89
C.2 Change in moment of inertia for a two-layer Earth model with the rotation axis drifting from 0° to 45° colatitude in the x-z plane over 5000 years with a constant speed with the analytical solution in blue, and the numerical solutions after 10 iterations using the original local coordinate system implementation in green, and the 'new' local coordinate system implementation in red. 90

D.1 TPW triggered by a $2{\cdot}10^{19}$ kg point mass at 0° longitude and 45° colatitude over 15 ka after 5 iteration for mantle viscosities of 1e20 Pa s, 1e21 Pa s, and 1e22 Pa s. 91

E.1 TPW triggered by a $2{\cdot}10^{19}$ kg point mass at 0° longitude and 45° colatitude over 5 ka for 5 iterations for a constant Ω and updated Ω for the centrifugal potential definition. 93
E.2 The spatial signal of a $2{\cdot}10^{19}$ kg point mass at 0° longitude and 45° colatitude on a 1° grid converted to spherical harmonic coefficients and back to the spatial domain using a maximum degree of 45, 90, and 180. 94
E.3 TPW triggered by a $2{\cdot}10^{19}$ kg point mass at 0° longitude and 45° colatitude over 5 ka for 5 iterations for a maximum spherical harmonic degree of 45 (crosses) and 180 (dots) for the surface mass density in the perturbed gravitational potential definition. 95

List of Tables

6.1 Two-layer Earth model properties (Hu et al., 2017a). 47
6.2 Four-layer Earth model properties (Mitrovica et al., 2001). 52
6.3 Degree 2 tidal Love number at 200 Ma for all iterations for the two-layer Earth model and its percentage compared to the analytical fluid Love number of 1.0461. 56
6.4 Degree 2 tidal Love number for all time steps for iteration 12 for the two-layer Earth model and its percentage compared to the analytical fluid Love number of 1.0461. 57
6.5 Degree 2 tidal Love number at 200 Ma for all iterations for the four-layer Earth model and its percentage compared to the analytical fluid Love number of 0.96737. 57
6.6 Degree 2 tidal Love number for all time steps for iteration 12 for the four-layer Earth model and its percentage compared to the analytical fluid Love number of 0.96737. 58
6.7 Change in moment of inertia after 12 iterations after 10 Ma when the two-layer Earth model is in equilibrium and compared to the analytical solution. 58
6.8 Change in moment of inertia after 12 iterations at 10 Ma when the two-layer Earth model is in equilibrium for a mesh resolution of 400 km and 300 km and compared to the analytical solution. 59
6.9 Change in moment of inertia after 5 iterations at 1 year after hydrostatic equilibrium, at 10 Ma, for the two-layer Earth model for a mesh resolution of 500 km. 64

A.1 Change in moment of inertia at 10 Ma for a simulation using multiple time steps (MS) and for a simulation using one time step (OS) for the two-layer Earth model for a 400 km mesh resolution after 12 iterations. 83

B.1 Change in moment of inertia of the input surface load for a point mass of $2{\cdot}10^{19}$ at 45° colatitude in the x-z plane, from the analytical approach and from the grid approach of the code. 86
B.2 Change in moment of inertia of the input surface load for a distributed mass being the ICE-3G ice history (LGM-present day), from the analytical approach (Milne and Mitrovica, 1998) and from the grid approach of the code. 87

1 Introduction

Mass redistribution on the Earth's surface and inside the Earth causes the Earth's gravity field to change. Many mass transport processes occur close to the Earth's surface, the most significant ones being: oceanic and atmospheric tides, oceanic and atmospheric mass redistribution related to meteorological processes, hydrological variations in watersheds and basins, and melting of glaciers and ice sheets with Greenland and Antarctica being the largest contributors, consequently causing global sea level rise. With the GRACE satellite mission, operational between 2002 and 2017, and the recently launched GRACE Follow-On mission, monthly mass changes are monitored. These data however also include the Earth's deformation due to glacial isostatic adjustment (GIA), which is a response to changes in ice mass distribution over a period from the late Pleistocene up to present. The mass change signal needs to be corrected for GIA-induced mass changes for the present-day mass changes to be revealed, which are of importance for climate change related studies on for example ice mass losses and sea level rise.

The $C_{2,1}$ and $C_{2,-1}$ spherical harmonic coefficients of the mass change signal are affected by true polar wander (TPW), the secular drift of the position of the Earth's rotational axis with respect to the Earth's surface. Until 2004 the secular drift of the pole was directed along the ~70°W meridian over the last century. Recent observations of TPW show that from 2005 onward the TPW changed into the direction of Greenland (Chen et al., 2013) and that the speed has increased, which may imply the acceleration of ice melt in Greenland in recent years. However, the effect of GIA on polar wander is still poorly understood. TPW occurs due to environmental processes such as cryospheric, hydrologic, and oceanic mass exchanges and geophysical processes such as GIA, mantle convection, and seismic events, which are processes on a wide range of time scales. The focus of this research is on GIA-induced TPW to improve GIA models, but since GIA is not the only contributor to TPW, it does not fully have to explain the observed TPW.

The rotational state of the Earth and its interior are closely related. Analytical methods exist to model TPW for Earth models consisting of homogeneous layers. However, the Earth is not homogeneous but heterogeneous, and this may have a significant effect on the prediction of GIA-induced TPW. Heterogeneities in mantle viscosity can be taken into account by numerical modeling. Section 1.1 describes the deformation behavior of the Earth. The process of true polar wander and how it is affected by the Earth's interior is discussed in Section 1.2. The need for a numerical model to predict polar wander is discussed in Section 1.3. This leads to the research objective and the research questions which are presented in Section 1.4. Mathematical expressions will not be covered in this chapter yet, but will be introduced in the coming chapters.

1.1. Deformation behavior of the Earth

The Earth's rotational behavior is complex due to the body's deformable nature. The Earth is viscoelastic: it acts elastic on short time scales and viscous as well as elastic over long time scales, and thus its short-term and long-term rotational behavior differ from one another. In order to model the response of the Earth due to loading one needs a rheological model, which is a mathematical relation between stress and strain. The choice of rheological model depends on the available knowledge of the rheological behavior of the medium, the quality of the geophysical data which the model needs to match, and the mathematical difficulty of the model (Sabadini et al., 2016).

The linear Maxwell model is the simplest model which can describe short term elastic behavior and long term viscoelastic behavior for the Earth (Maxwell, 1867). The historic Earth reorientation does not call for a more realistic rheology model than the Maxwell model for the study of the response of Earth to glaciation (Hu, 2018). The observed TPW speed is $\sim 1^\circ$ Myr^{-1} (Dickmann, 1977), which is a slow process. The TPW speed and the long wavelength phenomenon of GIA allow for the use of a linear model. The Maxwell model (Maxwell, 1867) is chosen as the fundamental rheological model which describes the viscoelastic response of the Earth to glaciation. The Maxwell rheology can be represented by a spring, which is purely elastic, and a damper, which is purely viscous, connected in series. The total deformation of a viscoelastic material is the sum of the elastic and the viscous component:

1. When a constant strain is applied to the material, the damper ensures that the stress decays with time to zero.
2. When a constant stress is applied to the material, the spring will instantaneously deform whereas the damper will deform with a constant rate, thus linearly with time. When the stress is then removed, the spring springs back instantaneously whilst the damper does not recover at all.

A homogeneous one-layer Earth model can be represented by a single spring-damper system. However, a more realistic Earth model consists of multiple layers; the Earth is then represented by a stratified sphere with homogeneous layers. Each of these layers has its own physical properties such as density, rigidity, and viscosity, and can be represented by a spring-damper system. The material viscosity affects the damper and the material rigidity affects the spring. The relaxation time of the material is dependent on the rigidity and viscosity. The entire model will then be a series connection of the individual spring-damper systems per layer. The deformation of the model is dependent on the physical properties per layer. For a homogeneous single layer or stratified Earth this deformation can be determined analytically. When heterogeneity is taken into account, i.e. when physical properties are allowed to vary laterally, the deformation cannot be solved analytically. An analytical method based on the normal mode method does exist for heterogeneous models under the assumption that the relative perturbation in viscosity is small (Tromp and Mitrovica, 2000). However, for large relative perturbations in viscosity numerical methods, such as the finite element method (FEM), are required to solve for the Earth's response to loading.

1.2. Rotational behavior of the Earth

For a viscoelastic body the material can fully relax. The balance of the centrifugal force and self-gravitational force determines the equilibrium shape, or hydrostatic shape, of the rotating body, neglecting the effect of third bodies and compressibility of the body. Wu and Peltier (1984) provide the rotational theory based on Gold (1955) and Munk and MacDonald (1960). The two governing equations are:

1. The linearized Liouville equation for small angle TPW, describing the change in rotational state needed to conserve angular momentum for a change in moment of inertia.
2. The moment of inertia equation, describing the change in moment of inertia for a change in rotational state. The moment of inertia changes due to the direct effect of a mass anomaly, the indirect effect of the mass anomaly causing the body to deform, and the equatorial bulge readjustment perpendicular to the new position of the rotational axis caused by the mass anomaly.

Conservation of angular momentum keeps the rotational axis fixed in an inertial frame, assuming that no external torque is exerted on the body. The moment of inertia of the body can be altered by geophysical processes, such as GIA, which perturb the body due to a redistribution of mass. As a consequence of the change in moment of inertia the body has to reorient to conserve angular momentum. The rotational velocity may also change to keep the angular momentum constant. For an observer on Earth the reorientation of the body appears as if the rotational axis is moving with respect to the surface. This phenomenon is called polar motion and is characterized by a short-term periodic signal and a long-term secular drift. The short-term periodic signal contains an annual wobble, excited by natural phenomena with a period of one year, and the Chandler wobble with a period of 14 months. The Chandler wobble is an eigenmotion of the body and is induced by the deformable nature of the body and ocean and atmosphere. The averaged long-term secular drift is called true polar wander (TPW), and is also a consequence of the deformation of the rotating body (Munk and MacDonald, 1960).

Rotational stability of planetary bodies was first described by Gold (1955), who stated that the rotational axis is inherently unstable because the equatorial bulge will reorient to the new position of the rotational axis, which tries to align with the axis of maximum moment of inertia, and thereby the system will lose all memory of any preexisting rotational state. A positive mass anomaly will eventually be relocated to the equator, and a negative mass anomaly to the poles. A stepwise overview of this rotational behavior is described here from the body-fixed co-rotating frame, for the condition that the dominant relaxation time of the body is much longer than its Chandler wobble period (Hu, 2018). The process is visually presented in Figure 1.1 (a-d).

1. (a) The rotating viscoelastic body in hydrostatic equilibrium has a bulge that is centered at the equator. Therefore this bulge is referred to as the equatorial bulge.
2. (b) A positive mass anomaly within or on the rotating body breaks the rotational stability and causes the centrifugal force to change.
3. (b) To conserve angular momentum the rotational axis moves in the direction of the axis of maximum moment of inertia. The body thus reorients until a new equilibrium position is reached.
4. (c) After the reorientation, the centrifugal force is applied to the body at its new position, causing the equatorial bulge to readjust to the position perpendicular to the rotational axis again. This process is known as equatorial bulge readjustment.
5. (d) With the equatorial bulge readjusted the balance between the centrifugal force and self-gravitational force is broken again, and a new unbalanced force is exerted on the body.

In reality the reorientation of the body and the readjustment of the equatorial bulge occur at the same time, and not as an iterative process as described above. Both processes keep going until the centrifugal force and the self-gravitational force on the body are balanced again, leading to the positive mass anomaly eventually reaching the equator.

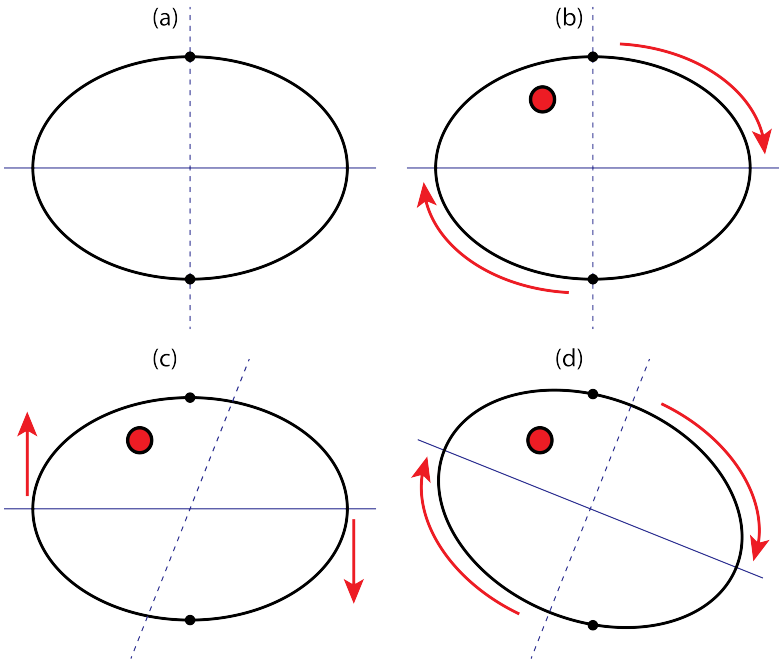

Figure 1.1: Visual representation of the process of TPW in the body-fixed co-rotating frame viewed in the cross-section of the body, for a body with a dominant relaxation time much longer than its Chandler wobble period. The blue dashed line is the rotational axis, the blue solid line the position of the equatorial bulge, the black dots the original north and south poles, and the red with black encircled dot the mass anomaly.

The above process of TPW does not take into account the effect of an elastic lithosphere. A body with an elastic lithosphere is not able to fully relax, as is the case for a body without an elastic lithosphere. During the process of TPW stress will accumulate in the elastic, thus very high viscosity, lithosphere. The accumulation of stress in the lithosphere prevents the equatorial bulge to fully readjust (Hu, 2018; Willemann, 1984). A stepwise overview of this rotational behavior is described here:

1. The rotating viscoelastic body with an elastic lithosphere in hydrostatic equilibrium has a bulge that is centered at the equator. Therefore this bulge is referred to as the equatorial bulge.
2. A positive mass anomaly within or on the rotating body breaks the rotational stability and causes the centrifugal force to change.
3. To conserve angular momentum the rotational axis moves in the direction of the axis of maximum moment of inertia. The body thus reorients. Simultaneously, stress accumulates in the lithosphere due to the deformation, causing a restoring force which counteracts TPW. In other words, the rotational axis keeps moving away from the mass anomaly which is not compensated. At the same time the equatorial bulge cannot fully relax, causing a remnant bulge and thus resistance to TPW.
4. The restoring force from the stress in the lithosphere will eventually become large enough to cancel the change in centrifugal force and the process of TPW stops. As a result, the mass anomaly cannot reach the equator because the lithosphere prevents the body from fully relaxing.
5. The final position of the rotational axis is governed by a balance between the stabilization of the remnant rotational bulge and the TPW induced by the mass anomaly.

When comparing the cases for the body without and with an elastic lithosphere, their rotational behavior also differ from one another when the mass anomaly is removed from the body. For the body without an elastic lithosphere the mass anomaly is fully compensated and the equatorial bulge is fully readjusted. A new equilibrium position is reached and therefore all memory of prior states of the rotational axis are lost. Thus, when removing the mass anomaly the rotational axis will not move. However, for the body with an elastic lithosphere the remaining stress in the lithosphere will force the body to reorient back to the original rotational axis position until the lithosphere is fully relaxed again, as before the mass anomaly was applied. When the lithosphere is somewhat able to relax during the TPW process, the forcing from the stress in the lithosphere reduces and the final position of the rotational axis will not be at its original position, but somewhere in between its original position and the position at when the mass anomaly was removed.

The hydrostatic equilibrium of the rotating body needs to be considered as well. A viscoelastic body is in hydrostatic equilibrium when the centrifugal force and self-gravitational force are in balance, when no external torques are present. This results in a flattened body in hydrostatic equilibrium; the Earth's equatorial radius is larger than its polar radius. Mitrovica et al. (2005) argues that the flattening of the Earth is not only a function of the hydrostatic equilibrium but also of non-hydrostatic signals coming from long-term geophysical processes such as mantle convection and fossil rotational effects from the cooling and forming of the lithosphere. An excess ellipticity needs to be introduced for a better treatment of the background equilibrium form.

Wu and Peltier (1984) provides the rotational theory for small angle polar wander for lateral homogeneous models based on the Maxwell rheology and Mitrovica et al. (2005) introduces a different treatment of the background oblateness of the Earth. Hu et al. (2017a,b) presents an analytical method for large angle TPW also using the linearized Liouville equation for lateral homogeneous models. The large angle polar wander is based on the assumption that during the process of polar wander the equatorial bulge readjustment is fast enough, or the polar wander slow enough, such that the equatorial bulge is always nearly perpendicular to the rotational axis. This method is benchmarked with the method from Wu and Peltier (1984) and is able to include non-stationary surface loads with respect to the rotational axis. The recently proposed approach of Hu et al. (2017a,b) allows for larger flexibility due to that TPW is not limited to small angles and with the option to include non-stationary loads.

1.3. Need for numerical modeling

The deformation of the Earth model under loading is dependent on the physical properties per layer. For a homogeneous single layer or stratified Earth this deformation can be determined analytically. However, the Earth is not laterally homogeneous but heterogeneous. An analytical method based on the normal mode method does exist for heterogeneous models under the assumption that the relative perturbation in viscosity is small (Tromp and Mitrovica, 2000). However, for large relative perturbations in viscosity numerical methods are required to solve for the Earth's response to loading.

Heterogeneities may have a significant effect on the prediction of GIA-induced TPW as explained here, and visualized in Figure 1.1. The relation between the size of the mass anomaly and the magnitude of the change in centrifugal force exerted on the body is dependent on the local viscosity. When at the location of the mass anomaly there is a local low viscosity, the mass anomaly will soon blend in with the body, causing the extra force to diminish. On the other hand, the equatorial bulge readjustment is dependent on the average global viscosity. These viscosity variations may affect polar motion and thus TPW. This leads to the question whether lateral viscosity variations have a significant effect on the rotational behavior of Earth due to mass redistribution from glacial isostatic adjustment. When heterogeneity is taken into account, i.e. when physical properties are allowed to vary laterally, the resulting deformation cannot be solved analytically. Numerical methods such as the finite element method (FEM) are required to solve for the Earth's response to loading.

The accurate prediction of glaciation-induced TPW is of importance for GIA models. GIA models are required in order to correct satellite gravimetry observations for the ongoing solid Earth deformation from GIA, such that these mass changes are not taken into account when determining present-day surface mass changes. Polar wander heavily dominates the $C_{2,1}$ and $C_{2,-1}$ spherical harmonic coefficients from satellite gravimetry observations. It is expected that lateral viscosity variations near North America have a larger effect on GIA-induced TPW than lateral viscosity variations near Antarctica for two reasons. The Laurentian ice sheet over northern North America lost more ice mass from the last glacial maximum (LGM) up to present and the Laurentian ice sheet was located close to the maximum of the $C_{2,1}/C_{2,-1}$ signal. Antarctica is centered around the pole and thus Antarctica is only marginally able to excite polar motion. Another reason to study the effect of heterogeneous viscosities is that plate boundaries reduce the effective lithospheric thickness and thus reduce the effect of the lithosphere on TPW. A broken high viscosity lithosphere may have a significant effect on long-term TPW.

Current GIA models give a wide range in values for the $C_{2,1}$ and $C_{2,-1}$ spherical harmonic coefficients. There is no agreement on the values for the $C_{2,1}$ and $C_{2,-1}$ coefficients due to GIA. There are GIA models based on lateral homogeneous Earth models that do not include the effect of TPW (Ivins and James, 2005) and do include the effect of TPW (Peltier, 2004; Peltier et al., 2015; Purcell et al., 2016). There are also GIA models based on lateral heterogeneous Earth models that do not include the effect of TPW (Latychev et al., 2005) and do include the effect of TPW (A et al., 2013; Paulson, 2006; Paulson et al., 2007; Whitehouse et al., 2012). However, the model of Whitehouse et al. (2012) is only applicable to Antarctica and it is not clear how polar wander is included in the model as it is only stated that the GIA model accounts for rotational feedback. The model of Paulson (2006); Paulson et al. (2007), and of A et al. (2013) which is based on Paulson (2006); Paulson et al. (2007), do include TPW. The numerical model has been benchmarked with an analytical spectral method for the resulting topographic and geoid heights and rates, and they differ by 1% to 4% for different cases. However, the polar wander itself is not quantified and verified and neither is the effect of lateral viscosity variations on GIA-induced TPW researched.

Furthermore, the numerical analysis is based on a finite element code which is derived from a code developed for viscous mantle convection (Zhong et al., 2000, 2003). Within the research group at TU Delft a numerical model exists based on finite element (FE) software for engineering purposes. Adjustments had to be made to make the software suitable for geophysical applications which involve long wavelength deformations and viscoelasticity based on Wu (2004), and the centrifugal force included according to Wu and Wang (2006). It would be valuable to include TPW, the coupling between surface loads and the rotational behavior of the body, in the existing numerical model. By incorporating the TPW approach described by Hu et al. (2017a,b) in the numerical model, research can be performed on the lateral viscosity variations on glaciation-induced TPW. Accurate GIA-induced TPW predictions can be made by using this large angle approach which allows for non-stationary surface loads, in conjunction with the FE model.

The aim is to provide a realistic range for the $C_{2,1}$ and $C_{2,-1}$ coefficients for GIA models, based on realistic Earth viscosity profiles, lithospheric characteristics, and ice loading histories. Even though the effect of lateral viscosity variations on GIA-induced TPW may turn out to be small, it is still useful to provide a realistic range for these coefficients. This would lead to more consistent GIA models, and thus to more consistent determination of present-day mass change signals which are used for climate change studies.

1.4. Research objective and research questions

In order to investigate the effect of lateral viscosity variations on GIA-induced TPW, TPW needs to be implemented in a numerical model. A numerical model based on finite element (FE) analysis exists within the research group which can provide displacements in the model and on its surface excited by a surface load. The numerical model is based on (Wu, 2004) and (Wu and Wang, 2006). However, the Earth's rotational behavior as response to surface loading, based on (Wu and Peltier, 1984) and (Hu et al., 2017a), is not included in this model yet. This research focuses on the implementation of true polar wander in a numerical model, which leads to the following research objective:

To implement true polar wander in a numerical model based on the finite element method by using state-of-the-art rotational theory.

The research question follows directly from the research objective:

How to implement true polar wander in a numerical model based on the finite element method?

Subquestions are formulated which help to answer the research question. It is not known how the accuracy of the numerical model compared to analytical methods affects TPW predictions. Lateral homogeneous Earth models have to be used in the numerical analysis to be able to determine the accuracy. Before TPW can be implemented, before the coupling between surface loads and the rotational behavior of the body, the accuracy of the existing numerical model needs to determined for these two decoupled elements. The accuracy of the numerical model compared to analytical methods has to be determined for a rotating Earth with a forced movement of the rotational axis, and for a non-rotating Earth with surface loads. Furthermore, it is not known how accurately the numerical model can approach the hydrostatic equilibrium of the body. Only then the accuracy of the model for true polar wander can be determined. Potential discrepancies in equilibrium shape between the numerical and analytical solution can have an effect on TPW. Other influencing factors on the accuracy of the numerical model for true polar wander are for example how accurately the surface load can be represented in terms of moment of inertia, the time step size used in the simulation, and the maximum spherical harmonic degree used for the decomposition of the surface load and radial displacements into their coefficients. These accuracy considerations for the numerical model result in the following subquestions:

1. What is the accuracy of the numerical model for the response to a forced movement of the rotational axis?
2. What is the accuracy of the numerical model for the response to surface loading?
3. What is the accuracy of the numerical model for the Earth in hydrostatic equilibrium?
4. What is the accuracy of the numerical model for true polar wander?

The research question and its subquestions are addressed in this research. Here an overview is given of the structure of the report. Chapters 2, 3, and 4 describe in detail the existing numerical model within the research group, thus without TPW. No documentation exists yet on the numerical model. The model is in detail explained such that future MSc students or PhD candidates who will work with or expand the model can rely on this documentation instead of having to reinvent the wheel, and hopefully also add on to it. Chapter 5 discusses the existing TPW theory and the implementation of true polar wander in the numerical model, followed by the results in Chapter 6, the conclusion in Chapter 7, and the recommendations in Chapter 8.

- Chapter 2 describes the finite element method and the application suite `Abaqus` used to determine displacements in the Earth model under surface loading from stresses in the Earth model. The existing numerical model which is extended in this research is based on this method. Commercially available FEM application suites such as `Abaqus` solve for the stiffness equation. For geophysical applications which involve long wavelength deformations and viscoelasticity the stiffness equation needs to be modified to take into account the restoring force of isostasy and self-gravitation. For a self-gravitating incompressible spherical Earth model the boundary conditions, which couple stress and displacements in the Earth model, at each of the model layer surfaces are derived from this modified stiffness equation and Laplace's equation.

- Chapter 3 describes the definition and the generation of the Earth model and the initial forces, from the Earth's rotation and surface loading, acting on the model in `Abaqus`. This is done using two `Python` scripts. The `Model_data.py` script includes parameters that the user can vary, such as the input surface load and the mesh resolution. Subsequently, the `Model_gen.py` script generates the model based on the parameters defined in `Model_data.py`.
- Chapter 4 describes how the radial displacements, determined by the FE analysis, and the perturbed gravitational potential, as solution to Laplace's equation, are implemented in the numerical model in the `Iter.py` and `sph_tools_TPW.py` scripts. To have a complete set of boundary conditions the perturbed gravitational potential at the model layer surfaces needs to be known. Thus, an iterative process is required for the determination of the radial displacements of the body and the perturbed gravitational potential as they are a function of one another. It is described how a converged solution is obtained through iteration for all time steps simultaneously.
- Chapter 5 argues how the linearized Liouville equation together with the moment of inertia equation can be used for large angle polar wander. Coordinate transformations of the changes in moment of inertia, from the model deformations and the surface load, are performed to the local frame which z-axis coincides with the rotational axis. A stepwise overview and a schematic overview of the implementation of TPW in the numerical model are also presented.
- Chapter 6 describes the code verification tests performed using homogeneous Earth models such that the solution can be compared to analytical solutions to determine the accuracy of the numerical model. Tests are performed on:
  - The change in moment of inertia from a forced movement of the rotational axis.
  - The radial displacements and change in moment of inertia from surface loading using distributed loads.
  - The degree 2 tidal Love number and the change in moment of inertia from a spherical non-rotating model to a flattened rotating model in hydrostatic equilibrium.
  - The number of time steps required before hydrostatic equilibrium is reached.
  - The moment of inertia of the surface load itself from a point mass and a distributed surface load.
  - The TPW feeding back into the numerical model through the definition of the local coordinate system for each time step based on the position of the rotational axis.
  - The TPW magnitude and direction from a point mass and a distributed surface load.
  - The TPW magnitude and direction from a point mass for:
    - varying mantle viscosities.
    - varying moments of inertias around the principal axes from the hydrostatic equilibrium.
    - the Earth's rotational rate update in the definition of the centrifugal potential.
    - varying time step sizes in the simulation.
    - varying maximum spherical harmonic degrees for the decomposition of the surface load and radial displacements into their coefficients.
  - The iteration of the centrifugal potential and perturbed gravitational potential per time step instead of over all time steps simultaneously.
- Chapter 7 provides the answers on the research question and its subquestions based on the code verification tests performed in Chapter 6.
- Chapter 8 presents recommendations ranked on priority based on the research done so far on the implementation of TPW in the numerical model and the potential applications of the model.

2

Finite element method and model

This chapter describes the finite element method and model. The finite element method (FEM) is the numerical method used in this research to determine displacements in the Earth model under centrifugal forcing and surface loading, from stresses in the Earth model. The finite element method is discussed in Section 2.1, along with the used application suite `Abaqus` for the numerical analysis. Commercially available FEM application suites solve for the stiffness equation. For geophysical applications which involve long wavelength deformations and viscoelasticity the stiffness equation needs to be modified to take into account the restoring force of isostasy and self-gravitation. The modified stiffness equation is presented in Section 2.2. For a self-gravitating incompressible spherical Earth model boundary conditions at each of the model layer surfaces are derived from the modified stiffness equation and Laplace's equation. The boundary conditions couple stress and displacements in the Earth model and are presented in Section 2.3. A complete set of boundary conditions for the FE method is obtained when the perturbed gravitational potential is known at all model layer surfaces.

2.1. Finite element method

The formulations of the laws of physics for space-dependent and time-dependent problems are expressed in terms of partial differential equations (PDEs). PDEs can generally not be solved with analytical methods. Therefore, approximations to the PDEs have to be created based on discretization. An approximation to the real solution of the PDE can be found by approximating the PDE with numerical model equations, which are solved using numerical methods. The finite element method (FEM) is a numerical method which discretizes the continuous model with finite elements, resulting in a mesh with nodes. The numerical model equations approximating the solution to the PDEs are computed for mesh elements. FEM allows for the modeling of deformation and stresses in the Earth, and is especially useful when variations of material properties in arbitrary directions are present in the Earth model (Gasperini and Sabadini, 1990; Kaufmann et al., 1997, 2000).

`Abaqus 6.14` is the application suite for the finite element (FE) analysis used in this research. Building models and performing tasks in `Abaqus` using only the graphical user interface (GUI) can be very time consuming. Therefore, `Abaqus` makes use of the `Python` programming language, such that for example repetitive tasks can be automated, parameters can be varied within optimization problems, and information can be efficiently extracted. `Abaqus` has its own `Python` library which is extensively used. The `Python` commands can be found in the scripting reference guide (Abaqus, 2014).

2.2. Modified stiffness equation

Commercially available FEM application suites solve for the stiffness equation since these application suites are designed for engineering purposes. The stiffness equation, which only describes the divergence of stress, is too simplistic for geophysical applications which involve long wavelength deformations and viscoelasticity (Wu, 2004). The stiffness equation solved for in commercially available FEM application suites is as follows (Wu, 2004):

$$\vec{\nabla} \cdot \boldsymbol{\tau} = 0 \tag{2.1}$$

in which $\vec{\nabla}$ is the nabla operator and $\boldsymbol{\tau}$ the stress tensor. For geophysical applications the stiffness equation would only be realistic for elastic deformations with very short wavelengths. For long wavelength deformations and viscoelasticity the stiffness equation needs to be modified to take into account the restoring force of isostasy and self-gravitation from the solid Earth and oceans. The linearized elastic equation of motion is then as follows (Wu, 2004; Wu and Peltier, 1982):

$$\vec{\nabla} \cdot \boldsymbol{\tau} - \vec{\nabla} \left(\vec{u} \cdot \rho_0 g_0 \hat{r} \right) - \rho_1 g_0 \hat{r} - \rho_0 \vec{\nabla} \phi_1 = 0 \tag{2.2}$$

in which $\vec{u}$ is the displacement vector, ρ the density, g the gravitational acceleration, $\hat{r}$ the unit vector in radial direction, and ϕ the gravitational potential, with subscript 0 referring to the hydrostatic state and subscript 1 to the perturbed state. The first term is the divergence of stress (Wu, 1992). The second term is the advection of pre-stress or the restoring force from isostasy, and this term is included to ensure viscoelastic gravitational relaxation (Wu, 1992, 2004; Wu and Peltier, 1982). The third term represents internal buoyancy, in which the perturbed density is given by (Wu, 2004):

$$\rho_1 = -\rho_0 \vec{\nabla} \cdot \vec{u} - \vec{u} \cdot \left(\partial_r \rho_0 \right) \hat{r} \tag{2.3}$$

When there is no large negative ambient pressure gradient, $-\vec{u} \cdot \left(\partial_r \rho_0 \right) \hat{r}$ in Equation 2.3, the internal buoyancy, third term in Equation 2.2, will counteract the restoring force of isostasy, second term in Equation 2.2, since they have opposite signs and a comparable magnitude (Wu, 2004). This counteracting effect between internal buoyancy and the restoring force of isostasy causes instability (Vermeersen and Mitrovica, 2000). When assuming incompressibility, $\rho_1 = 0$, this instability cannot arise, since the third term in Equation 2.2 representing internal buoyancy then becomes zero. When assuming compressibility the internal buoyancy should be zero to ensure stability. However, the separation of compressibility and internal buoyancy for materials is physically impossible (Klemann et al., 2003; Wu, 2004). Therefore, incompressibility has to be assumed for the use of commercial FEM application suites for geophysical problems.

The fourth term in Equation 2.2 represents self-gravitation. Mass redistribution causes changes to the gravitational potential as described by Poisson's equation:

$$\nabla^2 \phi_1 = 4\pi G \rho_1 \tag{2.4}$$

in which G is the gravitational constant. For a self-gravitating incompressible spherical Earth model the modified stiffness equation and Poisson's equation reduce to (Wu, 2004):

$$\vec{\nabla} \cdot \boldsymbol{t} = \vec{\nabla} \cdot \boldsymbol{\tau} - \vec{\nabla} \left(\vec{u} \cdot \rho_0 g_0 \hat{r} \right) - \rho_0 \vec{\nabla} \phi_1 = 0 \tag{2.5a}$$

$$\nabla^2 \phi_1 = 0 \tag{2.5b}$$

in which $\boldsymbol{t}$ is the new stress tensor. For incompressibility Poisson's equation thus reduces to Laplace's equation. From the modified stiffness equation and Laplace's equation for a self-gravitating incompressible spherical Earth model boundary conditions can be derived at each of the model layer surfaces. The boundary conditions couple stress and displacements in the Earth model.

2.3. Boundary conditions

Wu (2004) provides how the modified stiffness equation and Laplace's equation for a self-gravitating incompressible spherical Earth model are transformed to boundary conditions at the Earth's surface, at internal solid-solid boundaries, and at the core-mantle boundary (CMB). Next to the boundary conditions from the modified stiffness equation and Laplace's equation, there is a set of boundary conditions for an elastic Earth. For all layer surfaces the continuity of potential, $\left[\phi_1 \right]_-^+ = 0$, is a boundary condition for an elastic Earth (Cathles, 1975). All boundary conditions at the Earth's surface, at internal solid-solid boundaries, and at the CMB are presented in Subsections 2.3.1, 2.3.2, and 2.3.3, respectively. To conclude, Subsection 2.3.4 explains that one needs to solve for Laplace's equation to obtain a complete set of boundary conditions for the FE method.

2.3.1. Earth's surface

For the Earth's surface the boundary condition derived from the modified stiffness equation and Laplace's equation is as follows (Wu, 2004):

$$t_{rr} + \rho_0 g_0 u_r = -\sigma g_0 - \rho_0 \phi_1 \tag{2.6}$$

in which t_{rr} is the new stress tensor component in radial direction, and σ the surface mass density of the applied surface load. $-\sigma g_0$ is the surface load and $-\rho_0\phi_1$ the potential load both applied to the surface. The term $\rho_0 g_0 u_r$ can be simulated by the Winkler foundation, with a foundation stiffness per area of $\rho_0 g_0$ (Wu, 2004), in which ρ_0 is the density of the model at the surface and g_0 the gravitational acceleration at the surface. Under forcing the model experiences elastic deformation. The Winkler model assumes a continuous elastic foundation such that reaction forces of the elastic foundation are linearly proportional to the displacement at any point.

For the surface of the Earth $[\boldsymbol{\tau} \cdot \hat{r}]^+_- = 0$ leading to (Cathles, 1975; Wu and Peltier, 1982):

$$\tau_{rr}|_{z=0} = -\sigma g_0 \tag{2.7a}$$

$$\tau_{r\theta}|_{z=0} = 0 \tag{2.7b}$$

in which τ_{rr} is normal stress, $\tau_{r\theta}$ shear stress, and z the depth. Additionally, the gradient of potential satisfies (Cathles, 1975; Wu and Peltier, 1982):

$$[\nabla\phi_1 \cdot \hat{r}] + 4\pi G\rho_0 u_r = 4\pi G\sigma \tag{2.7c}$$

in which $\nabla\phi_1$ is the gradient of potential, and $u_r = \overrightarrow{u} \cdot \hat{r}$.

2.3.2. Solid-solid internal boundaries

For the solid-solid internal boundaries, with no internal mass loads, the boundary condition derived from the modified stiffness equation and Laplace's equation is as follows (Wu, 2004):

$$[t_{rr}]^+_- = \Delta\rho \left(g_0 u_r + \phi_1\right) \tag{2.8}$$

in which $\Delta\rho = \left(\rho_- - \rho_+\right)$ is the density jump at the interface, between the lower layer (-) and upper layer (+). The Winkler foundation is applied with a foundation stiffness per area of $\left(\rho_- - \rho_+\right) g_0$, in which g_0 is the gravitational acceleration at the interface. Next to the Winkler foundation, the potential load $\Delta\rho\phi_1$ needs to be applied at the layer interface.

For the solid-solid internal boundaries $[\boldsymbol{\tau} \cdot \hat{r}]^+_- = 0$ leading to (Cathles, 1975; Wu and Peltier, 1982):

$$\tau_{rr}|_{z=0} = 0 \tag{2.9a}$$

$$\tau_{r\theta}|_{z=0} = 0 \tag{2.9b}$$

Furthermore, there is continuity of displacements and there are no internal mass loads, leading to (Cathles, 1975; Wu and Peltier, 1982):

$$[\overrightarrow{u}]^+_- = 0 \tag{2.9c}$$

$$[\nabla\phi_1 \cdot \hat{r} + 4\pi G\rho_0 u_r]^+_- = 0 \tag{2.9d}$$

2.3.3. Core-mantle boundary

For the solid-fluid internal boundary, or the core-mantle boundary (CMB), the boundary condition derived from the modified stiffness equation and Laplace's equation is as follows (Wu and Wang, 2006):

$$[t_{rr}]^+ = \left(\rho_c - \rho_m\right) g_0 u_r + \left(\rho_c - \rho_m\right) \phi_1 \tag{2.10}$$

in which ρ_c is the density of the core, and ρ_m the density of the mantle just above the core. The Winkler foundation is applied with a foundation stiffness per area of $\left(\rho_c - \rho_m\right) g_0$, in which g_0 is the gravitational acceleration at the CMB. Next to the Winkler foundation, the potential load $\left(\rho_c - \rho_m\right)\phi_1$ needs to be applied at the CMB.

For the solid-fluid internal boundary, at the CMB:

$$[\boldsymbol{\tau} \cdot \hat{r}]_{-}^{+} = \rho_c g_0 u_r \hat{r} \tag{2.11a}$$

Furthermore, the shear stress vanishes at the CMB, there is continuity of displacements, and there are no internal mass loads, leading to (Wu, 2004):

$$[\overrightarrow{u}]_{-}^{+} = 0 \tag{2.11b}$$

$$[\nabla \phi_1 \cdot \hat{r}]_{-}^{+} + 4\pi G[\rho_0]_{-}^{+} u_r = 0 \tag{2.11c}$$

2.3.4. Complete set of boundary conditions

As presented in the previous subsections the boundary conditions couple stress and displacements in the Earth model. A complete set of boundary conditions for the FE method is obtained when the perturbed gravitational potential ϕ_1 is known at all model layer surfaces. Then the stresses and the accompanying displacements of the nodes on the mesh can be determined through numerical analysis. By solving the Laplace equation the perturbed gravitational potential can be found. However, from the Laplace equation follows that the perturbed gravitational potential is a function of the radial displacements. The FE model and the Laplace equation from Equation 2.5 are coupled through the boundary conditions for stress and displacements. Thus, an iterative process is required to solve for the displacements. The iterative process along with the solution to the Laplace equation are explained in more detail in Chapter 4.

With the information gathered on the modified stiffness equation and the boundary conditions the Earth model can be defined and generated using `Abaqus`. The Earth model definition and generation is presented in the next Chapter 3.

3

Model definition and generation

As briefly introduced in the previous chapter, an iterative process is required for the determination of the perturbed gravitational potential and the radial displacements of the nodes on the mesh because they are a function of one another. This iterative process and the solution to the Laplace equation are discussed in detail in Chapter 4. Before these iterations can be performed, the Earth model and the initial forces acting on the model need to be defined and generated. This is done in the `Model_data.py` and `Model_gen.py` Python scripts. The `Model_data.py` script includes parameters that the user can vary, such as the input surface load and the mesh resolution. Subsequently, the `Model_gen.py` script generates the model based on the parameters defined in `Model_data.py`. The Earth model definition for homogeneous Earth models is discussed in Section 3.1 and the model generation in Section 3.2.

3.1. Model definition

This section discusses the definition of the Earth model. The Earth model consists of layers. The layer data, constant parameters, and parameters that the user can vary are discussed in Subsection 3.1.1. The user can also choose for extra options which will be of importance for the model generation. An example of these options is to include eustatic sea level changes depending on the input ice load. The model options are introduced in Subsection 3.1.2.

3.1.1. Model data

The parameters that define the Earth model are loaded or determined in the `Model_data.py` script. The Earth model consists of layers which are defined by their outer radius R, density ρ, shear modulus G, and viscosity μ, defined in `layer_data.txt`. For each layer the Young's modulus and gravitational acceleration at the outer surface can be computed. These are later needed for the material definition and forces definition, respectively. The Young's modulus or elastic modulus E for each layer can be computed as function of the Poisson's ratio ν and the shear modulus G according to:

$$E = 2G(1+\nu) \tag{3.1}$$

The Poisson's ratio is the negative of transverse strain over axial strain. For a perfectly incompressible elastically deformed material the Poisson's ratio would equal 0.5. As explained in Section 2.2 in the FEM analysis it is assumed that the Earth model materials are incompressible, such that instability arising from the internal buoyancy counteracting the restoring force of isostasy is avoided (Wu, 2004). A Poisson's ratio of 0.5-1e-10 is assumed, slightly under 0.5, because `Abaqus` cannot handle Poisson's ratios of 0.5 for the mesh elements used in this research. For incompressibility Equation 3.1 for the Young's modulus then reduces to:

$$E \approx 2G(1+0.5) = 3G \tag{3.2}$$

The gravitational acceleration g_{acc} at the outer surface of each layer can be determined as follows:

$$g_{acc,i} = \left(\frac{4}{3} G\pi R_0^3 \rho_0 + \sum_{j=0}^{i} \frac{4}{3} G\pi \left(R_{j+1}^3 - R_j^3 \right) \rho_{j+1} \right) / R_i^2 \tag{3.3}$$

in which the subscript i and j denote the layer. i runs from 0, the core, to the maximum number of layers N_{layer} minus 1, j runs from 0 to i, and G is the gravitational constant. Note that the symbol G is used for the shear modulus as well as the gravitational constant in this report. Constant parameters that are defined are the density of water ρ_{water} of 1000 kg/m^3, the density of ice ρ_{ice} of 931 kg/m^3, and the amount of seconds in one thousand years, 1 ka. The amount of seconds in one thousand years is 31,557,600,000 s, based on an average of 365.25 days in a year, 24 hours in a day, 60 minutes in an hour, and 60 seconds in a minute. Other parameters that need to be defined and which can be varied are the end of the time steps $Time$ from which the number of steps N_{step} is derived, the distance between the FEM nodes $Seeds$, the creep error tolerance $CETOL$, and the spherical harmonics degree limit $Degree$. In Chapter 6 the relevance of these parameters for the accuracy of the solution will be investigated.

3.1.2. Model options

The user can also choose to include the core of the Earth model, the centrifugal forcing, a surface ice load, a linearly increasing load between time steps, the spherical harmonics degree 0 and 1 of the ice loading, and the change in sea level depending on the ice loading. These options are explained here in more detail.

- When the viscosity of the core equals 0 Pa s, there is no resistance for the fluid core to flow. `Abaqus` cannot easily simulate fluid dynamics. Therefore, the fluid core does not take part in the FE analysis and the centrifugal force is applied to the inner surface of the layer above the core instead of the outer surface of the core layer. This way, the displacements at the CMB are still taken into account even though the core is fluid. The indicator $flag\_lc$ equals 1 for a fluid core and 0 for a solid core. The indicator is of importance for the definition of the direction of the centrifugal force in `Model_gen.py`. A pressure force in `Abaqus` is defined positive for negative volumetric creep, or in other words for compression. One wants the centrifugal force at the CMB to point in the same direction as the centrifugal force at the surface, or intermediate layer interfaces, for a certain colatitude. Since a compressive force applied at the inner surface of the layer above the core points in the opposite direction as a compressive force applied at the outer surface of the layer above the core, and all other layer interfaces, the centrifugal force at the CMB needs to change sign. This is what the parameter $flag\_lc$ takes care of.

  Figure 3.1 presents a schematic overview of the implication of $flag\_lc$ on the direction and the surface used of the centrifugal force for a two-layer Earth model, in which the red arrows perpendicular to the surface represent the direction and magnitude of the centrifugal force. The figure is not to scale. When $flag\_lc$ is 0 the centrifugal force is applied to the outer surface of the core, and when $flag\_lc$ is 1 the centrifugal force is applied to the inner surface of the layer above the core, in this example the mantle.

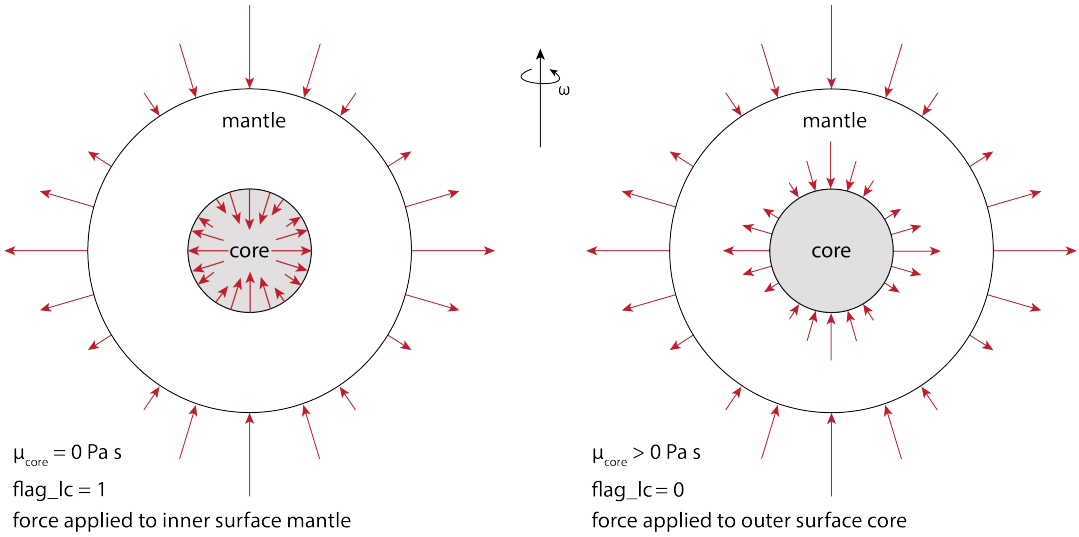

Figure 3.1: Schematic overview of the implication of $flag\_lc$ on the direction and the surface used of the centrifugal force for a two-layer Earth model. The red arrows perpendicular to the surface indicate the direction and magnitude of the centrifugal force. The core is indicated in grey. ω indicates the rotation about the rotational axis.

In the Earth model the core is assumed to be liquid, even though the inner core of the Earth is solid. However, due to the presence of the outer liquid core the layers above the core cannot sense the inner core. Thus, the inner solid core will not have an effect on the displacements and perturbed gravitational potential. `Model_gen.py` can also be used to generate other planetary bodies with a solid core. The description of the model generation procedure will focus on the case in which $flag\_lc$ is 1 since this is the case for the planetary body, the Earth, in this research.

- The centrifugal forcing can be switched off when one is only interested in the effect of surface loading on a non-rotating Earth model. The indicator for this option is $centrifugal\_on$ and equals 1 for including and 0 for excluding the centrifugal force. The surface loading can be switched off when one is only interested in deformations due to a rotating Earth model. However this is not done by assigning a 1 or 0 to a parameter but simply by using a zeros grid as input ice load. Switching certain parts of the code on and off is useful for intermediate testing and verification of the code.

- When applying a surface load on the model at the start of a time step, it can either be increased linearly between the start and the end of the previous time step, or fully applied at the start of the current time step. Figure 3.2 presents a schematic drawing of the instant load on the left and the ramp load on the right for a time step with t_i at the start of the time step and t_{i+1} at the end of the current time step. The way in which the surface load is applied affects the nodal displacements at the start and end of the time step and thus it affects the perturbed gravitational potential. When the time step is sufficiently small between t_{i-1} and t_i the nodal displacements at t_{i+1} for a ramp load will approach the nodal displacements at t_{i+1} for an instant load.

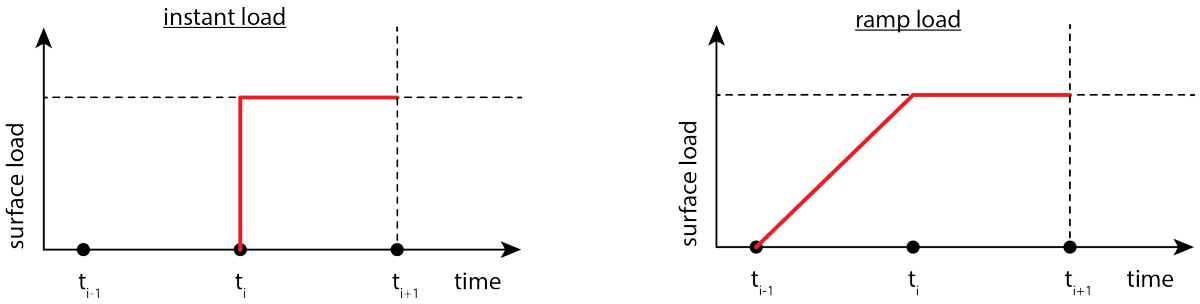

Figure 3.2: Schematic overview of the instant load on the left and the ramp load on the right for a time step with t_i at the start of the time step and t_{i+1} at the end of the time step.

- Due to mass conservation required in the model, either the spherical harmonic degree 0 of the input ice load has to be removed, or the applied ice mass is assumed to come from the ocean, causing sea level change (Wu, 2004). The input ice data is ice height data on an equiangular grid. Together with the radius of the Earth model the areas of the grid cells can be determined. With the ice density ρ_{ice} and the grid cell areas the applied ice mass $M_{ice}(t)$ is computed. The ice-equivalent sea level over the ocean basin $S_0(\theta,\lambda,t)$ is determined from this ice mass by using the density of water ρ_{water}, the total area of the ocean basin A_0, and an ocean mask indicating which grid cells are ocean with 1's and which are land with 0's $O(\theta,\lambda,t)$ according to (Wu, 2004):

$$S_0(\theta,\lambda,t) = -\frac{M_{ice}(t)}{\rho_{water} A_0} O(\theta,\lambda,t) \tag{3.4}$$

Here only eustatic sea level change is considered. Since the applied ice mass is taken from the water mass in the ocean basin at the surface of the Earth model, mass is conserved and thus the spherical harmonic degree 0 of the complete model, the Earth model itself plus the applied ice loads, remains zero. The indicator for the eustatic sea level change is SLE_true and is set to 1 when included. Another reason to not include an ice-equivalent sea level change can be to be able to verify the numerical model which is a simplified representation of reality. In this research the spherical harmonic degree 0 of the ice input load is removed for mass conservation. All the elements are present in the code to use the ice-equivalent sea level change approach. However, this part of the code is not tested in conjunction with true polar wander.

- The spherical harmonic degree 1 should remain zero as well, because there is no interest in the shift of the center of mass (Wu, 2004). The spherical harmonic degree 1 is zero if the center of figure (CF) coincides with the center of mass (CM), or geocenter, of the model. When a non-uniformly distributed surface load is applied the CM will shift with respect to the CF. Benchmarks for surface displacements due to GIA are with respect to the CM. When incorporating geocenter motion, the CM needs to be updated per time step and per iteration. The CM will shift slightly due to the nature of FEM, because it is a discretization of a continuous model, which introduces numerical errors. The measured and predicted geocenter motion due to GIA is in the order of sub mm per year, whilst the measured and predicted surface radial displacement due to GIA is in the order of cm per year (Wu et al., 2012). The geocenter motion is not negligible but is for these reasons not taken into account here. The indicator for removing the degree 0 and 1 spherical harmonics is $Disable\_SH\_0\_1$ and set to 1 when removing degree 0 and 1. When there is opted for an ice-equivalent sea level change there is the parameter $Disable\_SH\_1$ to only remove degree 1. In this research both the spherical harmonic degrees 0 and 1 of the input ice load are removed.

3.2. Model generation

Now that the model layers are defined, the model can be build in `Abaqus` using the `Model_gen.py` script. The parts created from the layer data is discussed in Subsection 3.2.1, the layer material and its viscoelastic behavior in Subsection 3.2.2, the parts assembly and the mesh generation in Subsection 3.2.3, the viscoelastic time step definition in Subsection 3.2.4, the application of the Winkler foundation in Subsection 3.2.5, the pressure application from the centrifugal potential in Subsection 3.2.6, the pressure application from the input surface load in Subsection 3.2.7, and at last the analysis job definition in Subsection 3.2.8.

3.2.1. Layer parts creation

Parts are the building blocks of an `Abaqus` model. First the core of the Earth model is generated. The sketch mode is opened and a construction line at $x = 0$ and a fixed constraint at the origin of the sketch are created. A half circle arc is drawn between $(x, y) = (0, R_0)$ and $(x, y) = (0, -R_0)$ with its center at the origin of the sketch. The 3-D deformable part L_0 is created by revolving the sketch 360° around the $x = 0$ construction line. For meshing reasons later on the spherical core part is partitioned into 8 identical sized pieces by using 3 partitions: one in the y-z plane, one in the x-y plane, and one in the x-z plane. Figure 3.3 presents the partitioning of the core using three perpendicular planes.

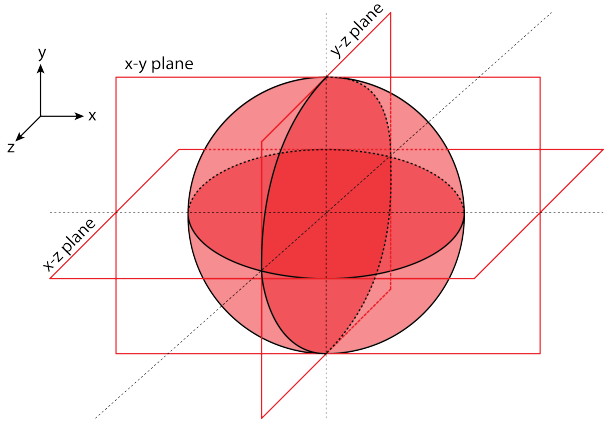

Figure 3.3: Partitioning of the core using three perpendicular planes.

For the L_0 part a node set $Center$ is created for the center of the model consisting of one node at $(x, y, z) = (0, 0, 0)$. A surface $Sout_0$ is created being the outer surface of the core. Subsequently, all defined layers are created per layer, starting from the layer closest to the core to the most outer layer. The sketch mode is opened and a construction line at $x = 0$ is created. A half circle arc is drawn between $(x, y) = (0, R_{i-1})$ and $(x, y) = (0, -R_{i-1})$ and another half circle between $(0, R_i)$ and $(x, y) = (0, -R_i)$, both with their center at the origin of the sketch. The subscript i denotes the layer, running from 0 for the core to the maximum number of layers N_{layer} minus 1 for the most outer layer. Two lines are drawn between $(x, y) = (0, -R_{i-1})$ and $(x, y) = (0, -R_i)$, and

between $(x, y) = (0, R_{i-1})$ and $(x, y) = (0, R_i)$. The 3-D deformable parts L_i are created by revolving the sketch 360° around the $x = 0$ construction line. Each layer part is a spherical shell. As the core the subsequent layers are also partitioned for meshing reasons. For each layer two surfaces are defined, the surface at the inner radius Sin_i and the surface at the outer radius $Sout_i$. The surfaces need to be defined for the application of pressure loads from the centrifugal potential, the surface load, and the perturbed gravitational potential.

3.2.2. Viscoelastic material definition

Now that the layers are built in terms of parts, material properties need to be assigned to these parts. The materials need to be assigned to sections, which in their turn need to be assigned to the previously created layer parts L_i. For each layer, including the core, materials M_i are created. The initial elasticity is defined for all layers using the Young's modulus and Poisson's ratio (Abaqus, 2014). The density from the input layer data is also assigned to the material. When the viscosity of the layer is larger than 0 Pa s and smaller than 1e40 Pa s, a viscoelastic material is created based on a Prony series expansion of the dimensionless shear relaxation modulus according to (Abaqus, 2014):

$$g_R(t) = 1 - \sum_{i=1}^{N} \bar{g}_i^p \left(1 - e^{-t/\tau_i^G}\right) \tag{3.5}$$

in which the number of terms N, the modulus ratio of the shear relaxation modulus of term i $\bar{g}_i^p$, and the relaxation time for the ith term τ_i^G with $i = 0,1,...,N$ are material properties. (Hu et al., 2017a) showed that the viscoelastic behavior is better modeled with the Prony series expansion using the "Viscoelastic" option than with the power law strain-hardening using the "Creep" option. Both the "Creep" and "Viscoelastic" options give accurate results for the time history of the inertia tensor components. However, for the computation of true polar wander, a combination of components of the inertia tensor is used and these combined terms do contain a large error when using the "Creep" option. Thus, for this research, in which true polar wander is the focus, the "Viscoelastic" option in `Abaqus` is used to define the viscoelastic material property.

For a Maxwell rheology N equals 1, thus the modulus ratio and the relaxation time for only the first term need to be defined. Since only one term is considered $\bar{g}_1^p$ equals 1. `Abaqus` can only handle values between 0 and 1 and thus $\bar{g}_1^p$ is set to 1-1e-10, a value slightly smaller than 1. The relaxation time of the first term τ_1^G is a direct relation between the viscosity μ and the Young's modulus E:

$$\tau_i^G = \frac{\mu}{G} = \frac{3\mu}{E} \tag{3.6}$$

This relation is valid for incompressibility as shown in Equation 3.2. Next to the Prony series of the dimensionless shear relaxation modulus the Prony series of the dimensionless bulk relaxation modulus needs to be specified. The bulk modulus describes the compressibility of a material under external pressure. As previously explained incompressibility is assumed. Thus, for the specification of the Prony series expansion of the dimensionless bulk relaxation modulus the modulus ratio of the first term in the series expansion $\bar{k}_1^p$ is set to zero. Now that the materials per layer M_i are defined, sections per layer S_i are created and the materials are assigned to these homogeneous solid sections. Subsequently the section S_i are assigned to the parts L_i.

3.2.3. Assembly and mesh generation

The next step is to assemble the parts and generate the mesh to discretize the continuous model. First a spherical local coordinate system is created with respect to the global coordinate system for the assembly. The local x-axis points in the global z-axis direction, the local y-axis in the global x-axis direction, and the local z-axis in the global y-axis direction, as shown in Figure 3.4.

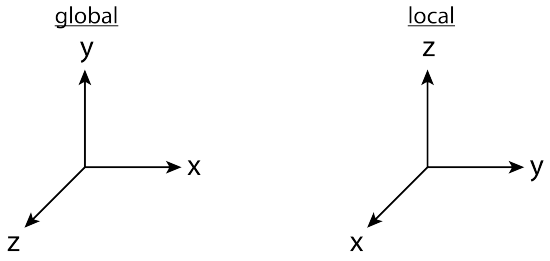

Figure 3.4: Global and local coordinate systems.

The local coordinate system is more intuitive than the global coordinate system for true polar wander, since now the x-axis points in the equatorial plane from the Earth's center of mass towards the Greenwich meridian which defines 0° longitude, the y-axis points in the equatorial plane from the Earth's center of mass towards 90° East longitude, and the z-axis or rotational axis now points upwards, completing the right-handed coordinate system.

To be able to assemble the layer parts, part instances I_i need to be created. A part instance is a representation of the original part. The instances are positioned relative to each other in the local coordinate system and then the assembly is created from merging of the instances. A new part called $Earth$ is created, which consists of all the instances in the assembly.

Before the meshing procedure the mesh element types are defined. Mesh elements have their own code based on their characteristics. For this research the C3D8RH mesh elements are used. 'C' specifies that continuum elements are used and '3D' that they are three-dimensional. For incompressible material, or close to incompressibility, hybrid mesh elements need to be used, indicated with 'H'. For an element with incompressible material characteristics its volume cannot change under pressure. The pressure stress cannot be computed from the displacements of the nodes. Hybrid elements can determine the pressure stress in the elements directly because they use an additional degree of freedom. Furthermore, the number of nodes of the element need to be specified, the number after '3D', and one can opt for reduced integration 'R'. Only quadrilateral and hexahedral elements can use a reduced-integration scheme. In reduced integration one fewer integration point in each direction is used than fully integrated elements. This reduces the integration time. However, reduced integration may require a higher mesh resolution for accurate results depending on a distortion within the elements called hourglassing. Although `Abaqus` does have automatic enhanced distortion control for hourglassing and this rarely causes a problem (Abaqus, 2014).

Next to the mesh element types, the shape of the elements and the meshing technique needs to be defined. As previously described the model is partitioned. The three-dimensional model is divided into smaller and thus simpler regions. This is done for meshing reasons because this allows for the use of exclusively hexahedral elements, any polyhedron with six surfaces. When the model is not partitioned, only tetrahedral elements, a polyhedron with four triangular surfaces, can be used using the free meshing technique. Tetrahedral elements are useful because they can fit complex geometries, but that is not necessary for the partitioned spherical model. A reason to use hexahedral elements over tetrahedral elements is that for tetrahedral elements volumetric locking can take place for incompressible, or close to incompressible, materials. Volumetric locking causes the elements to act stiffer than they actually are, which results in underestimated stresses and strains in the elements (Abaqus, 2014). Figure 3.5 shows the shapes of a tetrahedral mesh element, and two different hexahedral mesh elements.

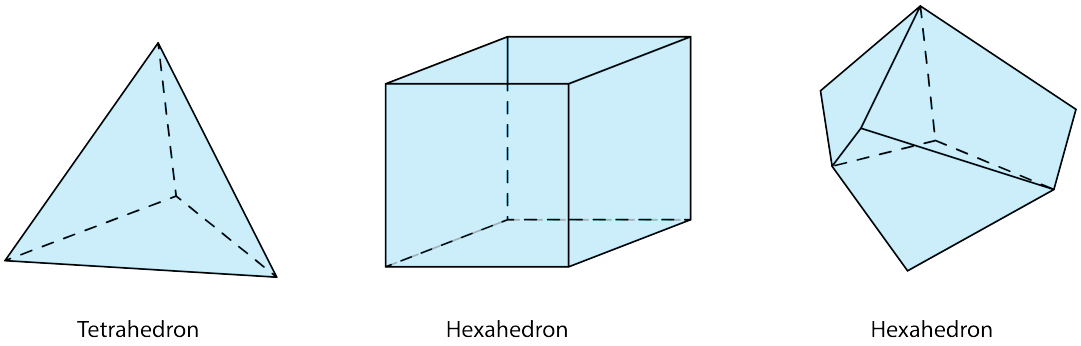

Figure 3.5: Shape of tetrahedral mesh elements and hexahedral mesh elements.

For hexahedral elements a structured meshing technique is used, meaning that simple predefined mesh topologies are transformed onto the geometry of the desired region to be meshed. The mesh is created with the previously defined parameter *Seeds* from `Model_data.py` which describes the desired distance between the nodes, or the desired size of the edges of the mesh elements. Furthermore, the deviation factor, which defines how much the size of the element edge is allowed to deviate from the desired edge size, is set to 0.1. This will result in hexahedral elements which are close to the shape of a cube.

With these mesh settings the $Earth$ part, consisting of all layers excluding the core part, and separately the core part L_0 with a larger element edge size are meshed. For the Earth a liquid core is assumed and forces are applied to the inner surface of the layer above the core Sin_1 instead of on the outer surface of the core $Sout_0$. The core is still meshed to take into account the incompressibility of the core. The displacements do not change when the core is not in the model at all. However, when one is interested in the movement of the center of mass of the model, thus the spherical harmonics of degree 1, the core needs to be included. It is therefore left in the model, for larger flexibility of the code. Since for the Earth the displacements within the core are not of interest, the core can be meshed with a coarse resolution. Therefore the desired element edge size $Seeds$ for the core is set to twice the value used for the other layers. The displacements at the CMB come from the displacements of the nodes on the surface of the layer above the core Sin_1.

The two meshed parts, $Earth$ and L_0, are tied together such that all active degrees of freedom are equal for the outer surface of the meshed core and the inner surface of the meshed Earth excluding the core.

3.2.4. Viscoelastic time step definition

Before applying the initial forces for each time step on the model, a boundary condition is created in which all degrees of freedom for the node set $Center$ of L_0, consisting of one node at the origin, are set to zero. The node at the origin of the coordinate system representing the center of figure of the Earth model is fixed at the start of the simulation. Next, the time steps are defined from the $Time$ array defined in `Model_data.py`. The $Time$ array defines the end of each step. Thus, the length of the first time step $step_1$ equals the difference between the initial zero time t_0, predefined in `Abaqus`, and the first element of $Time$ t_1. The length of the second time step $step_2$ equals the difference between the end of the first and second time step, and so on. Figure 3.6 presents the definition of the time steps from the $Time$ array.

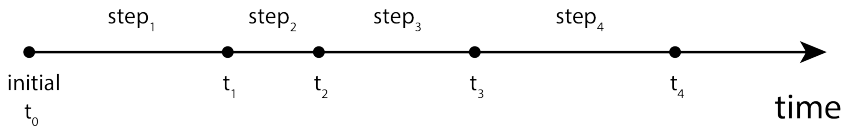

Figure 3.6: Definition of the time steps $step_i$ from the $Time$ array and the time indices t_i at the end of each time step.

The time steps are viscoelastic, meaning that a transient static response is obtained with a time-dependent material behavior. Furthermore, in the definition of the time steps module, time increments need to be defined (Abaqus, 2014). `Abaqus` is based on numerical integration and uses explicit dynamic integration for this problem. Thus, sufficiently small time increments within a time step are required to allow for a stable solution. The selection of the initial, minimum, and maximum increment size, and the maximum number of increments within a step is a matter of trial and error. As a start the initial increment size is set to 1% of the time step size, the minimum increment size to 0.00001% of the time step size, the maximum increment size to 4% of the time step size, and the maximum number of increments to 500. One can play around with these settings.

Also, the creep error tolerance needs to be defined. This tolerance needs to be defined such that the increments in stress $\Delta\sigma$ are determined with sufficient accuracy. For a one-dimensional case, the stress increment is related to the strain increments according to (Abaqus, 2014):

$$\Delta\sigma = E\Delta\epsilon^{el} = E\left(\Delta\epsilon - \Delta\epsilon^{cr}\right) \tag{3.7}$$

in which E is the elastic modulus, and $\Delta\epsilon^{el}$, $\Delta\epsilon$, and $\Delta\epsilon^{cr}$ the uniaxial, total, and creep strain increments, respectively. For the stress increment $\Delta\sigma$ to be accurate, the error in the creep strain increment $\Delta\epsilon^{cr}_{err}$, the maximum difference in the creep strain increment calculated from the creep strain rates at the beginning and end of the increment, should be small compared to the uniaxial strain increment $\Delta\epsilon^{el}$. Thus, the error in the creep strain increment $\Delta\epsilon^{cr}_{err}$ or creep error tolerance $CETOL$ is based on the following relation:

$$CETOL = \Delta\epsilon^{cr}_{err} << \Delta\epsilon^{el} = \frac{\Delta\sigma}{E} \tag{3.8}$$

To define $CETOL$ an acceptable stress error tolerance has to be chosen. $CETOL$ will therefore be a small fraction of the typical stress over the elastic modulus. This approach for selecting $CETOL$ is conservative. A typical value is 1e-3 to 1e-5 and its effect on the accuracy of the solution will be investigated.

3.2.5. Winkler foundation application

The last step before the pressure load application from the centrifugal potential and from the input surface load, is the application of the Winkler foundation. The Winkler foundation ensures that the reaction forces of the elastic foundation are linearly proportional to the displacement at any point. This is simulated by attaching elastic springs at the interfaces. The foundation is valid for all time steps. For the interfaces the elastic foundation is applied to the inner surface of the layer $i+1$ with a foundation stiffness of $\left(\rho_i - \rho_{i+1}\right) g_{acc,i}$, in which i denotes the layer, and $g_{acc,i}$ the gravity at layer surface i. The foundation stiffness is as defined in the boundary conditions in Section 2.3 in Equation 2.8, 2.10 for the solid-solid internal boundaries and the CMB, respectively. For the surface of the Earth model the elastic foundation is applied to the outer surface of the outer most layer with foundation stiffness of $\rho_s g_{acc,s}$, in which s denotes the surface of the model, as defined in Equation 2.6. The density outside the model, thus of Earth's atmosphere, is assumed to be negligible. Note that when the densities of two layers are equal, the density difference is zero, and thus from the Winkler foundation follows that there will be no displacements of the nodes of that layer surface.

3.2.6. Pressure application from centrifugal potential

The last step in the model generation is the application of pressure loads from the centrifugal potential and input surface load. First the application of the pressure load from the centrifugal potential is discussed. The centrifugal potential ϕ_c at the surface of the Earth model is defined as follows:

$$\begin{aligned}\phi_c &= -\frac{1}{2}\Omega^2 R_s^2 \sin^2\theta \\ &= \frac{1}{3}\Omega^2 R_s^2 \left(\frac{1}{2}(3\cos^2\theta - 1)\right) - \frac{1}{3}\Omega^2 R_s^2 \\ &= \frac{1}{3}\Omega^2 R_s^2 P_{2,0}(\cos\theta) - \frac{1}{3}\Omega^2 R_s^2\end{aligned} \tag{3.9}$$

in which Ω is the Earth's rotational rate, R_s the mean radius of the Earth's surface, θ the colatitude, and $P_{2,0}(\cos\theta)$ the associated Legendre function of degree 2 and order 0. The last term $-\frac{1}{3}\Omega^2 R_s^2$ in the above equation of the centrifugal potential can be ignored because it is pure dilatation due to its symmetry with the radius. In `Abaqus` an expression field is created relative to the local coordinate system based on $P_{2,0}(\cos\theta)$. The centrifugal potential is then applied as a pressure load at each of the layers. For a liquid core the pressure from the centrifugal potential at the CMB $p_{c,0}$ is applied to the inner surface of the layer above the core Sin_1 according to:

$$\begin{aligned}p_{c,0} &= (-1)^{flag\_lc}\phi_c\left(\rho_0 - \rho_1\right)\frac{R_0^2}{R_s^2} \\ &= -\phi_c\left(\rho_0 - \rho_1\right)\frac{R_0^2}{R_s^2}\end{aligned} \tag{3.10}$$

in which 0 indicates the core, and 1 the layer above the core, not to be confused with the hydrostatic and perturbed state from Chapter 2. The pressure is in the form of the second term of Equation 2.10 (Wu and Wang, 2006), $\left(\rho_0 - \rho_1\right)\phi$, representing a boundary condition at the CMB. The term R_0^2/R_s^2 is introduced to scale the centrifugal potential at the surface of the Earth model defined in Equation 3.9 to the centrifugal potential at the radius of the layer surface of interest. The negative sign ensures that the pressure at the CMB will point in the same direction as the pressure at all other layers, as explained in Subsection 3.1.2. The pressure from the centrifugal potential at the solid-solid internal boundaries is applied to the outer surfaces of the layer according to:

$$p_{c,i} = \phi_c\left(\rho_i - \rho_{i+1}\right)\frac{R_i^2}{R_s^2} \tag{3.11}$$

in which ρ_i is the density of the layer to which the pressure is applied, ρ_{i+1} the density of the layer above the considered layer, and R_i the outer radius of the considered layer. This pressure is in the form of the second term of Equation 2.8 (Wu, 2004), $\left(\rho_i - \rho_{i+1}\right)\phi$. The pressure from the centrifugal potential at the surface of the model as in Equation 2.6 (Wu, 2004), $\rho_s\phi$, equals:

$$p_{c,s} = \phi_c \rho_s \tag{3.12}$$

in which the subscript s indicates the surface of the Earth model.

3.2.7. Pressure application from input surface load

Now that the pressure from the centrifugal potential is applied, the pressure from the input ice loading can be applied to the surface of the most outer layer of the model. Here the option for an ice-equivalent sea level change is discussed, along with the removal of the spherical harmonic degree 0 and 1, followed by the pressure application from the input ice load, and potentially from the sea load.

Ice-equivalent sea level change

The input ice load has to be ice heights per time step on an equiangular grid with equal resolution in longitude $d\lambda$, from 0° to 360°, as in colatitude $d\theta$, from 0° to 180°. Before the surface load is applied the ice-equivalent sea level is determined from the input ice load when there is chosen for an ice-equivalent sea level change. The ice height data is loaded and the grid resolution, the constant step size in longitude and colatitude, $d\lambda$ and $d\theta$ respectively, is determined from the number of elements in longitude or latitude. The ice heights are given at specific locations of colatitude and longitude (θ,λ), but to find the total ice input mass the surface mass density at the grid cells is required. This means that grid cell areas need to be determined. The total ice input mass per time step $M_{ice}(t)$ is dependent on the ice heights on the grid $h(\theta,\lambda,t)$, or surface mass density $\sigma(\theta,\lambda,t)$, according to:

$$\begin{aligned} M_{ice}(t) &= \iint_{\Omega} \sigma(\theta,\lambda,t)\, d\Omega \\ &= \rho_{ice} \iint_{\Omega} h(\theta,\lambda,t)\, d\Omega \end{aligned} \tag{3.13}$$

in which Ω is the sphere of radius R and $d\Omega$ the area of the surface element described by:

$$d\Omega = R^2 \sin\theta\, d\theta\, d\lambda \tag{3.14}$$

Figure 3.7 presents a discrete visualization of a part of the Earth with in grey the area where the mass load is located on a longitude-latitude grid. This region and its elements $d\Omega$ are dependent on latitude. The ice heights at the grid points need to be assigned to grid cells. It is assumed that the grid points are located at the left side of the grid cells. The ice heights specified at the grid points at 0° and 360° longitude are equal and thus they only need to be taken into account once. Note that the ice heights at the grid points at 0° colatitude should be equal to each other because they represent the same grid point, namely the north pole. The same accounts for the ice heights at the grid points at 180° colatitude representing the south pole. Figure 3.8 presents how the grid cells are defined and to which grid cells the grid points are assigned to.

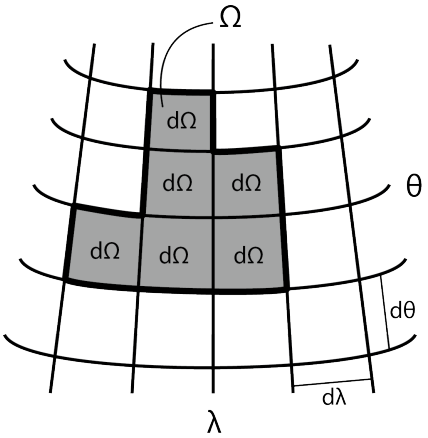

Figure 3.7: Discrete visualization of a part of the Earth with in grey the area where the mass load is located Ω. Also shown are the area elements $d\Omega$ on a longitude-latitude grid with step sizes $d\theta$ in colatitude and $d\lambda$ in longitude.

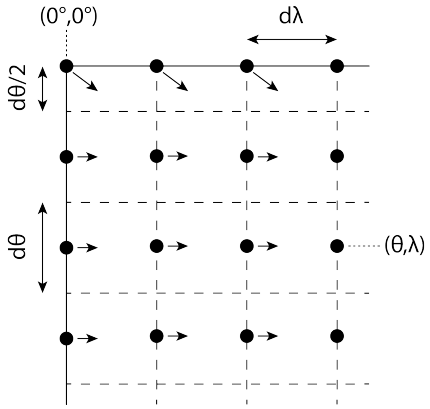

Figure 3.8: Grid of ice heights at specific locations (θ,λ) and corresponding grid cell area. The black dots represent the grid points and the dashed lines represent the boundaries of the grid cells. The arrows indicate to which grid cell the grid point is assigned to.

The boundaries of the grid cells lie $d\theta/2$ above and $d\theta/2$ below the grid point in latitude, except for the north pole and south pole grid points as shown in Figure 3.8. It seems as if the grid cells for the north pole grid point are half the size of the other grid cells, but this is not true because the Earth is a sphere. The area of a grid cell $d\Omega$ is dependent on latitude and is determined through:

$$\begin{aligned} d\Omega(\theta,\lambda) &= A_s \frac{\cos(\theta_u) - \cos(\theta_l)}{2n_{long}} \\ &= 4\pi R_s^2 \frac{\cos(\theta_u) - \cos(\theta_l)}{2n_{long}} \end{aligned} \tag{3.15}$$

in which A_s is the surface area of the model which equals $4\pi R_s^2$, θ_u the colatitude at the upper boundary of the cell, θ_l the colatitude at the lower boundary of the cell, and n_{long} the number of grid points in longitudinal direction, taking into account that 0°/360° longitude is only used once. Note that grid cell areas are equal for equal longitude. The total ice mass $M_{ice}(t)$ from the input ice data per time step is then determined using Equation 3.13, so by multiplying the ice heights at the grid points $h(\theta,\lambda,t)$ with their corresponding grid cell areas $d\Omega(\theta,\lambda)$ and the density of ice ρ_{ice}, and summing up the obtained ice masses from each grid point.

From the total ice mass input, the grid of ocean heights $S_0(\theta,\lambda,t)$ can be determined. First an ocean mask $O(\theta,\lambda,t)$ is created, derived from the ice input data, in which at the grid points 1's indicate ocean and 0's indicate ice. For now the Earth is assumed to be ocean except for the location of ice masses. Realistic ocean basins can be build in without much effort. The ocean mask is multiplied with the grid of grid cell areas $d\Omega(\theta,\lambda)$ to find the total area of the ocean A_0. Then, as previously introduced in Subsection 3.1.2 the grid of ocean heights can be computed according to (Wu, 2004):

$$S_0(\theta,\lambda,t) = -\frac{M_{ice}(t)}{\rho_{water} A_0} O(\theta,\lambda,t) \tag{3.16}$$

in which ρ_{water} is the density of water. The minus sign indicates a sea level height loss due to a positive ice input mass. Note that for a changing input ice load over the time steps, the total ice mass for that time step will change, and thus also the sea level is time-dependent. An ocean mask based on realistic ocean basins can assumed to be time-independent.

Spherical harmonic degree 0 and/or 1 removal

When one does not want to incorporate the ice-equivalent sea level change, mass conversation can be ensured by removing the degree 0 spherical harmonic coefficient from the input ice data, as briefly explained in Subsection 3.1.2. Spherical harmonics are solutions of the spherical Laplace equation, thus they are an adaption of Fourier analysis to a function on a sphere. The superposition of spherical harmonics can be used to represent physical phenomena, such as the gravitational potential or a surface load, distributed on the surface of a sphere (Heiskanen and Vening Meinesz, 1958). Equation 3.17 presents the surface spherical harmonics $Y_{l,m}(\theta,\lambda)$ as function of the associated Legendre polynomials $P_{l,m}(\cos\theta)$:

$$Y_{l,m}(\theta,\lambda) = P_{l,|m|}(\cos\theta) \begin{cases} \cos m\lambda & \text{if m} \geq 0 \\ \sin |m|\lambda & \text{if m} < 0 \end{cases} \tag{3.17}$$

in which l is the degree, m the order, θ the colatitude, and λ the longitude of a point on a sphere. Different harmonics can be described: zonal, sectorial, and tesseral. Figure 3.9 shows the spatial features of zonal, sectorial, and tesseral harmonics, and for which degree and order they occur.

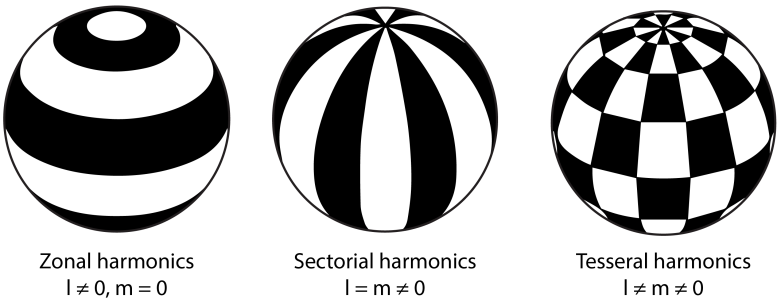

Figure 3.9: Zonal (left), sectorial (center) and tesseral (right) surface spherical harmonics.

The associated Legendre polynomials are normalized to ensure stability. Normalized parameters are indicated with a bar. Different normalizations techniques exist. For now the normalization technique is not of importance, but is shown to be of importance in Chapter 6. Any function $f(\theta,\lambda)$ defined on a sphere can be uniquely represented as a series of surface spherical harmonics:

$$f(\theta,\lambda) = \sum_{l=0}^{\infty} \sum_{m=-l}^{l} \bar{C}_{l,m}^{(f)} \bar{Y}_{l,m}(\theta,\lambda) \tag{3.18}$$

in which $\bar{C}_{l,m}^{(f)}$ are normalized spherical harmonic coefficients of the function $f(\theta,\lambda)$. Because the associated Legendre polynomials are normalized, and thus also the surface spherical harmonics following from Equation 3.17, the spherical harmonic coefficients are normalized accordingly. From Equation 3.18 follows that any function on a sphere $f(\theta,\lambda)$ can be decomposed in spherical harmonic coefficients according to:

$$\bar{C}_{l,m}^{(f)} = \iint_{\Omega} f(\theta,\lambda)\, \bar{Y}_{l,m}(\theta,\lambda)\, d\Omega \tag{3.19}$$

Using the `Python` open source `SpherePy` package (Direen, 2015), based on the above method, the surface load in the spatial domain can be converted to the spectral domain in spherical harmonic coefficients. Note that `SpherePy` requires the input grid to be from 0° to 360° longitude. The degree 0 spherical harmonic coefficient $\bar{C}_{0,0}$ is related to the mass of the surface load. To ensure mass conservation the degree 0 coefficient is extracted from the complete field of coefficients and is converted back to the spatial domain, and subsequently subtracted from the original surface load grid.

When there is no interest in the shift of the center of mass, the spherical harmonic coefficients of degree 1, being $\bar{C}_{1,-1}$, $\bar{C}_{1,0}$, and $\bar{C}_{1,1}$, should be removed as well, as previously explained in Subsection 3.1.2. For this research, there is no interest in the shift of the center of mass and thus the degree 1 coefficients are removed. Since for this research the ice-equivalent sea level is not used the degree 0 and degree 1 coefficients are extracted from the spectral domain of the surface load simultaneously, converted back to the spatial domain, and subsequently subtracted from the original surface load grid.

Pressure application

Now that the mass is conserved in the model and the shift of the center of mass from the surface loading is removed, the surface load can be applied to the model as a pressure load. Force fields need to be created for each time step which depend on the input ice heights. Total load fields per time step are created based on the total input ice load in the local coordinate system. For all time steps the pressure is applied only to the outer surface of the model, since the input loads are surface loads. The pressure field from the surface load p_L is a function of the ice heights, density of ice, and gravitational acceleration at the surface of the model:

$$p_L = h_{ice}\rho_{ice}g_{acc,s} \tag{3.20}$$

The load can be applied instantly or linearly increasing during the time step as introduced in Subsection 3.1.2 and as shown in Figure 3.2. When there is chosen for the linearly changing load, also force fields are created based on the difference in surface loads between time steps. These force fields are applied using the tabular amplitude setting in `Abaqus` (Abaqus, 2014). For the first time step that a surface load is present, the load is increased over the previous time step. For subsequent steps the load is increased or decreased depending on the whether the surface load is larger or smaller relative to the previous step. Figure 3.10 shows a timeline of the applied surface load in which the red colored areas represent the total load fields and the white areas under the red curve the load difference fields.

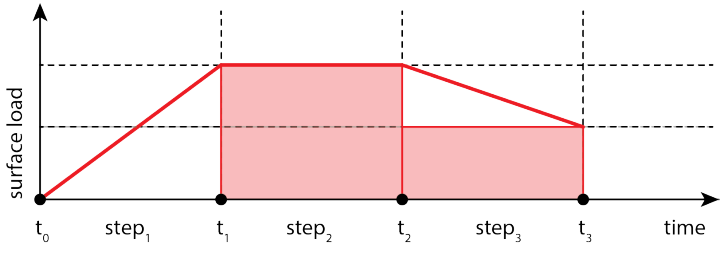

Figure 3.10: Timeline of the applied surface load in which the red colored areas represent the total load fields and the white areas under the red curve the load difference fields.

When a pressure load is created in Abaqus in a specific time step, it is automatically propagated to all coming time steps. For the pressure from the surface load it is of importance to deactivate the load in all coming time steps, since the load is newly defined for each time step.

3.2.8. Analysis job definition

The model with its initial forces for each time step is now fully defined and generated. The last step before starting the iteration procedure, in detail explained in the next Chapter 4, is to create the analysis job and specify the desired output of the analysis. For the analysis job the name of the job and the model are required inputs. Optional inputs are for example the time to wait before submitting the job, whether to print specific data, the number of CPUs to use for the analysis if parallel processing is available, and the amount of memory available to the analysis. The job thus provides control over the analysis. The desired output of the analysis are the nodal displacements in x-, y-, and z-direction. Node-based output is by default given in the global coordinate system.

4

Coupling of FE model to Laplace equation

The model is defined and generated according to the `Model_data.py` and `Model_gen.py` scripts as described in Chapter 3. This means that the FE analysis is ready to be performed from the `Iter.py` script. As introduced in Section 2.3 the perturbed gravitational potential ϕ_1 needs to be known at the layer surfaces to have a complete set of boundary conditions and thus to be able to determine the radial displacements in the model from the stresses. By solving the Laplace equation the perturbed gravitational potential can be found. However, the perturbed gravitational potential is a function of the radial displacements. The FE model and the Laplace equation are coupled through the boundary conditions for stress and displacement. Thus, an iterative process is required to solve for the radial displacements. This chapter describes the iterative process between the nodal displacements and the perturbed gravitational potential to find a converged solution, performed in the `Iter.py` and the subroutine `sph_tools_TPW.py` scripts.

The output of the FE analysis are the displacements at all the nodes in x-, y-, and z-direction in the global coordinate system. The nodal displacements at the layer surfaces need to be converted to a grid of radial displacements in the local coordinate system per time step. The displacements conversion is presented in Section 4.1. For verification purposes and for the later implementation of true polar wander, the change in moment of inertia of the body, needs to be known. Section 4.2 describes how to the change in moment of inertia of the model is derived from the radial displacements. The perturbed gravitational potential is a function of the radial displacements at the layer surfaces through the Laplace equation. The solution to the Laplace equation is presented in Section 4.3. For the coupling of the FE model and the Laplace equation an iterative process is required. The iterative process to compute the converged displacements and perturbed gravitational potential is discussed in Section 4.4. Information on the existing `Python` scripts on author and purpose is presented in Section 4.5.

4.1. Grid of radial displacements from FE analysis output

The total number of iterations are set before the start of the iterative procedure. The number of iterations required for a converged solution depends on the model and the applied forces. This is a matter of trial and error and testing, and will be investigated in Chapter 6. The analysis job is submitted and the FE analysis is performed. Depending on the viscosities of the model layers and the forces on the model `Abaqus` might not be able to find a stable solution at the time increments of the numerical integration due to the increment settings. This can be avoided by reducing the minimum allowed time increment or increasing the creep error tolerance, both defined in `Model_gen.py`. However, one should not set the minimum allowed time increment to a small value to begin with to avoid that `Abaqus` takes smaller time increments than is required for a stable solution. Smaller time increments lead to more time increments within a time step and thus to a longer simulation time.

The output of the FE analysis are the displacements at all the nodes in x-, y-, and z-direction in the global coordinate system. Subsection 4.1.1 describes how to convert these displacements at the layer surfaces to radial displacements. Subsection 4.1.2 presents the procedure for interpolating the obtained radial displacements in the global coordinate system to an equiangular grid in the local coordinate system. An equiangular grid is required for the determination of the spherical harmonic coefficients of the radial displacements.

4.1.1. Radial displacements at layer surfaces

The output of the FE analysis are the displacements at all the nodes in x-, y-, and z-direction in the global coordinate system. The nodes at the layer surfaces are extracted. For these nodes the displacements in x-, y-, and z-direction are converted to radial displacements u_r according to:

$$\begin{aligned} u_r &= |\bar{x}'| - |\bar{x}| = \frac{(|\bar{x}'| - |\bar{x}|)(|\bar{x}'| + |\bar{x}|)}{|\bar{x}'| + |\bar{x}|} = \frac{|\bar{x}'|^2 - |\bar{x}|^2}{|\bar{x}'| + |\bar{x}|} \\ &= \frac{2xu_x + 2yu_y + 2zu_z}{\sqrt{(x+u_x)^2 + (y+u_y)^2 + (z+u_z)^2} - \sqrt{x^2+y^2+z^2}} \\ &\approx \frac{2(xu_x + yu_y + zu_z)}{2\sqrt{x^2+y^2+z^2}} = \frac{\bar{x} \cdot \bar{u}}{|\bar{x}|} \end{aligned} \tag{4.1}$$

in which $\bar{x} = (x, y, z)$ is the initial nodal position, $\bar{u} = (u_x, u_y, u_z)$ is the nodal displacement, and $\bar{x}' = (x + u_x, y + u_y, z + u_z)$ is the nodal position after the displacement. One approximation made in the above derivation is that the nodal displacement is much smaller than the initial nodal position $\bar{u} << \bar{x}$. In this research on the implementation of polar wander the Earth model starts out being spherical. Due to that the Earth is rotating the Earth is flattens to an equilibrium shape after a long time period. The Earth radius at the poles will be slightly smaller and at the equator slightly larger than the radius of the initial spherical Earth. From observations it is known that the equatorial radius of the Earth is approximately 6378 km and the polar radius approximately 6357 km (Jeffreys, 1924). With respect to the spherical model with a radius of 6371 km, there will be nodal displacements in the order of 14 km. However, a displacement of 14 km is still only 0.2% of the radius of the model, and thus the assumption $\bar{u} << \bar{x}$ is justified. Glaciation-induced displacements are in the order of meters, which is negligible compared to the radius of the model, and thus this will not affect the assumption. The nodal radial displacements are saved in a file along with the Cartesian coordinates of the nodes, arranged per time step for all layers.

4.1.2. Grid of radial displacements in local coordinate system

The subroutine in `sph_tools_TPW.py` is started and the list of radial displacements in the global coordinate system is converted to a grid of radial displacement in the local coordinate system for each time step and each layer surface using the `block_gen` function. The local coordinate system, shown in Figure 3.4, is more intuitive for polar wander as explained in Subsection 3.2.3. Furthermore, the Cartesian coordinates of the nodes need to be converted to spherical coordinates to be able to create an equiangular grid of the nodal displacements by means of interpolation. Figure 4.1 and Equation 4.2 present the relation between the Cartesian and spherical coordinates.

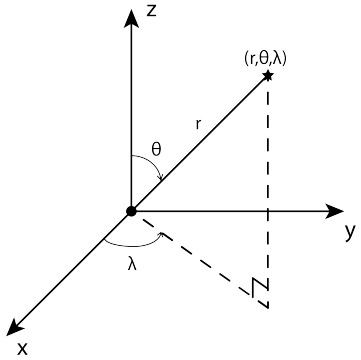

$$\begin{aligned} r &= \sqrt{x^2+y^2+z^2} \\ \theta &= \arccos\left(\frac{z}{r}\right) \\ \lambda &= \arctan2\left(\frac{y}{x}\right) \end{aligned} \tag{4.2}$$

Figure 4.1: Relation between the Cartesian (x,y,z) and spherical (r,θ,λ) local coordinate systems.

in which r is the distance from the origin of the coordinate system to the node, θ the colatitude, and λ the longitude of the node. To obtain the spherical coordinates in the local coordinate system the coordinates in the global coordinate system are used as follows in Equation 4.2:

$$
\begin{aligned}
r &= \sqrt{x^2 + y^2 + z^2} \\
\theta &= \arccos\left(\frac{y}{r}\right) \\
\lambda &= \arctan2\left(\frac{x}{z}\right)
\end{aligned}
\tag{4.3}
$$

Thus, Equation 4.3 uses the Cartesian coordinates in the global coordinate system (x,y,z) to obtain the spherical coordinates (r,θ,λ) in the local coordinate system. An equiangular grid is created from -180° to 180° for the longitude and from 0° to 180° for the colatitude with equal step sizes $d\theta$ and $d\lambda$ in colatitude and longitude respectively, equal to the step sizes of the input surface load grid. The Earth is a sphere and the radial displacements are linearly interpolated, based on the Delaunay triangulation, on a 2-D grid. In case of an irregular grid, when an area on the sphere requires a higher mesh resolution, or in the case of another interpolation technique, this introduces the problem that nodes located close to one of the boundaries of the grid will not be interpolated correctly, because the grid does not know that the boundary on the left at -180° continues to the boundary on the right at 180° longitude due to the spherical shape of the Earth. Therefore, the boundaries of the grid are padded; the nodes at or closest to 180° longitude are added to the left of the -180° longitude boundary and vice versa. Figure 4.2 presents a schematic overview of the padding procedure for the 2-D interpolation for the grid at 0° latitude.

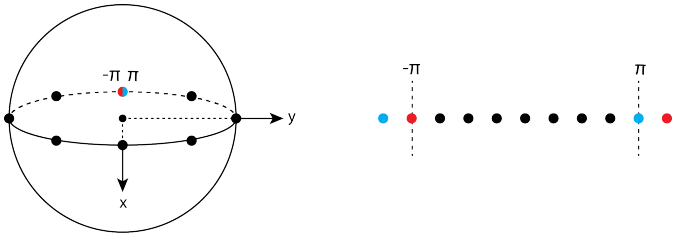

Figure 4.2: Padding of the π (blue dot) and -π (red dot) longitude at 0° latitude for interpolation of the radial displacements on a 2-D grid representing the spherical Earth. The dots represent the grid points.

The north and south pole are padded for similar reasons. The radial displacements can now be interpolated to the equiangular grid. The interpolation is performed for each time step and for each surface layer. The result is equiangular grids of nodal radial displacements for each layer surface and for each time step.

4.2. Change in moment of inertia from radial displacements

Before continuing with the determination of the perturbed gravitational potential from the radial displacements, the change in moment of inertia $\Delta\mathbf{I}$ of the model is determined from the radial displacements. The change in the moment of inertia of the model will be used for verification tests of parts of the code by comparing to an analytical solution, as later explained in Chapter 6. The change in moment of inertia is also of importance for the polar wander computations (Hu et al., 2017a; Wu and Peltier, 1984), which will be discussed in Chapter 5. From the nodal displacements follows that the model deforms with respect to the initial spherical model, and thus the moment of inertia of the body changes. The change in moment of inertia is computed for each layer k and summed up to find the change in moment of inertia of the complete model per time step. The change in moment of inertia per layer $\Delta\mathbf{I}_k(t)$ is a function of mass and its location according to:

$$
\begin{aligned}
\Delta\mathbf{I}_k(t) &= \begin{bmatrix} \Delta I_{11,k}(t) & \Delta I_{12,k}(t) & \Delta I_{13,k}(t) \\ \Delta I_{21,k}(t) & \Delta I_{22,k}(t) & \Delta I_{23,k}(t) \\ \Delta I_{31,k}(t) & \Delta I_{32,k}(t) & \Delta I_{33,k}(t) \end{bmatrix} \\
&= \begin{bmatrix} y^2+z^2 & -xy & -xz \\ -xy & x^2+z^2 & -yz \\ -xz & -yz & x^2+y^2 \end{bmatrix} \Delta M_k(t)
\end{aligned}
\tag{4.4}
$$

in which the spherical coordinates are converted to Cartesian coordinates according to:

$$\begin{aligned} x &= r\sin\theta\cos\lambda \\ y &= r\sin\theta\sin\lambda \\ z &= r\cos\theta \end{aligned} \tag{4.5}$$

As can be seen from Equation 4.4 mass changes $\Delta M_k(t)$ are required to compute the change in moment of inertia. The radial displacements need to be converted to units of mass. By multiplying the radial displacements on a layer surface k, $u_{r,k}(\theta,\lambda,t)$, with the density difference between the layer below and above the interface $\Delta\rho$, the radial displacements can be converted to surface mass densities $\sigma_k(\theta,\lambda,t)$ according to:

$$\begin{aligned} \sigma_k(\theta,\lambda,t) &= u_{r,k}(\theta,\lambda,t)\Delta\rho \\ &= u_{r,k}(\theta,\lambda,t)\left(\rho_{k+1}-\rho_k\right) \end{aligned} \tag{4.6}$$

The mass change then follows from the surface mass densities integrated over the surface of the layer, similar to Equation 3.13, according to:

$$\begin{aligned} \Delta M_k(t) &= \iint_{\Omega} \sigma_k(\theta,\lambda,t)\,d\Omega \\ &= \iint_{\Omega} u_{r,k}(\theta,\lambda,t)\left(\rho_{k+1}-\rho_k\right)d\Omega \end{aligned} \tag{4.7}$$

in which Ω is the sphere of radius R and $d\Omega$ the area of the surface element described by Equation 3.14. By combining Equations 4.5, 4.6, 4.7, and 3.14 into Equation 4.4 for the change in moment of inertia per layer surface, the full equation for the change in moment of inertia per layer surface becomes:

$$\begin{aligned} \Delta\mathbf{I}_k(t) = \left(\rho_{k+1}-\rho_k\right)R^4 \iint_{\Omega} u_{r,k}(\theta,\lambda,t)\ldots \\ \ldots \begin{bmatrix} \sin^2\theta\sin^2\lambda+\cos^2\theta & -\sin^2\theta\cos\lambda\sin\lambda & -\sin\theta\cos\lambda\cos\theta \\ -\sin^2\theta\cos\lambda\sin\lambda & \sin^2\theta\cos^2\lambda+\cos^2\theta & -\sin\theta\sin\lambda\cos\theta \\ -\sin\theta\cos\lambda\cos\theta & -\sin\theta\sin\lambda\cos\theta & \sin^2\theta\left(\cos^2\lambda+\sin^2\lambda\right) \end{bmatrix} \sin\theta\,d\theta\,d\lambda \end{aligned} \tag{4.8}$$

The change in moment of inertia for each layer k is summed up to find the change in moment of inertia of the complete model per time step, according to:

$$\begin{aligned} \Delta\mathbf{I}(t) &= \begin{bmatrix} \Delta I_{11}(t) & \Delta I_{12}(t) & \Delta I_{13}(t) \\ \Delta I_{21}(t) & \Delta I_{22}(t) & \Delta I_{23}(t) \\ \Delta I_{31}(t) & \Delta I_{32}(t) & \Delta I_{33}(t) \end{bmatrix} \\ &= \sum_{k=0}^{N_{layer}} \Delta\mathbf{I}_k(t) \end{aligned} \tag{4.9}$$

in which k indicates the layer and runs from 0 to the number of layers in the model N_{layer} minus 1. The change in moment of inertia computations of this section are performed by the `MI` function. The change in moment of inertia of the model will be used for verification tests of parts of the code by comparing to the analytical solution, as later explained in Chapter 6. Also, the change in moment of inertia is important for the polar wander computations, which will be discussed in the next Chapter 5.

4.3. Solution to the Laplace equation

As introduced in Section 2.3 the perturbed gravitational potential ϕ_1 needs to be known at the layer surfaces to have a complete set of boundary conditions and thus to be able to determine the radial displacements in the model from the stresses. By solving the Laplace equation the perturbed gravitational potential can be found. The perturbed gravitational potential $\phi_1(r,\theta,\lambda,t)$ can be decomposed into its spherical harmonic coefficients according to Equation 3.19. $\Phi_{l,m}$ are the coefficients of the spherical harmonic decomposition of $-\phi_1$. The Laplace equation, presented in Equation 2.5b, can be rewritten to (Wu, 2004; Wu and Peltier, 1982):

$$\frac{\partial^2}{\partial r^2}\Phi_{l,m} + \frac{2}{r}\frac{\partial}{\partial r}\Phi_{l,m} - \frac{l(l+1)}{r^2}\Phi_{l,m} = 0 \tag{4.10}$$

A solution to the Laplace equation is found as function of the radial displacements by using boundary conditions from Section 2.3 (Cathles, 1975), for a density structure of the Earth model described by uniform spherical shells over a uniform sphere. The assumption of uniform density within the layers is realistic because lateral density variations are small and only marginally change radial displacements. Because the radial displacement appears in the boundary condition $[\nabla\phi_1 \cdot \hat{r} + 4\pi G\rho_0 u_r]^+_- = 0$, the radial displacement is required to determine the solution to the Laplace equation. Thus, the perturbed gravitational potential will be a function of the radial displacements. The fluid core is treated as a uniform sphere with radius r_0. The mantle is made up of N shells. r_k is the outer radius of the kth shell. At the surface of the Earth $r = a$ and the solution to the Laplace equation equation is (Wu, 2004):

$$\begin{aligned}\Phi_{l,m}(a) = &\frac{4\pi G}{2l+1} a \left[\sigma_{l,m} + \rho_0(a) U_{l,m}(a)\right] \\ &+ \frac{4\pi G}{2l+1} \sum_{k=0}^{N-1} r_k U_{l,m}(r_k)(\rho_k - \rho_{k+1}) \left(\frac{r_k}{a}\right)^{l+1}\end{aligned} \tag{4.11a}$$

At the CMB the solution to the Laplace equation is (Wu, 2004):

$$\begin{aligned}\Phi_{l,m}(r_0) = &\frac{4\pi G}{2l+1} r_0 \left[\sigma_{l,m} + \rho_N(a) U_{l,m}(a)\right] \left(\frac{r_0}{a}\right)^{l-1} \\ &+ \frac{4\pi G}{2l+1} \sum_{k=0}^{N-1} r_0 U_{l,m}(r_k)(\rho_k - \rho_{k+1}) \left(\frac{r_0}{r_k}\right)^{l-1}\end{aligned} \tag{4.11b}$$

At the pth interface at radius r_p the solution to the Laplace equation is (Wu, 2004):

$$\begin{aligned}\Phi_{l,m}(r_0) = &\frac{4\pi G}{2l+1} r_p \left[\sigma_{l,m} + \rho_N(a) U_{l,m}(a)\right] \left(\frac{r_p}{a}\right)^{l-1} \\ &+ \frac{4\pi G}{2l+1} \sum_{k=p+1}^{N-1} r_p U_{l,m}(r_k)(\rho_k - \rho_{k+1}) \left(\frac{r_p}{r_k}\right)^{l-1} \\ &+ \frac{4\pi G}{2l+1} \sum_{k=0}^{p} r_k U_{l,m}(r_k)(\rho_k - \rho_{k+1}) \left(\frac{r_k}{r_p}\right)^{l+1}\end{aligned} \tag{4.11c}$$

in which $\sigma_{l,m}$ and $U_{l,m}$ are the coefficients of the spherical harmonic decomposition of the surface load and radial displacements, respectively. The surface load is the input ice load plus potentially the changing sea level. From $\Phi_{l,m}$ the spherical harmonic coefficient of degree 0 $\Phi_{0,0}$ is set to zero for mass conservation, and the spherical harmonic coefficients of degree 1, $\Phi_{1,-1}$, $\Phi_{1,0}$, and $\Phi_{1,1}$, are set to zero to remove the shift in the center of mass of the model. Then `SpherePy` is used to convert the coefficients back to the signal in the spatial domain according to Equation 3.18 to obtain $\phi_1(r_k, \theta, \lambda, t)$.

Since the nodal displacements are a function of the perturbed gravitational potential, and the perturbed gravitational potential is a function of the radial displacements, an iterative process is required to obtain a converged solution for the radial displacements, and thus for the perturbed gravitational potential. This iterative process is described in the next Section 4.4.

4.4. Iterative process

This section describes the iterative process from coupling of the FE model to the Laplace equation for a self-gravitating incompressible spherical Earth model. The perturbed gravitational potential $\phi_1(r_k, \theta, \lambda, t)$ needs to be known at the layer surfaces to have a complete set of boundary conditions and thus to be able to determine the radial displacements in the model from the stresses. By solving the Laplace equation the perturbed gravitational potential is found. However, the perturbed gravitational potential is a function of the radial displacements. The FE model and the Laplace equation are coupled through the boundary conditions for stress and displacement. Thus, an iterative process is required to solve for the radial displacements. Subsection 4.4.1 presents a schematic overview of the iterative process. The inclusion of the sea level equation is discussed in Subsection 4.4.2. Subsection 4.4.3 describes how the loads from the perturbed gravitational potential are derived, based on the boundary conditions of the model.

4.4.1. Schematic overview iterative process

Figure 4.3 presents a schematic overview of the coupling of the FE model to the Laplace equation, which supports the explanation of the iterative process.

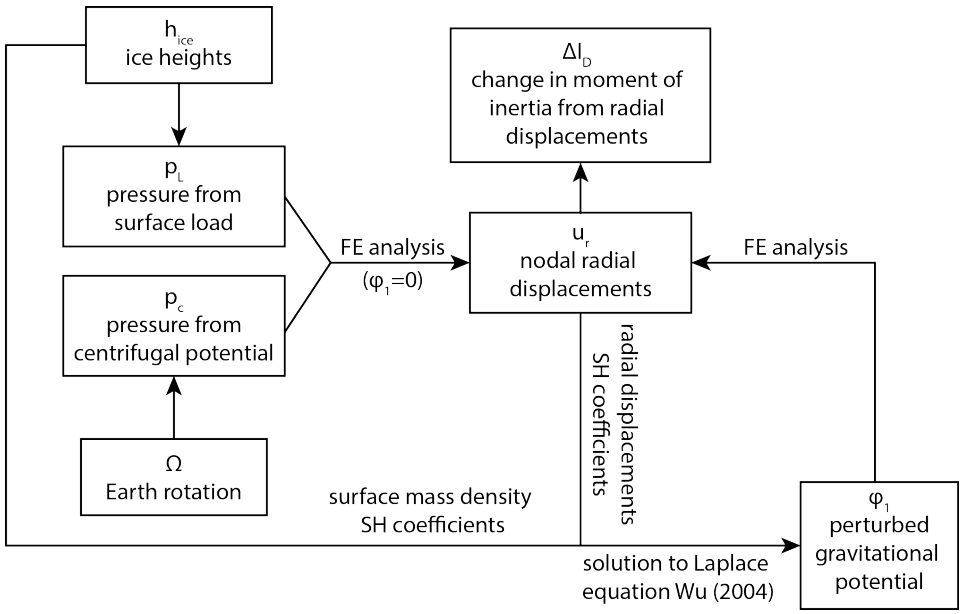

Figure 4.3: Schematic overview of the coupling of the FE model to the Laplace equation.

For the first iteration it is assumed that the perturbed gravitational potential is zero for all time steps, so $\phi_1(r_k,\theta,\lambda,t) = 0$. In the FE analysis the modified stiffness equation is solved for, presented in Equation 2.5a. The nodal displacements in the global coordinate system for all time steps follow from the stresses in the model. The nodal displacements are converted to radial displacements in the local coordinate system for nodes at the layer surfaces and interpolated to an equiangular grid. The radial displacements $u_r(r_k,\theta,\lambda,t)$ are decomposed into their spherical harmonic coefficients $U_{l,m}(r_k,t)$ per layer surface and per time step, as well as the surface load $\sigma_{l,m}(t)$ per time step. The spherical harmonic coefficients of the perturbed gravitational potential, $\Phi_{l,m}$, then follow from the solution to the Laplace equation, presented in Equation 4.11. $\Phi_{l,m}$ is converted back to the spatial domain to obtain $\phi_1(r_k,\theta,\lambda,t)$. This newly obtained $\phi_1(r_k,\theta,\lambda,t)$ gives new loads for each time step which are applied to the model, next to the still existing pressures loads from the centrifugal potential and the surface load. With new loads on the model, the FE analysis is performed again to obtain the nodal displacements. These steps are repeated until the solution is converged (Wu, 2004).

4.4.2. Inclusion of the sea level equation

Due to the fact that the Earth is self-gravitating, the displacements perturb the gravitational potential field, and thus the geoid is affected. Sea level is measured as a change in the geoid with respect to the Earth's solid surface, and thus the sea level is affected by the displacements and gravitational potential. When the sea level change is included, the radial displacements and the perturbed gravitational potential at the model surface give the new sea level through (Mitrovica and Peltier, 1991):

$$S(\theta,\lambda,t) = \left[\frac{\phi_{1,s}(\theta,\lambda,t)}{g_{acc,s}} - u_{r,s}(\theta,\lambda,t) + \left(-\frac{M_{ice}(t)}{\rho_{water}A_0} - \frac{1}{A_0}\left\langle \frac{\phi_{1,s}(\theta,\lambda,t)}{g_{acc,s}} - u_{r,s}(\theta,\lambda,t)\right\rangle_0\right)\right] O(\theta,\lambda) \tag{4.12}$$

in which $g_{acc,s}$ is gravitational acceleration at the surface, $u_{r,s}(\theta,\lambda,t)$ the radial displacements at the surface, $\phi_{1,s}(\theta,\lambda,t)$ the perturbed gravitational potential at the surface, A_0 the area of the ocean basins, and $\langle\rangle_0$ is the integration over the ocean basins. In this sea level equation the effect of the Earth's rotation is excluded. The updated sea level and the input ice load form the new load at the surface. Thus, these new loads need to overwrite the initial loads defined in `Model_gen.py`. The surface mass density $\sigma_{l,m}$ will be updated as well from the new surface load. Including the sea level equation in the numerical model can be done using the method described here. However, for this research the sea level equation has not been investigated in conjunction with true polar wander, and thus will be left out of the schematic overviews.

4.4.3. Pressure from perturbed gravitational potential

The perturbed gravitational potential $\phi_1(r_k, \theta, \lambda, t)$ is applied for each layer and each time step according to the boundary conditions. In `Abaqus` an expression field is created relative to the local coordinate system based on $\phi_1(r_k, \theta, \lambda, t)$. The perturbed gravitational potential is then applied as a pressure load at each of the layers. For a liquid core the pressure from ϕ_1 at the CMB, $p_{\phi,0}$, is applied to the inner surface of the layer above the core Sin_1, derived from the boundary condition in Equation 2.10, according to (Wu, 2004):

$$p_{\phi,0} = (-1)^{flag\_lc+1} \phi_1 \left(\rho_0 - \rho_1\right) \tag{4.13}$$

The pressure from ϕ_1 at the solid-solid interfaces i, $p_{\phi,i}$, are derived from the boundary condition in Equation 2.8, according to (Wu, 2004):

$$p_{\phi,i} = \phi_1 \left(\rho_{i+1} - \rho_i\right) \tag{4.14}$$

The pressure from ϕ_1 at the surface, $p_{\phi,s}$, is derived from the boundary condition in Equation 2.6, according to (Wu, 2004):

$$p_{\phi,s} = -\phi_1 \rho_s \tag{4.15}$$

Now that the loads are defined from the perturbed gravitational potential, the FE analysis can be performed again. The numerical model will be extended with true polar wander, as described in Chapter 5.

4.5. Python scripts information

Here an overview is given of the already existing `Python` scripts used in this research. The information is in the form of 'Author: Purpose'. The first line gives information on the initial creator and purpose of the script, and the following lines of the additional contributions. This overview does not include the contributions made in this research.

`Model_data.py`
Haiyang Hu: Definition of constants and model data required to build the model.
Bas Blank: Added the ice-equivalent sea level change.

`Model_gen.py`
Haiyang Hu: A multi-layer model generator for Abaqus-CAE. The centrifugal potential for a static rotational axis is included.
Bas Blank: Added the ice and sea load. Added a subroutine to remove the spherical harmonic degree 0 and 1.

`Iter.py`
Haiyang Hu: A multi-layer model iterator for Abaqus-CAE, applied after the model is generated.
Bas Blank: Added the sea level equation and ice and sea load.

`sph_tools_TPW.py`
Haiyang Hu: A subroutine for the perturbed gravitational potential as function of radial displacements.
Bas Blank: Replaced the `scipy.Special.lpmv` with the `SpherePy` package for determination of spherical harmonic coefficients to be able to include higher degrees. Changed the `block_gen` function to interpolate the radial displacements of the mesh from the centers to the corner points of the grid cells.

5

Implementation of true polar wander

The process of TPW is explained in Chapter 1. Here first the mathematical expressions for polar wander are presented from Wu and Peltier (1984) and second how polar wander is implemented in the numerical model, based on a proposed approach from Hu et al. (2017a). The two governing equations for true polar wander are the Liouville equation and the moment of inertia equation. The Liouville equation describes the change in rotational state needed to conserve angular momentum for a change in moment of inertia, and is presented in Section 5.1. The moment of inertia equation describes the change in moment of inertia for a change in rotational state. The moment of inertia equation is a function of tidal and load Love numbers of the body. The Love number theory is discussed in Section 5.2 based on Peltier (1976), and the moment of inertia equation in Section 5.3. Section 5.4 justifies the linearization of the Liouville equation (Hu et al., 2017a; Wu and Peltier, 1984), and how true polar wander follows from perturbations in the moment of inertia. The implementation of true polar wander in the numerical presented in Section 5.5 is the new contribution to the numerical model. The implementation is based on a proposed approach from Hu et al. (2017a) but has not been implemented and tested before. The implementation process is described in detail and a schematic overview of the complete code is presented.

5.1. Liouville equation

A torque-free situation is assumed since the Earth's system is not subjected to any significant external torque. Thus, the angular momentum is conserved. The Euler equation of motion describes the change in rotational state $\boldsymbol{\omega}$ required to satisfy the conservation in angular momentum, where $\mathbf{I}$ is the moment of inertia (MoI) tensor of the body. The rotational state in the body-fixed frame is defined here as $\boldsymbol{\omega} = (\omega_1,\omega_2,\omega_3)$. The Euler rotation equation is as follows:

$$\frac{d}{dt}(\mathbf{I}\cdot\boldsymbol{\omega}) + \boldsymbol{\omega}\times\mathbf{I}\cdot\boldsymbol{\omega} = 0 \tag{5.1}$$

The Euler rotation equation presented above assumes a constant MoI tensor. However, the Earth is deformable and thus the MoI tensor of the body $\mathbf{I}$ is dependent on time and becomes $\mathbf{I}(t)$. The Euler rotation equation with a time-dependent MoI tensor is known as the Liouville equation (Munk and MacDonald, 1960):

$$\frac{d}{dt}(\mathbf{I}(t)\cdot\boldsymbol{\omega}) + \boldsymbol{\omega}\times\mathbf{I}(t)\cdot\boldsymbol{\omega} = 0 \tag{5.2}$$

The time-dependent MoI tensor $\mathbf{I}(t)$ can change due to three different contributors which are related to the deformable nature of Earth (Gold, 1955; Hu, 2018):

1. The direct contribution from a relocation of mass of the body. The mass anomaly causes a change in centrifugal force such that the body will reorient to a new equilibrium position. The MoI tensor of the mass anomaly is referred to as $\Delta\mathbf{I}_1$.
2. The indirect contribution from a relocation of mass of the body causing a deformation of the body. The body will deform under the mass anomaly until a new hydrostatic equilibrium is reached. The change in MoI tensor due to the deformation of the body due to the mass anomaly is referred to as $\Delta\mathbf{I}_2$.

3. The indirect contribution from the equatorial bulge readjustment. The centrifugal force applied to the body at its new position from the load and deformation due to the mass anomaly causes the equatorial bulge to readjust perpendicular to the rotation axis again. The change in MoI tensor due to the equatorial bulge readjustment is referred to as $\Delta\mathbf{I}_3$.

5.2. Tidal and load Love numbers

Tidal Love numbers describe the deformational response of the Earth to tidal forcing, whereas load Love numbers describe the deformational response of the Earth to loading on the Earth's surface. For a homogeneous stratified viscoelastic Earth the deformation can be determined by Love numbers which can directly be obtained by the normal mode method (Peltier, 1976). The degree 2 load Love number and tidal Love number in the time domain are presented in equation 5.3 and 5.4, respectively.

$$k_2^L(t) = k_2^{L,E}\delta(t) + \sum_{i=1}^{M} k_i^L e^{s_i t} \tag{5.3}$$

$$k_2^T(t) = k_2^{T,E}\delta(t) + \sum_{i=1}^{M} k_i^T e^{s_i t} \tag{5.4}$$

in which the superscript E stands for the elastic Love number component, $\delta(t)$ for the Dirac-delta function, M for the number of modes, k_i for the viscous Love number component per mode, and s_i for the negative inverse relaxation time per mode. Equation 5.5 and 5.6 present the degree 2 load Love number and tidal Love number in the Laplace domain (Peltier, 1974):

$$k_2^L(s) = k_2^{L,E} + \sum_{i=1}^{M} \frac{k_i^L}{s - s_i} \tag{5.5}$$

$$k_2^T(s) = k_2^{T,E} + \sum_{i=1}^{M} \frac{k_i^T}{s - s_i} \tag{5.6}$$

in which s is the complex variable of frequency. It is important to note that literature may show $s+s_i$ in the denominator of equation 5.5 and 5.6, and $-s_i t$ in the exponent of equation 5.3 and 5.4. Some literature adopts the positive inverse relaxation time for s_i, whereas here the inverse relaxation time is defined as negative. Earth's viscosity plays a major role in its rotational behavior through k_i and s_i.

5.3. Moment of inertia equation

The time-dependent MoI tensor is a summation of the MoI of the unperturbed body I_0 and the contributions in change of MoI from the mass anomaly and equatorial bulge readjustment $\Delta I_{1,ij}$, $\Delta I_{2,ij}$, and $\Delta I_{3,ij}$ where $\Delta I_{x,ij}$ are the components of the tensor $\Delta\mathbf{I}_x$ and δ_{ij} is the Kronecker delta function (Sabadini et al., 2016):

$$\begin{aligned} I_{ij}(t) &= I_0\delta_{ij} + \Delta I_{ij}(t) \\ &= I_0\delta_{ij} + \Delta I_{1,ij}(t) + \Delta I_{2,ij}(t) + \Delta I_{3,ij}(t) \end{aligned} \tag{5.7}$$

The MoI tensor of the mass anomaly $\Delta\mathbf{I}_1(t)$ is directly related to the MoI of the mass anomaly $\mathbf{C}(t)$, where the operator $*$ denotes linear convolution (Munk and MacDonald, 1960):

$$\Delta I_{1,ij}(t) = \delta(t) * C_{ij}(t) \tag{5.8}$$

The change in MoI tensor due to the deformation of the body due to the mass anomaly $\Delta\mathbf{I}_2$ is a function of the applied load and load Love numbers k^L (Farrell, 1972; Munk and MacDonald, 1960):

$$\Delta I_{2,ij}(t) = k^L(t) * C_{ij}(t) \tag{5.9}$$

Using MacCullagh's formula the change in MoI tensor due to the equatorial bulge readjustment $\Delta\mathbf{I}_3$ is related to the tidal Love number of degree 2 k_2^T (Munk and MacDonald, 1960; Sabadini et al., 2016):

$$\Delta I_{3,ij}(t) = \frac{k_2^T(t)\,a^5}{3G} * \left(\Omega(t)^2\left[\omega_i(t)\omega_j(t) - \frac{1}{3}\delta_{ij}\right]\right) \tag{5.10}$$

in which a is Earth's radius, G the gravitational constant, ω the components of the change in rotational vector $\boldsymbol{\omega} = \Omega(\omega_1,\omega_2,\omega_3)^T$, and Ω the rotational speed of the body. The Correspondence Principle is used in the derivation of the contributions to the change in MoI, of which the resulting equations are presented above. An elastic problem in the Laplace domain is converted to a linear viscoelastic problem in the time domain (Peltier, 1974). By combining Equations 5.7 to 5.10 the complete moment of inertia equation becomes:

$$I_{ij}(t) = I_0\delta_{ij} + \left[\delta(t) + k^L(t)\right] * C_{ij}(t) + \frac{k_2^T(t)a^5}{3G} * \left(\Omega(t)^2\left[\omega_i(t)\omega_j(t) - \frac{1}{3}\delta_{ij}\right]\right) \tag{5.11}$$

With the moment of inertia equation the total change in MoI of the rotating body can be obtained as a function of the MoI of the mass anomaly $\mathbf{C}(t)$, the rotational state $\boldsymbol{\omega}$, and the tidal and load Love numbers of the body k^T and k^L respectively. The required change in rotational state to satisfy conservation of angular momentum can then be obtained from the change in MoI using the Liouville equation, presented in Equation 5.2. This process continues until the body reaches a new stable hydrostatic equilibrium.

5.4. Linearized Liouville equation

The Liouville equation, presented in Section 5.1 is highly non-linear. Three different methods exist to solve for the system of equations:

1. Linear method (Nakiboglu and Lambeck, 1980; Sabadini and Peltier, 1981; Wu and Peltier, 1984):
   The linear method is suitable when the instantaneous position of the rotation pole does not depart considerably from a reference equilibrium rotation pole position, thus for small angle TPW.
2. Non-linear method (Ricard et al., 1993; Sabadini et al., 1982; Spada et al., 1992):
   The non-linear method is suitable for large angle TPW. A difficulty in the non-linear method is the convolution for the tidal Love number, describing the viscous behavior of the equatorial bulge (Hu, 2018). By assuming that the studied time scale of rotation is much longer than the dominant relaxation time of the body, the quasi-fluid limit is adopted (Ricard et al., 1993). This approximation does not fully represent the response of a Maxwell body due to underestimation of the equatorial bulge readjustment speed.
3. Fluid limit method (Hu, 2018; Matsuyama et al., 2014; Willemann, 1984):
   The fluid limit method takes into account the MoI of a tidal bulge and the reorientation of the body concerning both the tidal and rotational axis. This method does provide the reorientation path for a time-invariant load but the accuracy is unclear for a time-varying load.

Which of these methods is more suitable and accurate depends on the planetary body. The tidal force can be ignored when describing the rotational behavior of the Earth since the tidal force is much smaller than the centrifugal force. This is because the rotational period of the Earth is much smaller than its orbital period and because the Moon only has a small effect. Furthermore, the observed TPW on Earth is in the order of 1°/Myr, obtained from the International Earth Rotation and Reference Systems Service (IERS) (Dickmann, 1977), which is small angle TPW. Thus, the linear method is sufficiently accurate for TPW induced by GIA on the Earth. Therefore, only the linear method will be further discussed. However, in Section 5.5, on the implementation of TPW in the numerical model, will be discussed that by using coordinate transformations the linearized Liouville equation is also valid for large angle TPW.

5.4.1. Hydrostatic equilibrium of the rotating Earth

The MoI of the viscoelastic body in hydrostatic equilibrium needs to be determined, when the centrifugal force and self-gravitational force are in balance. The relation between the equatorial bulge and the change in MoI is described by equation 5.10. At time t is zero a non-rotating spherical body is assumed. When the body starts to rotate with a constant speed, the body will flatten due to its viscoelastic properties under the centrifugal force. At infinite time, the viscoelastic body will have reached its hydrostatic equilibrium when no other forces are considered. The rotational vector is set to $\boldsymbol{\omega}(t) = \Omega(\omega_1,\omega_2,\omega_3)^T = \Omega(0,0,1)^T$, where Ω is the rotational speed around the z-axis in the local frame. The difference in MoI between the non-rotating spherical body and the rotating body in hydrostatic equilibrium $\Delta\mathbf{I}_h$ is determined by taking the infinite time limit of equation 5.10 (Hu, 2018):

$$\Delta\mathbf{I}_h = \lim_{t\to\infty} \Delta\mathbf{I}_3(t) \tag{5.12}$$

Using the final value theorem equation 5.12 can be solved according to:

$$\lim_{t\to\infty} \Delta\mathbf{I}_3(t) = \lim_{s\to 0} s\Delta\mathbf{I}_3(s) \tag{5.13}$$

in which s is the complex variable of frequency and $\Delta\mathbf{I}_3(s)$ the Laplace transform of $\Delta\mathbf{I}_3(t)$ as described by:

$$\begin{aligned}\Delta\mathbf{I}_3(s) &= \int_0^\infty \frac{k_2^T(t)a^5}{3G}\left(\Omega(t)^2\left[\omega_i(t)\omega_j(t) - \frac{1}{3}\delta_{ij}\right]\right)e^{-st}dt \\ &= \frac{1}{s}\frac{k_2^T(s)a^5}{3G}\left(\Omega(t)^2\left[\omega_i(t)\omega_j(t) - \frac{1}{3}\delta_{ij}\right]\right)\end{aligned} \tag{5.14}$$

in which G is the gravitational constant, a Earth's radius, Ω the rotational speed of the body, and k_2^T the degree 2 tidal Love number of the body. $\Delta\mathbf{I}_3(s)$ can be substituted back into equation 5.13 and 5.12 to find the difference in MoI between the non-rotating spherical body and the rotating body in hydrostatic equilibrium $\Delta\mathbf{I}_h$, together with $\boldsymbol{\omega}(t) = \Omega(0,0,1)^T$:

$$\begin{aligned}\Delta\mathbf{I}_h &= \lim_{s\to 0} s\frac{1}{s}\frac{k_2^T(s)a^5}{3G}\left(\Omega(s)^2\left[\omega_i(s)\omega_j(s) - \frac{1}{3}\delta_{ij}\right]\right) \\ &= \begin{pmatrix}\Delta A & 0 & 0\\ 0 & \Delta B & 0\\ 0 & 0 & \Delta C\end{pmatrix} = \frac{k_f^T a^5\Omega^2}{3G}\begin{pmatrix}-\frac{1}{3} & 0 & 0\\ 0 & -\frac{1}{3} & 0\\ 0 & 0 & \frac{2}{3}\end{pmatrix}\end{aligned} \tag{5.15}$$

in which ΔA, ΔB, and ΔC are the changes of MoI at the three principal axes, between the non-rotating spherical body and the rotating viscoelastic body in hydrostatic equilibrium, and k_f^T is the fluid Love number. The fluid Love number is measure for the background oblateness, and is defined as the fluid limit of the degree 2 tidal Love number, thus for s equals zero (Munk and MacDonald, 1960):

$$k_f^T = k_2^T(s=0) = k_2^{T,E} - \sum_{i=1}^{M}\frac{k_i^T}{s_i} \tag{5.16}$$

The total MoI of the body around the three principal axes A, B, and C, can then be obtained by adding the MoI of the unperturbed body I_0. When the body is assumed to be symmetric, thus when there are no lateral variations present, The total MoI of the body around the three principal axes becomes (Munk and MacDonald, 1960; Wu and Peltier, 1984):

$$\begin{aligned}A &= I_0 + \Delta A = I_0 + \Delta B = B\\ C &= I_0 + \Delta C\end{aligned} \tag{5.17}$$

in which A is the polar moment of inertia and C the equatorial moment of inertia for a purely hydrostatic, unperturbed, state of the rotating Earth. The difference between C and A is the size of the equatorial bulge (Munk and MacDonald, 1960):

$$C - A = \frac{2}{3}\frac{k_f^T a^5\Omega^2}{3G} - -\frac{1}{3}\frac{k_f^T a^5\Omega^2}{3G} = \frac{k_f^T a^5\Omega^2}{3G} \tag{5.18}$$

5.4.2. True polar wander equations

The moment of inertia of the Earth $\mathbf{I}$ can now be described as the combination of the MoI of the purely hydrostatic state of the Earth following from A, B, and C, and perturbations to the MoI (Munk and MacDonald, 1960; Wu and Peltier, 1984):

$$\mathbf{I} = \begin{pmatrix}A + \Delta I_{11} & \Delta I_{12} & \Delta I_{13}\\ \Delta I_{21} & B + \Delta I_{22} & \Delta I_{23}\\ \Delta I_{31} & \Delta I_{32} & C + \Delta I_{33}\end{pmatrix} \tag{5.19}$$

in which ΔI_{ij} are perturbations in MoI from the contributions in change of MoI from the mass anomaly and equatorial bulge readjustment as described by Equations 5.8, 5.9, and 5.10 presented in Section 5.3. The goal is to find expressions for the perturbed rotational vector as function of the change in moment of inertia dependent on mass redistribution. The perturbed rotational vector can be described in dimensionless quantities m_i as defined in (Munk and MacDonald, 1960; Wu and Peltier, 1984):

$$\boldsymbol{\omega} = \Omega\,(\omega_1, \omega_2, \omega_3)^T = \Omega\,(m_1, m_2, 1 + m_3)^T \tag{5.20}$$

Ω is the initial rotational speed of the body. m_1 and m_2 give the polar shift in radians. m_1 is in the x-direction, in the equatorial plane from the Earth's center of mass towards the Greenwich meridian. m_2 is in the y-direction, in the equatorial plane from the the Earth's center of mass towards 90° East longitude. m_3 gives the change in the length of day in radians per sidereal day (Sabadini et al., 2016). Note that ΔI_{ij} and m_i have to be small fluctuations away from the base state such that small angle TPW is preserved and the linearized Liouville equation represents reality sufficiently well (Wu and Peltier, 1984). Thus, $m_i \ll 1$ and $\Delta I_{ij} \ll A, B, C$. $\mathbf{I}$ and $\boldsymbol{\omega}$ from Equation 5.19 and 5.20 respectively can now be substituted into the Liouville equation 5.2. When the second and higher order terms in the smaller fluctuations are dropped then the Liouville equation decouples into (Sabadini et al., 2016):

$$\dot{m}_1 = -\frac{C-B}{A}\Omega m_2 + \frac{\Omega}{A}\Delta I_{23} - \frac{\Delta \dot{I}_{13}}{A} \tag{5.21a}$$

$$\dot{m}_2 = \frac{C-A}{B}\Omega m_1 - \frac{\Omega}{B}\Delta I_{13} - \frac{\Delta \dot{I}_{23}}{B} \tag{5.21b}$$

$$\dot{m}_3 = -\frac{\Delta I_{33}}{C} \tag{5.21c}$$

In the presence of lateral variations in the model, i.e. $A \neq B$, the Eulerian free precession frequency cannot be used to further combine these equations. As will be further explained in Section 5.5, numerically true polar wander is calculated stepwise. In each step of the numerical integration it is assumed that the step is small enough to be able to treat the change in the inertia tensor as linear (Hu et al., 2017a). By using the assumption of linearity for the change in the inertia tensor, and by ignoring periodical terms which represent the Chandler wobble, the expressions for the perturbed rotational vector as function of the change in moment of inertia become after some manipulation (Hu et al., 2017a; Sabadini et al., 2016):

$$m_1 = \frac{\Delta I_{13}(t)}{C-A} + \frac{C\Delta \dot{I}_{23}(t)}{\Omega\,(C-A)\,(C-B)} \tag{5.22a}$$

$$m_2 = \frac{\Delta I_{23}(t)}{C-B} + \frac{C\Delta \dot{I}_{13}(t)}{\Omega\,(C-A)\,(C-B)} \tag{5.22b}$$

$$m_3 = -\frac{\Delta I_{33}(t)}{C} \tag{5.22c}$$

The parts which contain the derivatives of the changes in the inertia tensor, the second terms of the above m_1 and m_2 equations, are small for the Earth and can be ignored. These terms are only of importance for slowly rotating bodies. When the magnitude of the second terms become comparable to the magnitude of the first terms in Equation 5.22 for m_1 and m_2 a mega wobble occurs (Hu et al., 2017a; Sabadini et al., 2016; Spada et al., 1996). For the Earth Equation 5.22 thus reduces to:

$$m_1 = \frac{\Delta I_{13}(t)}{C-A} \tag{5.23a}$$

$$m_2 = \frac{\Delta I_{23}(t)}{C-B} \tag{5.23b}$$

$$m_3 = -\frac{\Delta I_{33}(t)}{C} \tag{5.23c}$$

Now that the analytical expressions are at hand to determine true polar wander from the changes in the inertia tensor of the body, the implementation of true polar wander in the numerical model can be discussed in the next section.

5.5. Implementation in numerical model

This section presents the implementation of true polar wander in the numerical model. Subsection 5.5.1 discusses the implementation of a flattened Earth model in hydrostatic equilibrium for the rotating Earth from the spherical non-rotating Earth model. Subsection 5.5.2 presents the implementation of true polar wander once the model is in hydrostatic equilibrium, based on an algorithm using coordinate transformations such that the local angular change in each step remains small, but allows for large angle polar wander. This section also describes how the computed polar wander feeds back into the numerical model by changing the local coordinate system to which the centrifugal potential is applied for each time step.

5.5.1. Model in hydrostatic equilibrium

In `Abaqus` the Earth model starts out as a spherical model. To be able to study TPW of bodies in their hydrostatic equilibrium state, first the pressure from the centrifugal potential, as described in Section 3.2, needs to be applied for a sufficiently long time for the body to reach this hydrostatic equilibrium state. The time needed for a model to reach hydrostatic equilibrium depends on the layer properties and thus differs per model. The time needed will be investigated in Chapter 6, where it will also be shown that there is no need for intermediate time steps building up to this time in `Abaqus` for accurate change in moment of inertia values. Only after the model is in hydrostatic equilibrium, surface loads can be applied which trigger TPW. At the end of the first time step, the output from the FE analysis will be the displacements at the nodes. As explained in Section 4.2 the displacements are converted to the change in moment of inertia. Only the elements ΔI_{11}, ΔI_{22}, and ΔI_{33} should have a value, representing the change in moment of inertia around the x-, y- z- axis in the local coordinate system, respectively. For the first time step these are equal to ΔA, ΔB, and ΔC. Figure 5.1 presents an exaggerated drawing of the shapes of the spherical non-rotating Earth model and the flattened rotating Earth model in hydrostatic equilibrium.

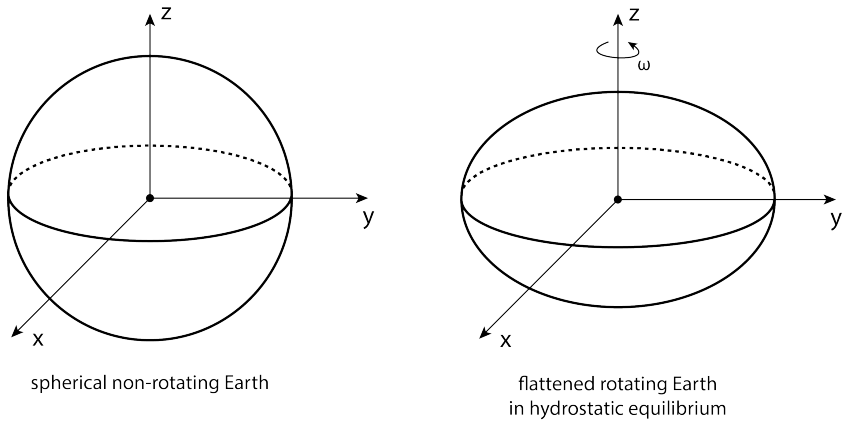

Figure 5.1: Exaggerated drawing of the shapes of the spherical non-rotating Earth model and the flattened rotating Earth model in hydrostatic equilibrium.

Due to the flattening of the Earth more mass is relocated closer the x-y plane and further away from the z-axis. This means that with respect to the spherical non-rotating Earth model over the first time step of the simulation, the change in moment of inertia elements ΔI_{11} and ΔI_{22} will decrease, thus become negative, and ΔI_{33} will increase, thus becomes positive. After the first time step to get to a flattened rotating Earth model in hydrostatic equilibrium, the algorithm for true polar wander induced by input ice loads can be implemented.

5.5.2. Algorithm for implementing true polar wander

The expressions for the perturbations in the rotational vector m_i from Equation 5.23 are based on the linearized Liouville equation. The Liouville equation is linearized at the position where the z-axis of the coordinate system is the rotational axis and where the equatorial bulge is perpendicular to the rotational axis (Hu et al., 2017a; Wu and Peltier, 1984). From this linearization follows that the instantaneous position of the rotational axis may not depart considerably from a reference equilibrium rotational axis position. Thus, the linearized Liouville equation is only suitable for small perturbations from a reference state, i.e. for small angle TPW. Using the algorithm presented here, the polar wander expressions derived from the linearized Liouville equation can also be used for large angle TPW.

Hu et al. (2017a) describe that a new reference frame can be defined in which the new z-axis coincides with the current rotational axis, by assuming that during the process of TPW the equatorial bulge readjustment is fast enough, or the polar wander slow enough, such that the equatorial bulge is always nearly perpendicular to the rotational axis. The Liouville equation can then be linearized in the new reference frame. During TPW the rotational axis is moving towards the axis of maximum moment of inertia, which moves further away due to the displacement of the mass anomaly and the viscoelastic relaxation of the body. It is assumed that the angle between these two axes is small enough such that the Liouville equation can be linearized. Cambiotti et al. (2011) developed a linear scheme of the Liouville equation in the system of the principal moments of inertia reference frame of the mass anomaly, and studied the validity of the assumption for a non-linear approach for TPW induced by mantle convection. The assumption can only be violated when the inertia tensor of the mass anomaly triggering TPW is of comparable magnitude as the inertia tensor of the rotating body. The linearized Liouville equation can then not be used because the angle between the axis of maximum moment of inertia, from the rotating body plus the mass anomaly, and the rotational axis is not small. This is not the case for GIA-induced TPW on the Earth. The TPW algorithm, based on this assumption, which is used in the numerical model will be presented here.

As previously defined in Equation 5.20 the vector of rotation is $\boldsymbol{\omega} = \Omega\,(\omega_1, \omega_2, \omega_3)^T = \Omega\,(m_1, m_2, 1+m_3)^T$. $(\omega_1, \omega_2, \omega_3)$ and $(m_1, m_2, 1+m_3)$ are unit vectors. Figure 5.2 presents a schematic overview of the process of true polar wander induced by a constant surface load, instantly applied at t_1 and the different reference frames. At t_0 the local frame is defined with respect to the global reference frame in `Abaqus` as presented in Figure 3.4. This local reference frame at t_0 is called the initial local frame. At t_1 the rotating Earth is flattened and its rotational axis coincides with the z-axis of the initial local frame. At t_1 a surface load is applied to the model which triggers TPW. Both the elastic and viscous response will be included at t_2. When the time step between t_1 and t_2 is very short, in the order of one year, then the elastic response of the model at t_2 is dominant over the viscous response. The TPW at t_2 can then be seen as the elastic response of the body to the surface load. The TPW that starts at t_1 has to be calculated in the frame whose z-axis coincides with $\boldsymbol{\omega}$. Since the rotational axis at t_1 coincides with the initial local frame, no coordinate transformation needs to take place. However, to determine TPW that starts at t_2 a coordinate transformation needs to take place from the z-axis in the initial local frame to the z-axis which coincides with the rotational axis at t_2.

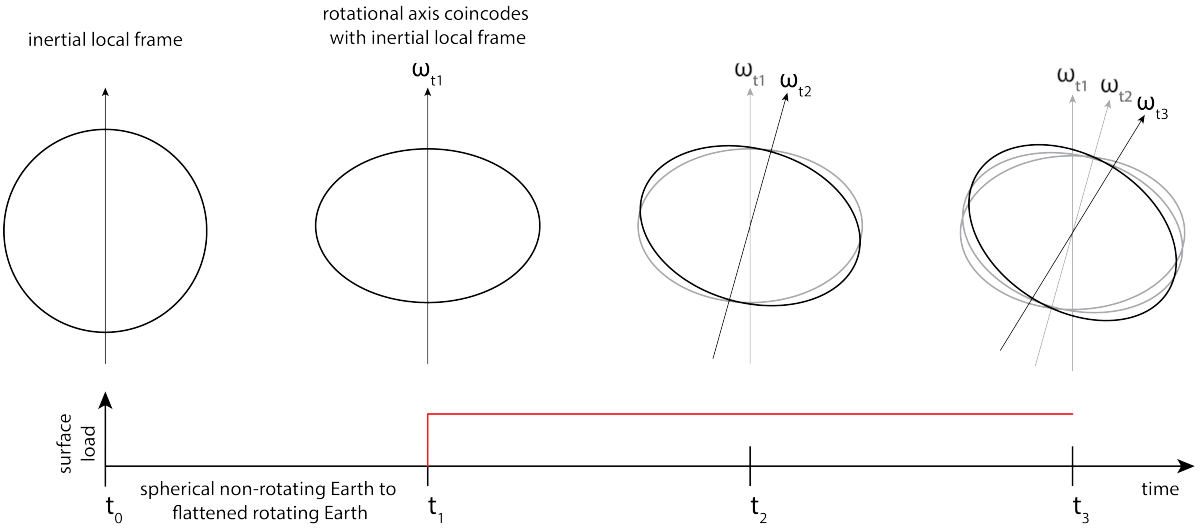

Figure 5.2: Schematic overview of the process of true polar wander induced by a surface load and the different reference frames.

Thus, for an arbitrary $\boldsymbol{\omega}$ the TPW that starts from this vector has to be calculated in the frame whose z-axis coincides with $\boldsymbol{\omega}$ at that time (Hu et al., 2017a). The coordinate transformation matrix from $\Omega\,(0,0,1)^T$ to $\Omega\,(\omega_1, \omega_2, \omega_3)^T$ is (Arvo, 1992; Hu et al., 2017a):

$$\mathbf{Q} = \begin{bmatrix} \omega_3 + \frac{\omega_2^2}{1+\omega_3} & -\frac{\omega_1\omega_2}{1+\omega_3} & \omega_1 \\ -\frac{\omega_1\omega_2}{1+\omega_3} & 1 - \frac{\omega_2^2}{1+\omega_3} & \omega_2 \\ -\omega_1 & -\omega_2 & \omega_3 \end{bmatrix} \tag{5.24}$$

The algorithm for large angle TPW triggered by a mass anomaly on a viscoelastic rotating body is as follows (Hu et al., 2017a):

1. Assume that step $i+1$ starts at t_i with the rotational vector $\boldsymbol{\omega}^i = \Omega^i\left(\omega_1^i, \omega_2^i, \omega_3^i\right)$ and ends at t_{i+1} with the rotational vector $\boldsymbol{\omega}^{i+1} = \Omega^{i+1}\left(\omega_1^{i+1}, \omega_2^{i+1}, \omega_3^{i+1}\right)$. For the first iteration is assumed that the vector of rotation does not change, thus that $\boldsymbol{\omega}^{i+1} = \boldsymbol{\omega}^i = \Omega^0(0,0,1)$, with Ω^0 the initial angular rotational rate.

2. The changes in moment of inertia $\Delta\mathbf{I}_D$ due to deformation of the body follow from the FE analysis. The deformations are caused by the pressure from the centrifugal potential $\Delta\mathbf{I}_{D,c}$ and from the surface load $\Delta\mathbf{I}_{D,L}$. The total change in moment of inertia $\Delta\mathbf{I}$ also needs to include the moment of inertia of the mass anomaly $\Delta\mathbf{I}_L$. The total change in moment of inertia thus becomes:

$$\Delta\mathbf{I} = \Delta\mathbf{I}_D + \Delta\mathbf{I}_L = \Delta\mathbf{I}_{D,c} + \Delta\mathbf{I}_{D,L} + \Delta\mathbf{I}_L \tag{5.25}$$

   The inertia tensor $\Delta\mathbf{I}$ needs to be converted to the local coordinate system $\Delta\mathbf{I}_{local}$ in which the z-axis aligns with the rotational vector, using the coordinate transformation matrix $\mathbf{Q}$, according to:

$$\begin{aligned} \Delta\mathbf{I}_{local} &= \mathbf{Q}^T\Delta\mathbf{I}\mathbf{Q} \\ &= \mathbf{Q}^T\left(\Delta\mathbf{I}_D + \Delta\mathbf{I}_L\right)\mathbf{Q} \\ &= \mathbf{Q}^T\Delta\mathbf{I}_D\mathbf{Q} + \mathbf{Q}^T\Delta\mathbf{I}_L\mathbf{Q} \\ &= \Delta\mathbf{I}_{D,local} + \Delta\mathbf{I}_{L,local} \end{aligned} \tag{5.26}$$

   The transformation is performed for the changes in moment of inertia from the deformation of the body and the direct contribution from the mass anomaly, or surface load, separately. The reason for this will become clear in the next step of the algorithm.

3. The elements from total change in moment of inertia in the local frame $\Delta\mathbf{I}_{local}$ are used as input in Equation 5.23 to compute the perturbations to the rotational vector in the local frame m_1, m_2, and m_3. Note that the changes in moment of inertia around the principles axes in the local frame, ΔA, ΔB, and ΔC can be extracted from the diagonal of $\Delta\mathbf{I}_{D,local}$. Thus changes in moment of inertia around the principal axes, ΔA, ΔB, and ΔC are updated through $\Delta\mathbf{I}_{D,local}$, for each time step. For the computation of m_1 and m_2 the unperturbed moment of inertia of the body I_0 cancels out, but for the computation of m_3 I_0 needs to be defined, either analytically or from observations depending on the application. From the rotational vector perturbations the rotational vector at the end of the time step in the local frame of $\boldsymbol{\omega}^i$ can be determined as $\boldsymbol{\omega}' = \Omega^i(m_1, m_2, 1+m_3)$.

4. The length-of-day (LOD) and thus the rotational rate of the body also changes. LOD^{i+1} can be determined by taking the norm of the elements of $\boldsymbol{\omega}'$, thus of $\boldsymbol{\omega}'/\Omega^i$. LOD^i can be determined by taking the norm of the elements of $\boldsymbol{\omega}^i$, thus of thus of $\boldsymbol{\omega}^i/\Omega^i$. The new rotational rate Ω^{i+1} is then determined according to:

$$\Omega^{i+1} = \frac{LOD^i}{LOD^{i+1}}\Omega^i \tag{5.27}$$

   The rotational vector at the end of the time step in the local frame of $\boldsymbol{\omega}^i$ can then be described as:

$$\begin{aligned} \boldsymbol{\omega}'' &= \Omega^{i+1}(m_1, m_2, 1+m_3) \\ &= \frac{\Omega^{i+1}}{\Omega^i}\Omega^i(m_1, m_2, 1+m_3) \\ &= \frac{\Omega^{i+1}}{\Omega^i}\boldsymbol{\omega}' \end{aligned} \tag{5.28}$$

It is found that this is an important step. The change in the rotational rate from the change in length-of-day (LOD), which is determined from the norm of the perturbed rotational vector elements in the local frame, is a crucial step for the TPW solution to converge in terms of number of iterations for the radial displacement solution in the FE analysis. The new rotational vector needs to be normalized using the new rotational rate.

5. The rotational vector at the end of the time step in the local frame $\boldsymbol{\omega}''$ then needs to be transformed back to the initial local frame using the coordinate transformation matrix $\mathbf{Q}$ according to:

$$\begin{aligned} \boldsymbol{\omega}^{i+1} &= \mathbf{Q}\boldsymbol{\omega}'' \\ &= \Omega^{i+1}\left(\omega_1^{i+1}, \omega_2^{i+1}, \omega_3^{i+1}\right) \end{aligned} \tag{5.29}$$

6. The new positions of the rotational axis from the changes in moment of inertia, from the deformations $\Delta\mathbf{I}_D$ and from the surface load $\Delta\mathbf{I}_L$, are used to define the pressure from the centrifugal potential again. The centrifugal potential needs to be applied to these new positions of the rotational axis per time step. This is the part where the polar wander feeds back into the numerical model. For a new coordinate system definition in `Abaqus` a point on the x-axis and a point in the x-y plane of the new coordinate system needs to be entered in coordinates in the initial local frame. The z-axis is then automatically defined using the right-hand rule. A point on the y-axis can be used as a point on the x-y plane when the x-axis is also defined. Therefore, the x- and y- axis need to be defined to be able to define the new local coordinate systems for each time step in `Abaqus`.

   The z-axis coincides with the rotational axis and is therefore already defined with the new rotational axis definition for each time step. Figure 5.3 and Equation 5.30 present the definition of the direction of the z'-axes from the new rotational axes $\boldsymbol{\omega} = \Omega(\omega_1, \omega_2, \omega_3)$:

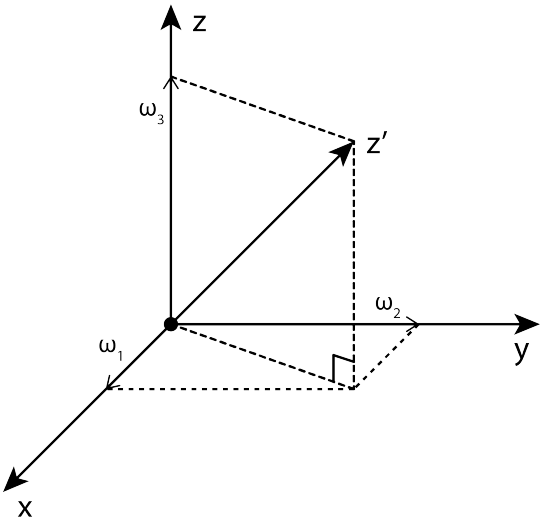

Figure 5.3: The definition of the new rotational axis z' from $(\omega_1, \omega_2, \omega_3)$.

$$z' = \begin{bmatrix} \omega_1 \\ \omega_2 \\ \omega_3 \end{bmatrix} \tag{5.30}$$

Equation 5.30 corresponds with using the coordinate transformation matrix $\mathbf{Q}$, in which z' presents the direction of the rotational axes in the local frame, which needs to be converted to the initial local frame:

$$z' = \mathbf{Q}z = \begin{bmatrix} \omega_3 + \frac{\omega_2^2}{1+\omega_3} & -\frac{\omega_1\omega_2}{1+\omega_3} & \omega_1 \\ -\frac{\omega_1\omega_2}{1+\omega_3} & 1 - \frac{\omega_2^2}{1+\omega_3} & \omega_2 \\ -\omega_1 & -\omega_2 & \omega_3 \end{bmatrix} \begin{bmatrix} 0 \\ 0 \\ 1 \end{bmatrix} = \begin{bmatrix} \omega_1 \\ \omega_2 \\ \omega_3 \end{bmatrix} \tag{5.31}$$

The same approach is used to define the x-axes and y-axes of the new local frames in the initial local frame:

$$x' = \mathbf{Q}x = \begin{bmatrix} \omega_3 + \frac{\omega_2^2}{1+\omega_3} & -\frac{\omega_1\omega_2}{1+\omega_3} & \omega_1 \\ -\frac{\omega_1\omega_2}{1+\omega_3} & 1 - \frac{\omega_2^2}{1+\omega_3} & \omega_2 \\ -\omega_1 & -\omega_2 & \omega_3 \end{bmatrix} \begin{bmatrix} 1 \\ 0 \\ 0 \end{bmatrix} = \begin{bmatrix} \omega_3 + \frac{\omega_2^2}{1+\omega_3} \\ -\frac{\omega_1\omega_2}{1+\omega_3} \\ -\omega_1 \end{bmatrix} \tag{5.32}$$

$$y' = \mathbf{Q}y = \begin{bmatrix} \omega_3 + \frac{\omega_2^2}{1+\omega_3} & -\frac{\omega_1\omega_2}{1+\omega_3} & \omega_1 \\ -\frac{\omega_1\omega_2}{1+\omega_3} & 1 - \frac{\omega_2^2}{1+\omega_3} & \omega_2 \\ -\omega_1 & -\omega_2 & \omega_3 \end{bmatrix} \begin{bmatrix} 0 \\ 1 \\ 0 \end{bmatrix} = \begin{bmatrix} -\frac{\omega_1\omega_2}{1+\omega_3} \\ 1 - \frac{\omega_2^2}{1+\omega_3} \\ -\omega_2 \end{bmatrix} \tag{5.33}$$

7. With the local coordinate frame definitions for each time step, which followed from TPW, the pressure from the centrifugal potential can be adjusted in the `Iter.py` script. For the first iteration the pressure from the centrifugal potential was applied to the initial local frame for all time steps because it was assumed that the vector of rotation does not change, thus that $\boldsymbol{\omega}^{i+1} = \boldsymbol{\omega}^{i}$. A pressure from the centrifugal potential was created at the start of the first time step and propagated through all coming time steps since the rotational axis remained the same. Thus only one pressure per layer surface was created. These pressures need to be removed for the next iteration, since for the next iteration the rotational axis changes per time step and one needs to define one pressure per layer surface per time step. However, in `Abaqus` it is not possible to remove previously created pressured loads and it is also not possible to deactivate pressure loads in the time step they were created in. Therefore, the magnitude of the pressure is multiplied with 1e-99 such that these pressures won't play a role in the simulation anymore.

   With the newly computed rotational rate of the body per time step from Equation 5.27 new centrifugal potentials can be computed at the surface of the model according to Equation 3.9 for each time step. Subsequently, new pressures from the new centrifugal potentials can be computed for at the CMB, at the solid-solid internal boundaries, and at the model surface, according to Equations 3.10, 3.11, and 3.12, respectively. These new pressured loads from the new centrifugal potentials are applied in the new local frames defined by the x'- and y'-axes for all time steps. For all iterations after the second one, the pressure loads from the centrifugal potential will overwrite each other so the removal or deactivation of pressure loads is not required. Together with the procedure described in Chapter 4, the FE analysis can be performed again until convergence of the nodal displacements is achieved. Thus steps 2 to step 7 are performed until convergence of the results.

The complete implementation of true polar wander in the numerical model is explained. Figure 5.4 presents a schematic overview of the coupling of the FE model to the Laplace equation including true polar wander. The iteration between radial displacements and perturbed gravitational potential already existed, as shown in Figure 4.3 in Chapter 4. The parts added to the code in this research are the ones in which true polar wander is computed from the changes in moment of inertia of the surface load and the deformations, and the feedback of true polar wander into the FE analysis. As can be seen from the scheme and as explained, the perturbed gravitational potential ϕ_1 and the centrifugal potential ϕ_c are iterated for simultaneously for all time steps. This simultaneous iteration will show to have a large impact on the TPW prediction, which was not clear before. The verification tests of the code are presented in the next Chapter 6.

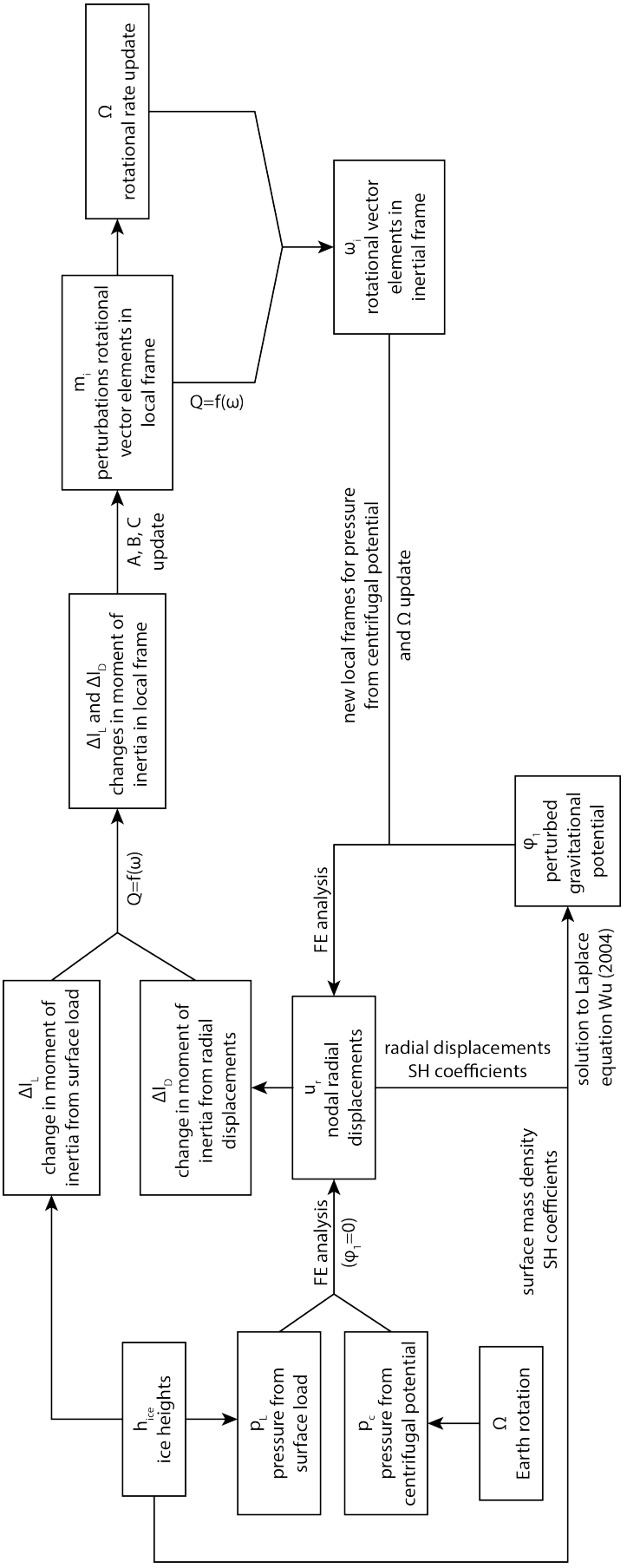

Figure 5.4: Schematic overview of the coupling of the FE model to the Laplace equation including true polar wander.

6

Code verification tests: results and discussion

In this chapter the code verification tests are described, and their results are presented and discussed. For each test it is specified what parts of the code are tested by providing the schematic overview from Figure 5.4 and indicating in red the parts of the code of interest. The tests are performed with lateral homogeneous Earth models such that the numerical results can be compared with results from analytical methods. Once the code is benchmarked and verified, heterogeneous Earth models can be used to further investigate the effect of lateral viscosity variations on glaciation-induced true polar wander.

In Section 6.1 the change in moment of inertia from a movement of the rotational axis and separately from a surface load is investigated, and the radial displacements from a realistic ice load. The change in moment of inertia from a forced movement of the rotational axis $\Delta\mathbf{I}_{D,c}$, when a surface load is not introduced, is compared to the analytical expression for the change in moment of inertia from the equatorial bulge readjustment $\Delta\mathbf{I}_3$. The change in moment of inertia from deformation from a surface load $\Delta\mathbf{I}_{D,L}$, when rotation is not introduced, is compared to the analytical expression for $\Delta\mathbf{I}_2$. Also, their sensitivities to variables in the numerical approach are investigated. The radial displacements from a realistic ice load, the ICE-3G ice history (Tushingham and Peltier, 1991), are compared to the results from the normal mode method to GIA (Martinec et al., 2018; Peltier, 1976; Vermeersen and Sabadini, 1997).

In Section 6.2 is described that to be able to study the Earth's rotational behavior induced by surface loads, the model needs to be in hydrostatic equilibrium. The centrifugal potential needs to be applied for a long enough time to the initial local frame such that the model is flattened and does not change shape anymore, or within certain boundaries, under the centrifugal forcing. The fluid Love number of the laterally homogeneous body from the normal mode method (Peltier, 1976; Vermeersen and Sabadini, 1997) is compared to the degree 2 tidal Love number, which is a function of the perturbed gravitational potential, from the numerical method (Wu and Wang, 2006). Also, the change in moment of inertia between two time steps is investigated.

In Section 6.3 the results from the true polar wander implementation in the numerical model are presented. The TPW direction and magnitude for a constant point mass and ICE-3G surface load are investigated for which the deformation due to surface load is not taken into account, and compared to results from Hu et al. (2017b) and Mitrovica et al. (2001). Since the TPW solution is not as expected, possible causes need to be identified by isolating components of the code. The accuracy of TPW to the change in moment of inertia around the principal axes, from a difference in analytical and numerical hydrostatic equilibrium, is investigated. Furthermore, the effect of the time step size on the numerical TPW solution is discussed. The last test investigates the implication of the simultaneous iteration of the centrifugal potential and the perturbed gravitational potential over all time steps, by performing the iterations per time step before continuing to the next time step.

6.1. Decoupling rotational axis movement from surface load

The total moment of inertia is described by Equation 5.11. The total change in moment of inertia cannot be solved analytically when the surface load causes the rotational axis to move. $\mathbf{C}(t)$ is then closely linked to $\boldsymbol{\omega}$. However, the surface load and the movement of the rotational axis can be decoupled. One can determine the change in moment of inertia due to a forced movement of the rotational axis causing the equatorial bulge to readjust, analytically described by $\Delta I_{3,ij}(t)$ from Equation 5.10, in which surface loads are not introduced. Separately one can determine the change in moment of inertia due to deformation due to the surface load, analytically described by $\Delta I_{2,ij}(t)$ from Equation 5.9, in which rotation is not introduced. Figure 6.1 presents a schematic overview of the parts of the code tested in Test 1 on the forced movement of the rotational axis, in which surface loads are not introduced. Figure 6.2 presents a schematic overview of the parts of the code tested in Test 2 on the surface load, in which rotation is not introduced.

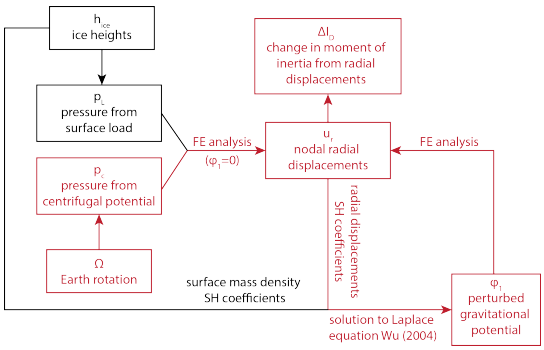

Figure 6.1: Schematic overview of the parts of the code tested in Test 1 on the forced movement of the rotational axis, in which surface loads are not introduced.

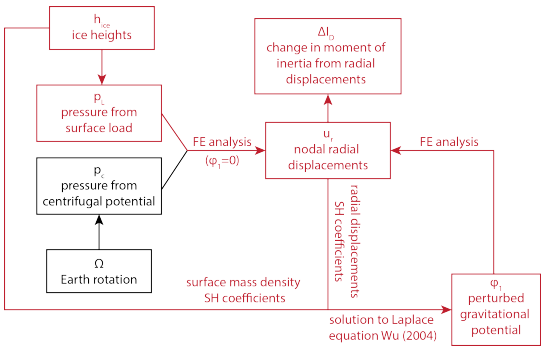

Figure 6.2: Schematic overview of the parts of the code tested in Test 2 on the surface load, in which rotation is not introduced.

The test on the change in moment of inertia from a forced movement of the rotational axis is described in Test 1 in Subsection 6.1.1, and the test on the change in moment of inertia from a surface load is described in Test 2 in Subsection 6.1.2. Since the main purpose of integrating TPW with the numerical model is to study glaciation-induced TPW on the Earth, the displacements from the ICE-3G ice history (Tushingham and Peltier, 1991) are investigated in Test 3 in 6.1.3.

6.1.1. Test 1: change in moment of inertia from forced movement of rotational axis

The numerical solution for the change in moment of inertia from a forced movement of the rotational axis will be compared to the analytical solution for $\Delta I_{3,ij}(t)$ described by Equation 5.10. The equation for the change in moment of inertia from the equatorial bulge readjustment is repeated here:

$$\Delta I_{3,ij}(t) = \frac{k_2^T(t)\,a^5}{3G} * \left(\Omega(t)^2 \left[\omega_i(t)\omega_j(t) - \frac{1}{3}\delta_{ij}\right]\right) \tag{6.1}$$

in which $\Delta I_{3,ij}$ are the components of the inertia tensor $\Delta \mathbf{I}_3$, δ_{ij} is the Kronecker delta function, $k_2^T(t)$ the degree 2 tidal Love number, a Earth's radius, G the gravitational constant, and $\boldsymbol{\omega}(t) = \Omega(t)\,(\omega_1(t), \omega_2(t), \omega_3(t))$ Earth's rotational vector, in which $\Omega(t)$ is the rotational rate of the body, and $(\omega_1(t), \omega_2(t), \omega_3(t))$ a unit vector describing the position of the rotational axis. The rotational axis will be forced to move, drifting from 0° to 45° colatitude in the x-z plane over 5000 years with a constant speed. The constant rotational rate of the Earth is determined by dividing one Earth revolution by the time it takes for one revolution T_{rev}:

$$\Omega = \frac{2\pi}{T_{rev}} = \frac{2\pi}{24 \cdot 60 \cdot 60} = 7.272 \cdot 10^{-5} \quad \text{rad/s} \tag{6.2}$$

From Figure 6.3 the following equations can be derived for the rotational vector elements presented in Equation 6.3. $\omega_2(t)$ is zero in this case because the movement of the rotational axis takes place in the x-z plane. For the definition of the local coordinate systems for each time step in `Abaqus` the origin, a point on the x-axis, and a point on the x-y plane need to be defined, with respect to the global coordinate system. The colatitude θ of the z-axis can be determined from the prescribed movement of the rotational axis.

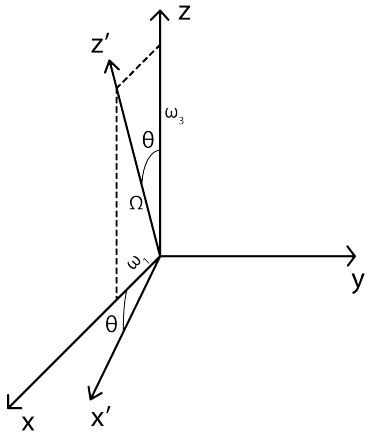

$$\begin{aligned}\omega_1(t) &= \sin\theta(t)\\ \omega_2(t) &= 0\\ \omega_3(t) &= \cos\theta(t)\end{aligned} \tag{6.3}$$

Figure 6.3: Visual representation of the forced axis movement in the x-z plane. z' is the moved rotational axis, Ω the rotational rate, ω_i the rotational vector elements with $i = 1,2,3$ corresponding to the initial x-, y-, and z-axis, respectively, and θ the angle of colatitude over which the rotational axis has moved.

The local coordinate system can be defined in `Abaqus` with respect to the global coordinate system according to the following expressions:

$$\begin{aligned}\text{Origin:} &\quad (0,0,0)\\ \text{Point on the } x\text{-axis:} &\quad (0,-\tan\theta(t),1)\\ \text{Point on the } x\text{-}y \text{ plane:} &\quad (1,-\tan\theta(t),1)\end{aligned} \tag{6.4}$$

Equation 6.1 is simplified by recognizing that a time convolution of the Dirac delta function at time t with a variable at time t equals this variable at time t. By also introducing Equation 5.4 for the tidal Love number, Equation 6.1 becomes:

$$\begin{aligned}\Delta I_{3,ij}(t) &= \frac{k_2^T(t)a^5}{3G} * \left(\Omega^2\left[\omega_i(t)\omega_j(t) - \frac{1}{3}\delta_{ij}\right]\right)\\ &= \frac{\left(k_2^{T,E}\delta(t) + \sum_{i=1}^{M} k_i^T e^{s_i t}\right)a^5}{3G} * \left(\Omega^2\left[\omega_i(t)\omega_j(t) - \frac{1}{3}\delta_{ij}\right]\right)\\ &= \frac{a^5}{3G}\left(k_2^{T,E}\left(\Omega^2\left[\omega_i(t)\omega_j(t) - \frac{1}{3}\delta_{ij}\right]\right) + \sum_{i=1}^{M} k_i^T e^{s_i t} * \left(\Omega^2\left[\omega_i(t)\omega_j(t) - \frac{1}{3}\delta_{ij}\right]\right)\right)\end{aligned} \tag{6.5}$$

Equation 6.5 can be used to analytically solve for the change in moment of inertia of the body due to the forced movement of the rotational axis. $\boldsymbol{\omega}$ is prescribed, the Earth model is defined as well from which a can be obtained, and the tidal Love number variables $k_2^{T,E}$, k_i, and s_i of the model are obtained through the normal mode method (Peltier, 1976; Vermeersen and Sabadini, 1997). The properties of the two-layer Earth model used for this test are presented in Table 6.1 (Hu et al., 2017a).

Table 6.1: Two-layer Earth model properties (Hu et al., 2017a).

Layer	Outer radius [km]	Density [kg m^{-3}]	Shear modulus [Pa]	Viscosity [Pa s]
Mantle	6371	4448	$1.7364{\cdot}10^{11}$	$1{\cdot}10^{21}$
Core	3486	10977	0	0

For the numerical solution the local coordinate frames are defined for each time step from $\boldsymbol{\omega}(t)$. The pressure of the centrifugal potential at each layer surface is then applied in these local coordinate frames according to Equations 3.10, 3.11, and 3.12. The change in moment of inertia, coming from the displacements of the body caused by the pressure from the centrifugal potential $\Delta\mathbf{I}_{D,c}$ solely, can be determined for each iteration. Thus, the analytical solution for $\Delta\mathbf{I}_3$ will be compared to the numerical solution for $\Delta\mathbf{I}_{D,c}$.

The sensitivity of the numerical change in moment of inertia solution to the following five variables, previously introduced in Chapter 3, is investigated:

- $Time$: the time array defines the time at the end of the time steps at which the model is evaluated.
- Res: the number of iterations for the determination of the nodes displacements and the perturbed gravitational potential.
- $Seeds$: the desired global element size for the edges of the mesh elements. Seeds are markers that are placed along the edges of a region to specify the target mesh density of that region. Meshes are generated that match the specified seeds as closely as possible.
- $Degree$: the maximum spherical harmonic degree used in the decomposition of parameters on a spatial grid into spherical harmonic coefficients.
- $CETOL$: the viscoelastic strain error tolerance which specifies the maximum difference in the creep strain increment calculated from the creep strain rates at the beginning and at the end of an increment.

First the effect of the time array on the change of moment of inertia is investigated. Two different time arrays are used with their unit being one thousand years, 1 ka. Within 0 to 10 ka the finer array 'Time 2' contains more time steps than the coarser defined array 'Time 1'.

- 'Time 1' = [0.01, 0.10, 0.15, 0.20, 0.25, 0.30, 0.40, 0.50, 0.65, 0.80, 1.00, 1.30, 1.60, 2.00, 3.00, 4.00, 5.00, 6.00, 8.00, 10.00] ka
- 'Time 2' = [0.01, 0.10, 0.15, 0.20, 0.25, 0.30, 0.40, 0.50, 0.65, 0.80, 1.00, 1.30, 1.60, 1.80, 2.00, 2.15, 2.30, 2.45, 2.60, 2.75, 2.90, 3.00, 3.20, 3.40, 3.60, 3.80, 4.00, 4.20, 4.40, 4.60, 4.80, 5.00, 5.20, 5.40, 5.60, 5.80, 6.00, 6.50, 7.00, 7.50, 8.00, 8.50, 9.00, 10.00] ka

Figure 6.4 presents the change in moment of inertia from the analytical approach and from the numerical approach using two different $Time$ arrays 'Time 1' and 'Time 2'. Res is set to 10, $Seeds$ to 400 km, $Degree$ to 45, and $CETOL$ to 1e-5.

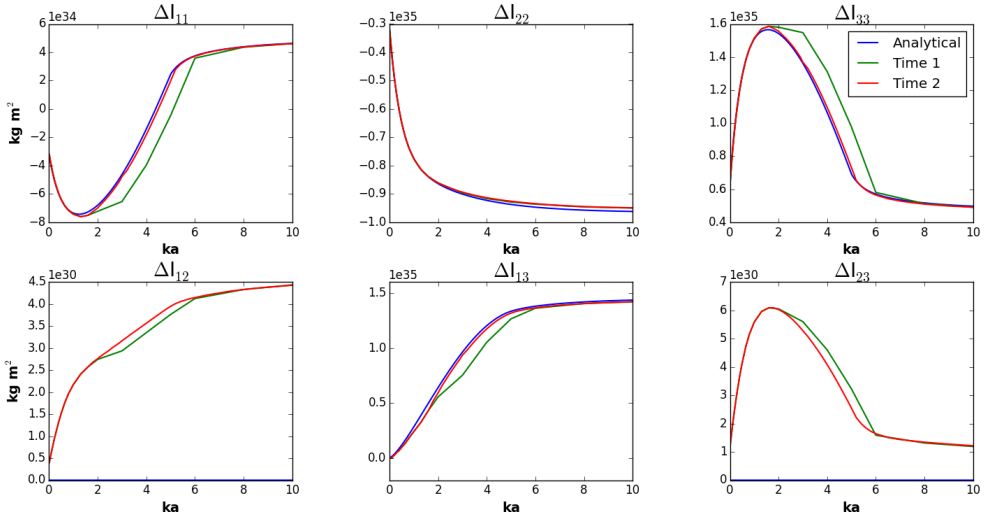

Figure 6.4: Change in moment of inertia for a two-layer Earth model with the rotational axis drifting from 0° to 45° colatitude in the x-z plane over 5000 years with a constant speed with the analytical solution in blue, and the numerical solutions after 10 iterations with a coarse time array 'Time 1' in green, and with a fine time array 'Time 2' in red.

The time array has a significant effect on the change in moment of inertia solution as 'Time 2' better resembles the analytical solution than 'Time 1'. 'Time 2' includes more time steps than 'Time 1' at times where the gradient of the change in moment of inertia is large. Furthermore, the analytical solution for ΔI_{12} and ΔI_{23} is zero for each time step since $\omega_2(t)$ is zero, but the numerical solution is not zero. The numerical values of the ΔI_{12} and ΔI_{23} components are 4 orders of magnitude smaller than the other theoretically non-zero components of the inertia tensor. These numerical errors are a result of the FE method and decrease with

a higher mesh resolution. Note that a higher mesh resolution increases computation time. Next, the effect of the number of iterations on the change in moment of inertia solution is investigated. Figure 6.5 presents the change in moment of inertia from the analytical approach and from the numerical approach for iteration 1 to 10. The time array is the finer 'Time 2', $Seeds$ is set to 400 km, $Degree$ to 45, and $CETOL$ to 1e-5.

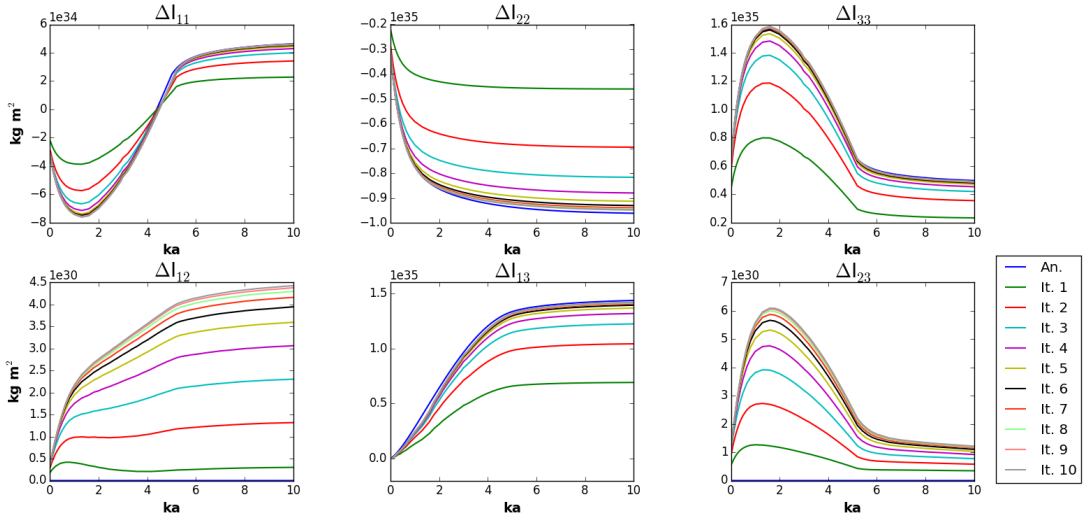

Figure 6.5: Change in moment of inertia for a two-layer Earth model with the rotational axis drifting from 0° to 45° colatitude in the x-z plane over 5000 years with a constant speed with the analytical solution in blue, and the numerical solutions per iteration indicated by the other colors with a fine time array 'Time 2'.

As can be seen the numerical solution resembles the analytical solution better for a higher number of iterations. This is logical, since the model is based on an iterative process between radial displacements and perturbed gravitational potential, and for an increasing number of iterations the result will converge, as explained in Chapter 4. Also noticeable is that for this test there is little improvement anymore after iteration 6.

Looking back at Figure 6.4 at the numerical solution for the 'Time 2' array and the analytical solution, there is little difference in change of moment of inertia between the solutions. The difference that is present can partly be overcome by an even finer time array. Remaining differences can come from the numerical error introduced through mainly the mesh resolution. A higher mesh resolution of 200 km slightly improves the resemblance of the analytical solution, but numerical errors will always be present due to the discretization of the models which lies at the heart of FEM. The error at 10 ka for all theoretically non-zero components of the inertia tensor is ~1% or ~1e32 kg m^2 for a 400 km mesh resolution.

The effect of the maximum spherical harmonic degree and the creep error tolerance are also investigated for this case of the forced movement of the rotational axis. However, the solutions for a maximum spherical harmonic degree of 30, 45, and 100 do not differ from one another. The movement of the rotational axis will mainly be visible in the degree 2 spherical harmonics, and with a maximum spherical harmonics degree of 30 these low degrees are determined with sufficient accuracy. The solutions for a creep error tolerance of 1e-3, 1e-5, and 1e-7 also do not differ from one another. A larger creep error tolerance allows for larger time increments for the numerical integration and thus for a faster simulation time. Hu et al. (2017a) also showed that the combinations of the inertia tensor which are of importance for TPW, $\Delta I_{13}(t)/(C-A)$ and $\Delta I_{23}(t)/(C-B)$, show good agreement with the analytical solution for a given TPW history.

6.1.2. Test 2: change in moment of inertia from surface load

The numerical solution for the change in moment of inertia from the deformation induced by a surface load, in which rotation is not introduced, will be compared to the analytical solution for $\Delta I_{2,ij}(t)$ described by Equation 5.9. The equation for the change in moment of inertia from the deformation induced by a surface load is repeated here:

$$\Delta I_{2,ij}(t) = k_2^L(t) * C_{ij}(t) \tag{6.6}$$

in which $\Delta I_{2,ij}(t)$ and $C_{ij}(t)$ are the components of the inertia tensor $\mathbf{I}_2(t)$ and $\mathbf{C}(t)$, respectively, and $\mathbf{C}(t)$ is convoluted with the degree 2 load Love number $k_2^L(t)$. With the expression for the degree 2 load Love number from equation 5.3, $\Delta I_{2,ij}(t)$ becomes:

$$\begin{aligned}\Delta I_{2,ij}(t) &= k_2^L(t) * C_{ij}(t) \\ &= \left(k_2^{L,E}\delta(t) + \sum_{i=1}^{M} k_i^L e^{s_i t}\right) * C_{ij}(t) \\ &= k_2^{L,E} C_{ij}(t) + \sum_{i=1}^{M} k_i^L e^{s_i t} * C_{ij}(t)\end{aligned} \tag{6.7}$$

The load Love number variables $k_2^{L,E}$, k_i, and s_i of the model are obtained through the normal mode method (Peltier, 1976; Vermeersen and Sabadini, 1997). The moment of inertia of the surface load $C_{ij}(t)$ is determined similarly to the change in moment of inertia of the body due to the radial displacements, described in Section 4.2, according to:

$$\mathbf{C}(t) = \rho_{ice} R^4 \iint_{\Omega} h_{ice}(\theta,\lambda,t) \begin{bmatrix} \sin^2\theta\sin^2\lambda + \cos^2\theta & -\sin^2\theta\cos\lambda\sin\lambda & -\sin\theta\cos\lambda\cos\theta \\ -\sin^2\theta\cos\lambda\sin\lambda & \sin^2\theta\cos^2\lambda + \cos^2\theta & -\sin\theta\sin\lambda\cos\theta \\ -\sin\theta\cos\lambda\cos\theta & -\sin\theta\sin\lambda\cos\theta & \sin^2\theta\left(\cos^2\lambda + \sin^2\lambda\right) \end{bmatrix} \sin\theta d\theta d\lambda \tag{6.8}$$

The used surface load is a symmetric ice sheet around the z-axis located at the south pole with a linearly increasing ice height from 0 to 1000 m from 160° to 170° colatitude and a constant 1000 m ice height from 170° to 180° colatitude, on a 0.5° grid with a total mass of $8.4{\cdot}10^{18}$ kg. The ice load is constant with time. The analytical and numerical procedure can be used for non-constant and non-symmetric loads as well. For the numerical approach pressure from the surface load is applied to the outer surface of the model according to Equation 3.20. The change in moment of inertia can be determined for each iteration. This change in moment of inertia comes from the displacements of the body caused by the pressure from the surface load $\Delta\mathbf{I}_{D,L}$ solely. Thus, the analytical solution for $\Delta\mathbf{I}_2$ will be compared to the numerical solution for $\Delta\mathbf{I}_{D,L}$. Again, the sensitivity of the numerical change in moment of inertia solution to the time array $Time$, the number of iterations Res, the desired element edge size $Seeds$, the maximum spherical harmonic degree $Degree$, and the creep error tolerance $CETOL$, is investigated.

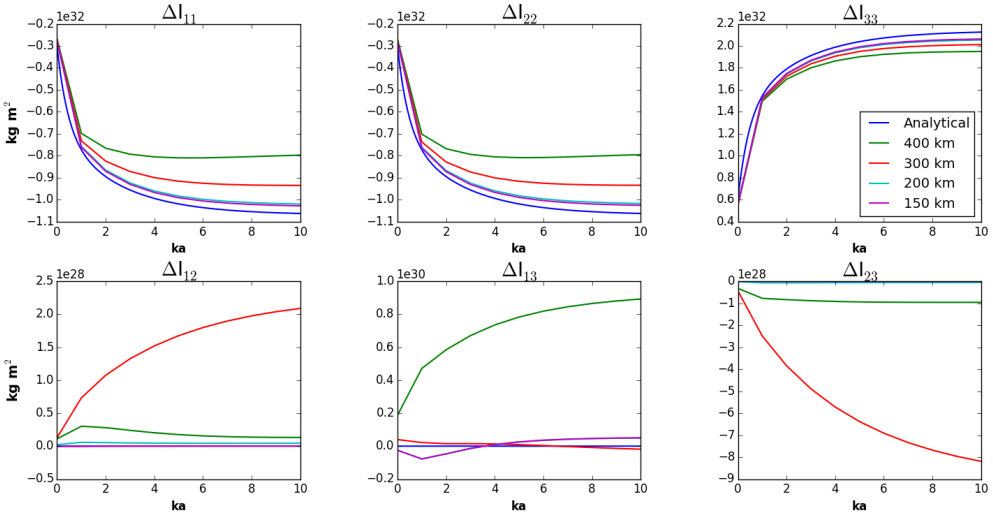

Figure 6.6: Change in moment of inertia for a two-layer Earth model with a constant surface load centered around the south pole with increasing ice thickness towards the pole with the analytical solution in blue, and the numerical solution after 3 iterations for different mesh resolutions of 400 km, 300 km, 200 km, and 150 km.

Figure 6.6 presents the change in moment of inertia due to deformation from a surface load after 3 iterations and mesh resolutions of 400 km, 300 km, 200 km, and 150 km. The time array, defining the end of the time steps, is [0.0001, 1.0, 2.0, 3.0, 4.0, 5.0, 6.0, 7.0, 8.0, 9.0, 10.0] ka. The first step is very short such that the elastic part of the viscoelastic response to the surface load is found. $CETOL$ is set to 1e-5 and $Degree$ to 45.

As can be seen the numerical solution improves for a smaller desired global element edge size, or a higher mesh resolution. For a mesh resolution from 200 km to 150 km there is little improvement for an input surface load on a 0.5° or ~56 km grid. Because the surface load is spherical around the z-axis the off-diagonal elements of the inertia tensor ΔI_{12}, ΔI_{13}, and ΔI_{23} should be zero. The ΔI_{12} and ΔI_{23} components have a larger error for a 300 km than for a 400 km mesh resolution. However, this error does converge to smaller values for a higher mesh resolution. Also, the numerical values of the three off-diagonal components are 3 orders of magnitude smaller than the theoretically non-zero components of the inertia tensor for a mesh resolution of 300 km and higher. As with Test 1 these numerical errors are a result of the FE method and it is also shown that the values decrease with a higher mesh resolution. A 200 km mesh resolution is the best choice when considering accuracy of the solution and computation time.

Next, the effect of the number of iterations on the change in moment of inertia solution is investigated. Figure 6.7 presents the change in moment of inertia due to deformation due to a surface load from the analytical approach and from the numerical approach for iteration 1 to 5 for a mesh resolution of 200 km. $Time$, $CETOL$ and $Degree$ are the same as in the previous simulation.

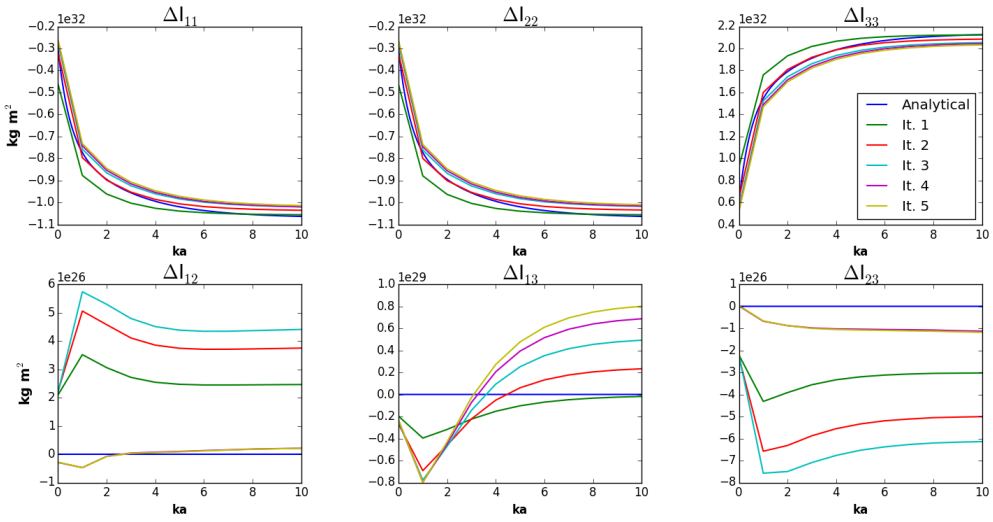

Figure 6.7: Change in moment of inertia for a two-layer Earth model with a constant surface load centered around the south pole with increasing ice thickness towards the pole with the analytical solution in blue, and the numerical solutions per iteration indicated by the other colors using a 200 km mesh resolution.

There is little improvement from iteration 4 to 5. With a 200 km mesh resolution and a sufficient amount of iterations of 5, the numerical solution does not resemble the analytical solution as closely as expected. The error at 10 ka for all theoretically non-zero components of the inertia tensor is ~4% or 5e30 kg m^{-2}. Paulson (2006) also finds a 4% error in topography using FEM, for the case without polar wander and ocean load. In the analytical solution with the normal model method the Maxwell solid is viscously incompressible (Peltier, 1976), but in the numerical model a phenomenon called pressure checkerboarding could take place due to the use of incompressible materials. Pressure checkerboarding is a behavior where large oscillating stresses occur without significant displacements, and typically occurs for hydrostatic stresses in nearly incompressible materials in confined elements. In nonlinear analysis of the displacements of the mesh elements these large oscillating hydrostatic stresses can interact with the displacements and can thereby cause convergence problems. Checkerboarding is more likely to occur in regular meshes. Therefore, it is suggested that mesh irregularities are introduced to study whether checkerboarding can be the cause of the difference between the analytical and numerical solution. This effect is not further investigated here, due to the rigorous adjustment required to the mesh generation. Furthermore, it is not known yet what the effect is of the errors in the inertia tensor due to the surface load on TPW. The effect of pressure checkerboarding is left for future research.

Another cause of the difference can be that `Abaqus` interpolates the pressure between grid points of the expression field, and that they may not exactly correspond with the surface ice cap. TPW may or not may not be affected by these numerical errors depending on the magnitude of the change in moment of inertia from a change in rotational axis position and from a surface load.

The numerical solutions for different values for the creep error tolerance *CETOL* of 1e-3, 1e-5, and 1e-7 do not differ from one another for all components of the inertia tensor for this surface load. This could be due to sufficiently small time increments in the integration. A creep error tolerance of 1e-3 may be conservative enough for the case of both rotation of the body and surface loads for the stress increments to be determined with sufficient accuracy for convergence on the time scale used in Test 1 and 2. For a constant surface load the numerical solution in change of moment of inertia remained the same for finer defined time arrays. A finer time array may be required for a surface load which changes fast, thus causing large gradients in the change in moment of inertia. For this spherical ice cap the maximum spherical harmonic degree of 30, 45, or 100, does not have an effect on the solution. However, for a surface load which spatially changes not as smooth as the spherical ice cap, such as a point mass, the maximum spherical harmonic degree may have an effect on the solution. Signal leakage can be minimized by including more degrees for the spherical harmonic decomposition of a surface load into its coefficients, as presented in Appendix E.2.

6.1.3. Test 3: radial displacements from ICE-3G

In this test the order of magnitude of the surface radial displacements are investigated using a realistic ice history. The implementation of TPW in the numerical model is useful for glaciation-induced TPW predictions, and therefore this test uses a realistic ice history, the ICE-3G model (Tushingham and Peltier, 1991). Figure 6.8 present the parts of the code tested in Test 3 on the radial displacements induced by a realistic ice history.

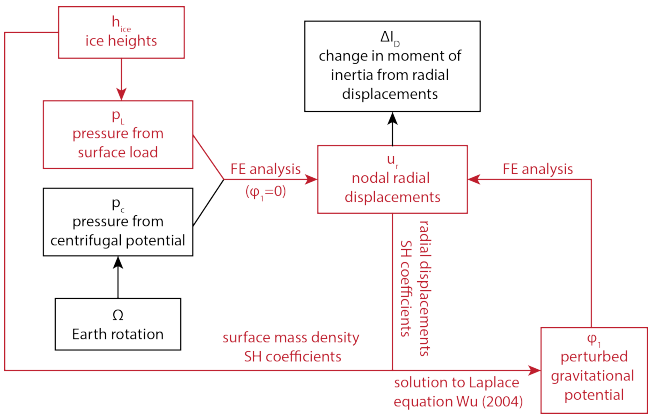

Figure 6.8: Schematic overview of the parts of the code tested in Test 3 on the radial displacements induced by the ICE-3G ice history.

For the test the ICE-3G at the Last Glacial Maximum (LGM) minus the present day is applied when the model is in hydrostatic equilibrium, further discussed in Section 6.2. The model used in this test is the laterally homogeneous four-layer Earth model (Mitrovica et al., 2001) presented in Table 6.2, which is also later used in Test 6 in Subsection 6.3.1 to compare TPW directions.

Table 6.2: Four-layer Earth model properties (Mitrovica et al., 2001).

Layer	Outer radius [km]	Density [kg m^{-3}]	Shear modulus [Pa]	Viscosity [Pa s]
Lithosphere	6371	3150	$0.5878 \cdot 10^{11}$	$1 \cdot 10^{24}$
Upper mantle	6276	3628	$0.8832 \cdot 10^{11}$	$1 \cdot 10^{21}$
Lower mantle	5701	4891	$2.2096 \cdot 10^{11}$	$2 \cdot 10^{21}$
Core	3480	10925	0	0

The load is kept constant for 90 ka after which it linearly decreases to 100 ka, assumed to be at present day, in time steps of 2 ka. Note that this test is only useful for benchmarking, but not for realistic results. For realistic results the ice mass should linearly increase over 90 ka and not instantly applied and kept constant.

The ICE-3G ice height history at LGM, 18 ka before present (bp), at present day, 0 ka bp, and the difference between LGM and present day are presented in Figure 6.9.

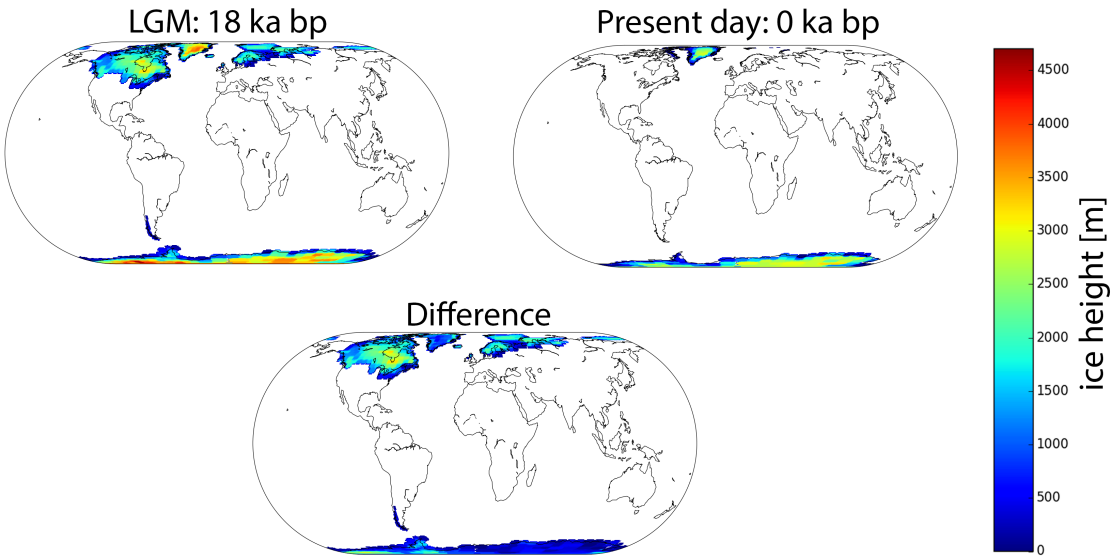

Figure 6.9: ICE-3G ice height history at LGM, 18 ka before present (bp), at present day, 0 ka bp, and the difference between LGM and present day.

Nowadays there are still ice masses mainly over Greenland and Antarctica. During the LGM these ice masses were larger, and there were ice masses over North America, the Laurentian ice sheet, and over Scandinavia, the Fennoscandian ice sheet. For the constant load over 90 ka the present-day ice heights are subtracted from the LGM ice heights such that at 100 ka, or at present day, there will be no loads on the body anymore. The radial displacement results from the numerical approach are compared to analytical results based on the normal mode method (Peltier, 1976; Vermeersen and Sabadini, 1997) for the laterally homogeneous four-layer Earth model. The convolution of the load Love numbers with a realistic surface load, without the sea level equation, was benchmarked in Martinec et al. (2018), and the numerical FE results were provided by Wu and Van der Wal (2003).

The time steps are defined such that the ice height at 92 ka is 80% of the total, at 94 ka 60% of the total etc. and that the decrease takes place in between the 2 ka time steps. Figure 6.10 presents the linearly decreasing surface load application over 10 ka.

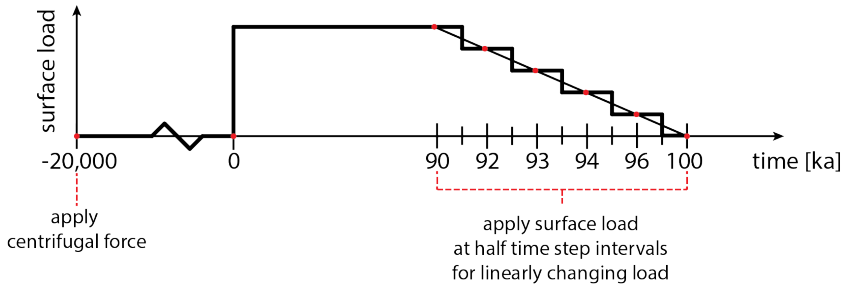

Figure 6.10: Test 3 linearly decreasing surface load application over 10 ka.

The surface radial displacements from the numerical method are compared to the results from the analytical method, which test set-up is similar, at 90 ka and 100 ka after surface load application. The analytical results are provided by Van der Wal (personal communication). Figure 6.11 presents the radial displacements from the numerical method for a mesh resolution of 400 km and after 5 iterations, and from the analytical method at 90 ka and 100 ka, for which the ICE-3G LGM minus present-day load linearly decreases over the last 10 ka.

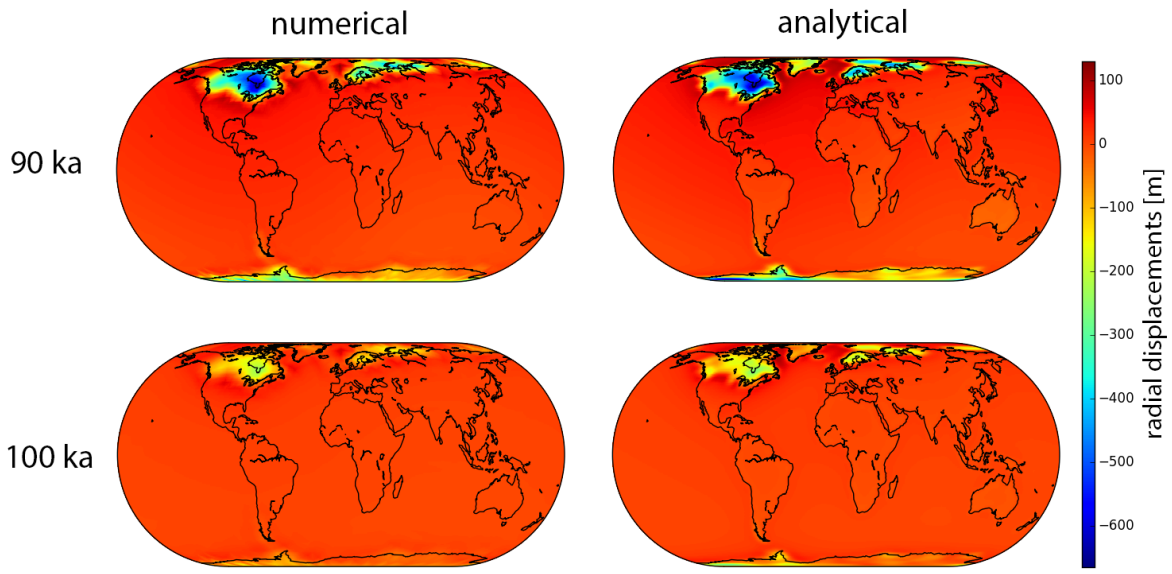

Figure 6.11: Surface radial displacements from the numerical method for a mesh resolution of 400 km and after 5 iterations and from the analytical method at 90 ka and 100 ka after hydrostatic equilibrium for which the ICE-3G LGM minus present day load linearly decreases over the last 10 ka.

The radial displacements after 90 ka look very similar for both methods. In the analytical method, based on the Love numbers, a maximum spherical harmonic degree of 120 is used. The largest displacement from the numerical method is -653.0 m and from the analytical method -666.0 m at 77.344°W longitude. Differences can come from the different resolutions, which is in the numerical method based on the mesh resolution, and in the analytical method on the maximum degree for spherical harmonic decomposition, which also introduces errors. Also, for the numerical method the surface load is shown for 90 ka, and for the analytical method for 91 ka, which can cause a small difference in displacements. Another difference can come from that for the numerical method the surface load is applied after hydrostatic equilibrium, and for the analytical method the surface load is applied to a non-rotating Earth.

After 100 ka, when the load is zero, the displacements from the analytical method are larger than for the numerical method. Figure 6.12 presents the surface radial displacements for both methods at the 77.344°W longitude of largest displacements.

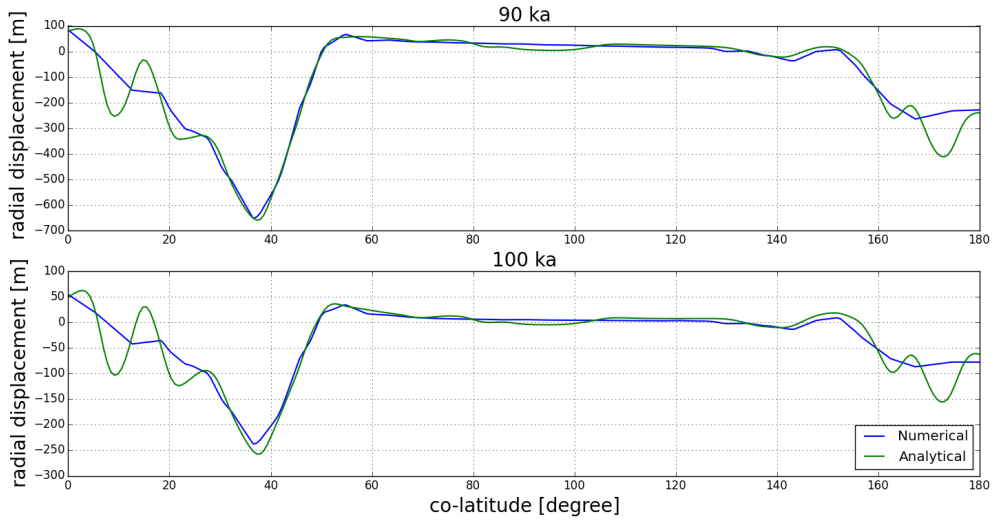

Figure 6.12: Surface radial displacements from the numerical method for a mesh resolution of 400 km and after 5 iterations and from the analytical method at 90 ka and 100 ka after hydrostatic equilibrium for which the ICE-3G LGM minus present-day load linearly decreases over the last 10 ka, at the 77.344°W longitude of largest displacements.

Clearly shown here is that after 90 ka the displacements are very similar over North-America. The 77.344°W longitude line runs through the parts of Greenland and Antarctica where in the analytical results larger displacements are modeled than for the numerical method. In combination with the displacements over the sea floor, the signal shows this wobbling feature. Also clearly visible here, is that after 100 ka the maximum radial displacement over North-America differs more than after 90 ka between the methods, from a ~2% difference at 90 ka to a ~9% difference at 100 ka. A possible cause for this difference in results can be the resolution difference. As shown in Test 2, the mesh resolution has a large impact on the change in moment of inertia, which is based on the radial displacements. A mesh resolution of 400 km can result in radial displacements largely deviating from the analytical solution. Also, in `Abaqus` the input surface load, on a constant grid with a grid size of 0.703°, is interpolated to the mesh of the model, resulting in inaccuracies. Another cause can be the definition of the time steps. Time increments in the numerical integration might be too large, thereby causing strain errors which propagate through time. Decreasing the creep error tolerance might solve this.

It is shown that the numerical solution of radial displacements for a realistic ice mass deviates from the analytical solution. Since for the remainder of the research on TPW a constant load is considered, the displacement difference at 100 ka will not be further investigated. When TPW induced by realistic ice histories is investigated, multiple ice cycli need to be incorporated in the applied surface load, and thus loads will have to increase and decrease over time. Then, the first step is to come back at these radial displacement differences after the linearly decreased load and see what the effect will be of using a finer mesh resolution of 200 km and incorporating smaller time steps to potentially decrease the strain error in the numerical integration.

6.2. Model in hydrostatic equilibrium

To be able to study the Earth's rotational behavior induced by surface loads, the model needs to be in hydrostatic equilibrium. As explained in Subsection 5.5.1 the centrifugal potential needs to be applied for a long enough time to the initial local frame such that the model is flattened and does not change shape anymore after that time, or within certain boundaries, under the centrifugal forcing. For a laterally homogeneous body the fluid Love number can be determined from the normal mode method (Peltier, 1976; Vermeersen and Sabadini, 1997) and compared to the degree 2 tidal Love number from the numerical approach (Wu and Wang, 2006) to find at what time the degree 2 tidal Love number is close enough to the fluid Love number such that the model can be considered to have reached equilibrium. This is done in Test 4 in Subsection 6.2.1, and schematically shown in Figure 6.13. Another approach is to investigate the change in moment of inertia between specified time steps, and set a threshold for equilibrium. This is done in Test 5 in Subsection 6.2.2, and schematically shown in Figure 6.14.

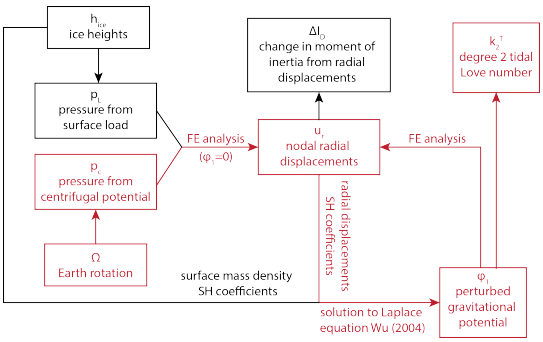

Figure 6.13: Schematic overview of the parts of the code tested in Test 4 on the model in hydrostatic equilibrium from the fluid Love number.

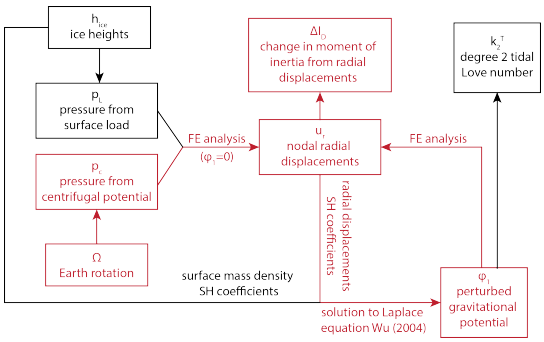

Figure 6.14: Schematic overview of the parts of the code tested in Test 4 on the model in hydrostatic equilibrium from the change in moment of inertia.

6.2.1. Test 4: fluid Love number

The fluid Love number is a measure for the background oblateness of the Earth, and is defined as the fluid limit of the degree 2 tidal Love number as described by Equation 5.16, and repeated here (Munk and MacDonald, 1960):

$$k_f^T = k_2^T(s=0) = k_2^{T,E} - \sum_{i=1}^{M} \frac{k_i^T}{s_i} \tag{6.9}$$

The fluid limit is reached at infinite time. The degree 2 tidal Love number is also a function of perturbed gravitational potential ϕ_1 and the associated Legendre function $P_{2,0}(\cos\theta)$ of degree 2 and order 0 of θ colatitude (Wu and Wang, 2006):

$$\phi_1 = \left(1 + k_2^T\right) P_{2,0}(\cos\theta) \tag{6.10}$$

For a laterally homogeneous body the fluid Love number can be determined from the normal mode method (Peltier, 1976; Vermeersen and Sabadini, 1997) and compared to the degree 2 tidal Love number from the numerical approach (Wu and Wang, 2006) to find at what time the degree 2 tidal Love number is close enough to the fluid Love number such that the model can be considered to have reached equilibrium. For the two-layer Earth model from Table 6.1 the fluid Love number, the degree 2 tidal Love number at infinite time, equals 1.0416. Figure 6.15 presents the fluid Love number, the degree 2 tidal Love number from 0 to 10 ka from the analytical approach described by Equation 6.9, and from the numerical approach described by Equation 6.10 for 12 iterations using a 400 km mesh resolution. The time array used here is [0.0001, 1.0, 5.0, 10.0, 50.0, 100.0, 500.0, 1000.0, 5000.0, 10000.0, 20000.0, 40000.0, 60000.0, 80000.0, 100000.0, 200000.0] ka.

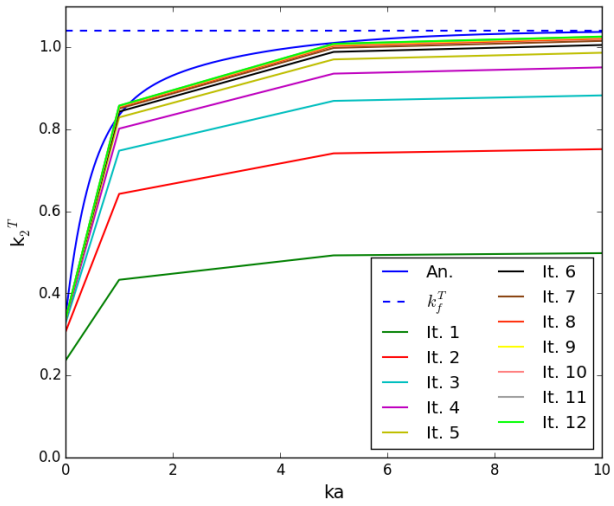

Figure 6.15: The fluid Love number of 1.0461 in dashed blue, the degree 2 tidal love number for 0 to 10 ka from the analytical approach in solid blue and from the numerical approach for 12 iterations indicated by the other colors using a 400 km mesh resolution.

As one can see the analytical degree 2 tidal Love number is better approached with more iterations. The numerical solution between 0 to 10 ka does not look smooth since there are only 4 time steps included in the simulation up to 10 ka. However, from a first sight the numerical solution for the degree 2 tidal Love number does seem to approach the analytical degree 2 tidal Love number. First the effect of the number of iterations is researched. Table 6.3 presents the degree 2 tidal Love number at 200 Ma for all iterations and its percentage compared to the analytical fluid Love number of 1.0461.

Table 6.3: Degree 2 tidal Love number at 200 Ma for all iterations for the two-layer Earth model and its percentage compared to the analytical fluid Love number of 1.0461.

Iteration	1	2	3	4	5	6
k_2^T / k_f^T [%]	47.77	72.08	84.64	91.18	94.60	96.41
k_2^T	0.497598	0.750801	0.881563	0.949701	0.985397	1.004158
Iteration	7	8	9	10	11	12
k_2^T / k_f^T [%]	97.35	97.85	98.12	98.26	98.33	98.37
k_2^T	1.014035	1.019242	1.021988	1.023436	1.024201	1.024605

The analytical fluid love number is better approached with more iterations. However, as one can see the improvement from iteration to iteration decreases and is 0.14% from iteration 9 to 10, 0.07% from iteration 10 to 11, and only 0.04% from iteration 11 to 12. The degree 2 tidal Love number does not seem to reach the fluid Love number in a realistic time range for even more iterations. The difference between the analytical fluid Love number and the numerical approximation of the fluid Love number can be attributed to the discretization in FEM and the numerical integration. The correspondence improves with a higher mesh resolution, which is discussed in Test 5. Now it is of importance to find at what time the model is sufficiently flattened. Table 6.4 presents the degree 2 tidal Love number for all time steps in the simulation for iteration 12 and its percentage compared to the analytical fluid Love number.

Table 6.4: Degree 2 tidal Love number for all time steps for iteration 12 for the two-layer Earth model and its percentage compared to the analytical fluid Love number of 1.0461.

Time [ka]	0.0001	1.0	5.0	10.0	50.0	100.0	500.0	1000.0
k_2^T / k_f^T [%]	32.29	82.36	96.84	98.53	98.71	98.74	98.72	98.61
k_2^T	0.336339	0.857829	1.008725	1.026279	1.028141	1.028451	1.028297	1.027089
Time [Ma]	5.0	10.0	20.0	40.0	60.0	80.0	100.0	200.0
k_2^T / k_f^T [%]	98.38	98.37	98.37	98.37	98.37	98.37	98.37	98.37
k_2^T	1.024692	1.024606	1.024605	1.024605	1.024605	1.024605	1.024605	1.024605

The analytical fluid Love number of 1.0416 is not reached after 200 Ma, and from 20 Ma the degree 2 tidal Love number does not change anymore. The numerical model can approximate the analytical equilibrium for 98.37%. A longer first step will ensure that the model is closer to equilibrium, but it will also result in more time increments within the time step required for the numerical integration. Therefore the choice for the length of the first time step should be a trade-off between these two considerations. The improvement in the degree 2 tidal Love number over a time step, with respect to the numerical value at the end of the time step, is 0.2340% from 1 Ma to 5 Ma, 0.0083% from 5 Ma to 10 Ma, and a mere 0.0002% from 10 Ma to 20 Ma. Glaciation history lengths used in TPW studies are in the order 0.8 Ma, for 8 100 ka cycli. The degree 2 tidal Love number changes for another 0.0478% over the next 0.8 Ma when hydrostatic equilibrium is assumed at 1 Ma, 0.0013% when hydrostatic equilibrium is assumed at 1 Ma, and 0.00002% when hydrostatic equilibrium is assumed at 10 Ma. When restricting the change in degree 2 tidal Lover number over the glaciation history to <0.001%, the two-layer Earth model is considered to have reached equilibrium after 10 Ma for 12 iterations.

Next, the same test is performed with another Earth model, the four-layer Earth model (Mitrovica et al., 2001) presented in Table 6.2, but with a lithospheric viscosity of $1 \cdot 10^{25}$ Pa s, to show how the model properties can affect the number of iterations and the time needed for the model to be considered to have reached equilibrium. Table 6.5 presents the degree 2 tidal Love number at 200 Ma for all iterations and its percentage compared to the analytical fluid Love number of 0.96737, obtained through the normal mode method (Peltier, 1976; Vermeersen and Sabadini, 1997).

Table 6.5: Degree 2 tidal Love number at 200 Ma for all iterations for the four-layer Earth model and its percentage compared to the analytical fluid Love number of 0.96737.

Iteration	1	2	3	4	5	6
k_2^T / k_f^T [%]	49.07	73.49	85.88	92.22	95.49	97.17
k_2^T	0.474689	0.710944	0.830750	0.892111	0.923710	0.940032
Iteration	7	8	9	10	11	12
k_2^T / k_f^T [%]	98.05	98.50	98.73	98.85	98.92	98.95
k_2^T	0.948476	0.952848	0.955114	0.956288	0.956896	0.957212

Again, the analytical fluid love number is better approached with more iterations. However, as one can see the improvement from iteration to iteration decreases and is 0.12% from iteration 9 to 10, 0.07% from iteration 10 to 11, and only 0.03% from iteration 11 to 12.

Now it is of importance to find at what time the model is sufficiently flattened. Table 6.6 presents the degree 2 tidal Love number for all time steps in the simulation for iteration 12 and its percentage compared to the analytical fluid Love number of 0.96737.

Table 6.6: Degree 2 tidal Love number for all time steps for iteration 12 for the four-layer Earth model and its percentage compared to the analytical fluid Love number of 0.96737.

Time [ka]	0.0001	1.0	5.0	10.0	50.0	100.0	500.0	1000.0
k_2^T / k_f^T [%]	31.09	72.44	91.50	95.25	96.89	97.02	97.56	97.87
k_2^T	0.300729	0.700740	0.885178	0.921372	0.937320	0.938587	0.943725	0.946759
Time [Ma]	5.0	10.0	20.0	40.0	60.0	80.0	100.0	200.0
k_2^T / k_f^T [%]	98.55	98.86	99.03	99.05	99.03	99.02	99.01	98.95
k_2^T	0.953387	0.956369	0.957987	0.958150	0.958013	0.957877	0.957748	0.957212

The analytical fluid Love number of 0.96737 is not reached after 200 Ma. The numerical model can approximate the analytical equilibrium for 99.05%. After 40.0 Ma the degree 2 tidal Love number deviates from the fluid Love number. There is no explanation for this behavior. However, the improvement in the degree 2 tidal Love number is 0.6952% from 1 Ma to 5 Ma, 0.3118% from 5 Ma to 10 Ma, 0.1689% from 10 Ma to 20 Ma, and 0.0170% from 20 to 40 Ma. The degree 2 tidal Love number changes for another 0.1390% over the next 0.8 Ma when hydrostatic equilibrium is assumed at 1 Ma, 0.0499% when hydrostatic equilibrium is assumed at 1 Ma, 0.0135% when hydrostatic equilibrium is assumed at 10 Ma, and 0.0007% when hydrostatic equilibrium is assumed at 20 Ma. When restricting the change in degree 2 tidal Lover number over the glaciation history to <0.001%, the four-layer Earth model is considered to have reached equilibrium after 20 Ma for 12 iterations.

Since this finding for the time it takes for the four-layer Earth model to have reached equilibrium is different for the two-layer Earth model, it is shown that one needs to find this time separately for different Earth models. More iterations can also slightly improve the results and more intermediate time steps in the time array will result in less conservative choices for the time to reach equilibrium. More importantly is how this equilibrium state translates to the change in moment of inertia from the non-rotating spherical Earth model to the rotating flattened Earth model. The next Test 5 investigates how the assumed equilibrium compares to the analytical approach in terms of change in moment of inertia and how much the components of the inertia tensor are still subjected to change after 10 Ma for the two-layer Earth model.

6.2.2. Test 5: change in moment of inertia

This test focuses upon how much the components of the inertia tensor of the change in moment of inertia are still subjected to change after 10 Ma for the two-layer Earth model and how the assumed equilibrium compares to the analytical approach. After 10 Ma the two-layer Earth model is assumed to be in hydrostatic equilibrium. The two-layer Earth model is laterally homogeneous and thus the changes in moment of inertia around the principal axes can be determined analytically. The change in moment of inertia from a static non-rotating Earth to a rotating Earth in equilibrium, ΔA, ΔB, and ΔC, is found with Equation 5.15. Table 6.7 presents the change in moment of inertia after 12 iterations after 10 Ma when the two-layer Earth model is in equilibrium and how the assumed equilibrium compares to the analytical approach.

Table 6.7: Change in moment of inertia after 12 iterations after 10 Ma when the two-layer Earth model is in equilibrium and compared to the analytical solution.

ΔI_{ij}	Analytical [kg m^2]	10 Ma [kg m^2]	|An. - 10 Ma| [%]	|20 Ma - 10 Ma| [kg m^2]	|20 Ma - 10 Ma| [%]
ΔI_{11}	-9.62708e34	-9.40888e34	2.2665	1.88619e29	0.0002
ΔI_{22}	-9.62708e34	-9.56099e34	0.6865	1.61861e29	0.0002
ΔI_{33}	1.92542e35	1.88989e35	1.8452	3.57057e29	0.0002
ΔI_{12}	0	-7.61388e30	N/A	6.44959e27	0.0847
ΔI_{13}	0	1.00911e30	N/A	3.07290e27	0.3045
ΔI_{23}	0	-3.38240e30	N/A	1.81725e27	0.0537

First, the change in moment of inertia compared to the analytical solution is considered. The off-diagonal components of the inertia tensor, ΔI_{12}, ΔI_{13}, and ΔI_{23} are supposed to be zero. These components are not zero in the numerical solution but their values are 5 orders of magnitude smaller than the main diagonal components. As shown in Test 1 and Test 2, and shown later in this test, these numerical errors are a result of the FE method and can decrease with a higher mesh resolution. Important to consider is whether these numerical errors can have an effect on the magnitude of true polar wander, which is further investigated in Test 6. For the diagonal components of the inertia tensor ΔI_{11} and Δ_{22} should be equal but they are not, which is also a result of the FEM discretization. These components will show more similarity for a higher mesh resolution, as shown later in this test.

Also indicated by the degree 2 tidal Love number to the analytical fluid number in the previous test, is that the numerical equilibrium state deviates from the analytically determined equilibrium state. This is also visible in that the change in moment of inertia for the diagonal components of the inertia tensor differ from the analytical solution by a few percent. In Test 7 is researched whether these numerical approximations of the diagonal components of the inertia tensor have an effect on TPW.

Second, the change in change in moment of inertia after 10 Ma is considered, coming from the fact that the model is close to equilibrium but still relaxing after 10 Ma since equilibrium is only reached at infinite time. As presented in the last two columns of Table 6.7 the difference in change in moment of inertia between 10 Ma and 20 Ma is only 0.0002% for the diagonal components of the inertia tensor and up to 0.3% for the off-diagonal components. For glaciation-induced true polar wander with a glaciation history of 8 cycli of 100 ka each, the change in change in moment of inertia after 0.8 Ma is approximately 0.03% maximum for the off-diagonal inertia tensor components. However, the small change in the values over 0.8 Ma after 10 Ma of ~1e26 kg m^2 is not significant compared to the numerical error of ~1e30 kg m^2 at 10 Ma. The effect of this numerical error on TPW is investigated in Test 7.

Table 6.8 presents the change in moment of inertia after 12 iterations after 10 Ma when the two-layer Earth model is in equilibrium for a mesh resolution of 400 km and 300 km.

Table 6.8: Change in moment of inertia after 12 iterations at 10 Ma when the two-layer Earth model is in equilibrium for a mesh resolution of 400 km and 300 km and compared to the analytical solution.

ΔI_{ij}	Analytical [kg m^2]	400 km [kg m^2]	|An. - 400 km| [%]	300 km [kg m^2]	|An. - 300 km| [%]
ΔI_{11}	-9.62708e34	-9.40888e34	2.2665	-9.50092e34	1.3105
ΔI_{22}	-9.62708e34	-9.56099e34	0.6865	-9.60134e34	0.2673
ΔI_{33}	1.92542e35	1.88989e35	1.8452	1.90404e35	1.1228
ΔI_{12}	0	-7.61388e30	N/A	-1.29241e30	N/A
ΔI_{13}	0	1.00911e30	N/A	2.38312e30	N/A
ΔI_{23}	0	-3.38240e30	N/A	4.35953e29	N/A

With the higher mesh resolution of 300 km the changes in moment of inertia around the principal axes approach the analytical solution closer, as can be seen in the fourth and last column. Also, ΔI_{11} and ΔI_{22} should be equal for this laterally homogeneous model, and the absolute difference between the two decreases with a higher mesh resolution. The numerical error for the off-diagonal components ΔI_{12} and ΔI_{23} decreases, whilst for the ΔI_{13} component it has doubled. The off-diagonal components of the inertia tensor are still a factor 4 smaller than the diagonal elements. The effect of the numerical error in these components on TPW will be investigated in Test 7. As noticed, up until now only laterally homogeneous models are considered because for these models an analytical solution can be found for the tidal Love number. When introducing lateral viscosity variations one has to investigate the change in degree 2 tidal Love number and the change in moment of inertia again to find the time for which the model is considered to have reached equilibrium.

Also investigated is whether the amount of time steps up to the time at which hydrostatic equilibrium is reached has an effect on the change in moment of inertia solution, presented in Appendix A. It is found that one time step can be used up to hydrostatic equilibrium, which results in a faster computation due to less evaluations of the nodal displacements.

6.3. True polar wander implementation

This section covers the results from the true polar wander implementation in the numerical model. The TPW direction and magnitude for a constant point mass and ICE-3G surface load are investigated for which the deformation due to surface load is not taken into account in Test 6 in Subsection 6.3.1. Since the TPW magnitude is not as expected, possible causes need to be identified by isolating components of the code. The accuracy of the change in moment of inertia of the model in hydrostatic equilibrium may have an effect on TPW. Test 7 in Subsection 6.3.2 investigates the accuracy of TPW to the change in moment of inertia around the principal axes. The effect of the time step size used in the numerical simulation on the TPW solution is discussed in Test 8 in Subsection 6.3.3. The last test investigates the implication of the simultaneous iteration of the centrifugal potential and the perturbed gravitational potential over all time steps, by performing the iterations per time step before continuing to the next time step, in Test 9 in Subsection 6.3.4.

6.3.1. Test 6: TPW direction and magnitude

The TPW direction and magnitude will be discussed for a point mass and a distributed mass for a lateral homogeneous Earth model. Then, the TPW solution can be compared to analytical solutions. The TPW path for the point mass will be compared to the analytical approach of Hu et al. (2017b). This approach is suitable for large angle polar wander and for non-stationary loads with respect to the rotational axis. The TPW path for the distributed mass will be compared to the analytical approach of Mitrovica et al. (2001) based on Wu and Peltier (1984). When the TPW paths from the analytical and numerical solution correspond, lateral viscosity variations can be introduced in the model to study the effect of these model variations on TPW. Here, a more detailed description of the tests is given for the point mass and distributed mass.

The TPW direction and magnitude triggered by a constant $2{\cdot}10^{19}$ kg point mass located at 0° longitude and 45° colatitude is investigated, as well as the TPW direction triggered by a constant ICE-3G LGM minus present day load. For these tests the deformation due to the surface load $\Delta\mathbf{I}_{D,L}$ is not taken into account, but the moment of inertia of the surface load $\Delta\mathbf{I}_L$ is taken into account for the determination of TPW and the spherical harmonic coefficients of the surface mass density $\sigma_{l,m}$ for the determination of the perturbed gravitational potential. Figure 6.16 presents a schematic overview of the parts of the code tested, which are investigated in Test 6 to Test 9.

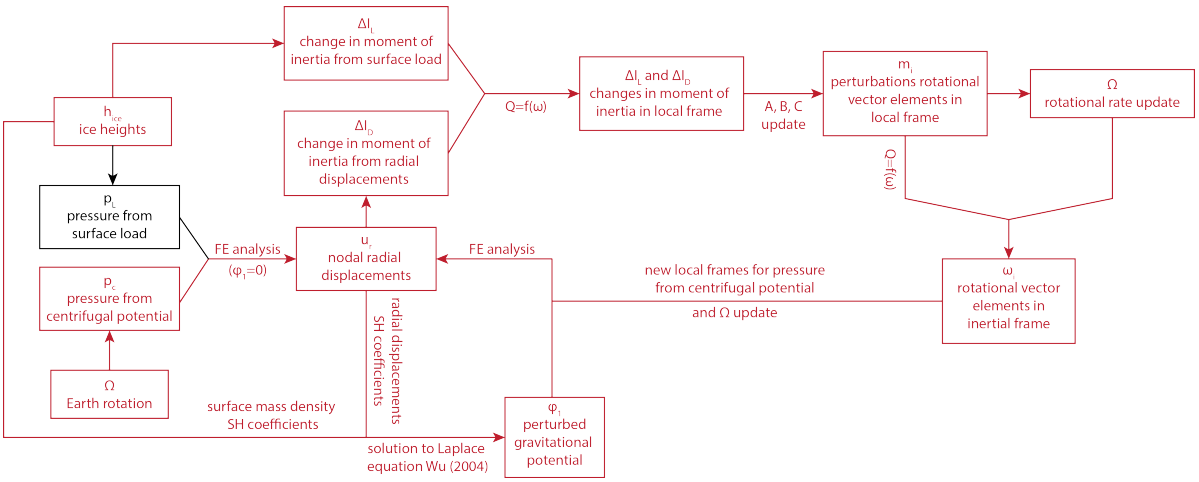

Figure 6.16: Schematic overview of the parts of the code tested in Test 6 to Test 9 on TPW without deformation from the surface load.

For TPW the dimensionless quantities m_i with $i = 1,2,3$ of the perturbed rotational vector are investigated. Their expressions introduced in Section 5.4 are repeated here:

$$m_1 = \frac{\Delta I_{13}(t)}{C-A} \qquad m_2 = \frac{\Delta I_{23}(t)}{C-B} \qquad m_3 = -\frac{\Delta I_{33}(t)}{C} \tag{6.11}$$

m_1 and m_2 give the polar shift in radians. m_1 is in the x-direction, in the equatorial plane from the Earth's center of mass towards the Greenwich meridian. m_2 is in the y-direction, in the equatorial plane from the the Earth's center of mass towards 90° East longitude. m_3 gives the change in the length of day in radians per sidereal day (Sabadini et al., 2016). The inertia tensor components in Equation 6.11 are a summation of the change in moment of inertia from the deformations $\Delta\mathbf{I}_{D,c}$ and the change in moment of inertia of the input load $\Delta\mathbf{I}_L$. The deformations from the surface load $\Delta\mathbf{I}_{D,L}$ are not taken into account. The deformations thus solely come from the application of the centrifugal potential and change in centrifugal potential from the changing local coordinate systems due to TPW. Note that Equation 6.11 is performed in the local coordinate frame to find the new rotational axis position and transformed to the initial local frame as described in Subsection 5.5.2 on the TPW algorithm.

TPW triggered by a point mass

As shown in Test 1, polar wander in the x-z plane is entirely defined by ΔI_{13}. The point mass lies in the x-z plane and thus m_1 will entirely describe the TPW path. Figure 6.17 visualizes the TPW direction for the point mass. For a constant surface load $\Delta\mathbf{I}_L$ in the form of a point mass, polar wander should continue until the point mass has reached the equator. The constant point mass causes a constant strain. Due to the viscoelastic behavior of the Earth, stresses in the body decrease with time for constant strain. Thus, the radial displacements would decrease over time. However, the radial displacements of the body cause a change in the moment of inertia of the body due to the deformations $\Delta\mathbf{I}_{D,L}$ and this together with the change in moment of inertia from the surface load $\Delta\mathbf{I}_L$ causes the axis of maximum moment of inertia to move. To conserve angular momentum the rotational axis moves towards the axis of maximum moment of inertia. The centrifugal force causes $\Delta\mathbf{I}_D$ to keep changing, the equatorial bulge has to readjust with respect to the position of the rotational axis, and the surface load has moved with respect to the position of the rotational axis in the direction of the equator. The axis of maximum moment of inertia is thus being pushed further away by the displacement of the point mass with respect to the rotational axis and by the viscoelastic relaxation of the body due to the change in centrifugal force due to the movement of the rotational axis. This process keeps going until the point mass has reached the equator, when the centrifugal force and self-gravitational force are balanced again. For the positive mass anomaly in the x-z plane for positive x and z, the rotational axis will move in the negative x, or negative m_1 direction, since the axis of maximum moment of inertia moves in the negative m_1 direction.

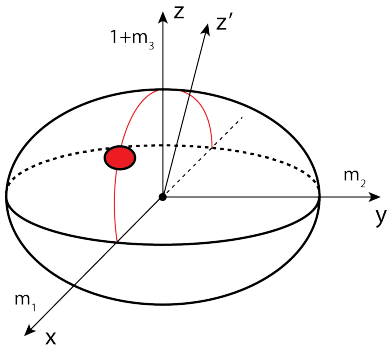

Figure 6.17: TPW direction for a point mass located at 0° longitude and 45° colatitude. The red dot with black encircled is the positive mass anomaly, the red half arc the path the rotational axis will move along when the mass anomaly is located in the x-z plane, at 0° longitude, and z' the new position of the rotational axis.

The time array starting at zero and defining the end of the time steps is as follows: [10000.0, 10000.001, 10001.0, 10002.0, 10003.0, 10004.0, 10005.0] ka. The first time step takes 10 Ma and is determined in Test 4 and 5 for the model in hydrostatic equilibrium. The second step is only 1 year such that the elastic response of TPW from the surface load can be determined. The following steps are all 1 ka until 5 ka after hydrostatic equilibrium. The TPW path will be compared to the analytical method of Hu et al. (2017b), which is benchmarked with TPW from the analytical approach of Wu and Peltier (1984). Both methods do not take into account the deformation of the body due to the surface load.

There is a difference in the analytical approaches of Wu and Peltier (1984) and Hu et al. (2017b). For the analytical approach of Hu et al. (2017b) and the approach implemented in the numerical model, based on Hu et al. (2017a), both $\Delta\mathbf{I}_{D,c}$ and the moment of inertia of the surface load $\Delta\mathbf{I}_L$ are transformed from the initial local frame to the local frames for each time step to compute m_i. Since $\Delta\mathbf{I}_L$ is transformed to the local frame for each step the load is non-stationary. The analytical method from Wu and Peltier (1984) is based on a small angle TPW approximation and therefore uses a stationary load. Hu et al. (2017b) has shown that the method from Wu and Peltier (1984) overestimates TPW by about 2.5% for 2° of TPW for the mass anomaly located at 45° colatitude. This difference between the methods becomes larger when the mass anomaly is located closer to the equator at 90° colatitude or to the poles at 0° and 180° colatitude. The same mass anomaly at 10° colatitude results in a difference in methods of 12.5% after 2° in predicted TPW for the two-layer Earth model. This shows that the applicable range of the use of the linear method is smaller than using the method which takes into account non-stationary loads with respect to the rotational axis to determine TPW.

For Equation 6.11 ΔA, ΔB, and ΔC are updated using the diagonal components of the $\Delta\mathbf{I}_{D,c}$ inertia tensor, which is a result from the body deformations due to the centrifugal potential. From Equation 6.11 can be seen that the moment of inertia of the unperturbed non-rotating body I_0 cancels out for m_1 and m_2, and that it only has an effect on m_3, the change in length-of-day (LOD), or rotational rate. I_0 is chosen to be equal to the value used in Hu et al. (2017b) of 7.2458e37 kg m^2, for the two-layer Earth model. Figure 6.18 presents the TPW path for a $2{\cdot}10^{19}$ kg point mass located at 0° longitude and 45° colatitude from the TPW algorithm implementation in the numerical model for 10 iterations and the analytical approach from Hu et al. (2017b). Note that 0 ka corresponds to the end of the first step in the simulation at 10 Ma for when the model is in hydrostatic equilibrium in all coming TPW plots. The mesh resolution can be coarse, as shown in Test 1, when the deformation of the surface load is not taken into account, and when a point mass is considered. The mesh resolution is set to 500 km for fast computations. $CETOL$ is set to 1e-4, and the maximum spherical harmonic degree to 45.

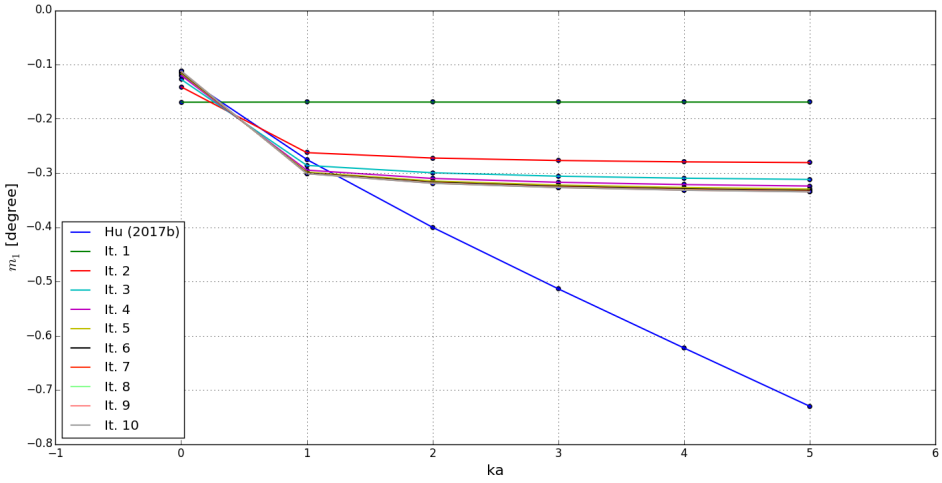

Figure 6.18: TPW path for a $2{\cdot}10^{19}$ kg point mass located at 0° longitude and 45° colatitude from the TPW algorithm implementation in the numerical model for 10 iterations and the analytical approach from Hu et al. (2017b) in blue. The dots indicate the data points. The x-axis indicates the time in ka after 10 Ma. The black dots indicate the end of the time steps.

Here the direction and the magnitude of the TPW triggered by the positive mass anomaly is discussed. After 5 iterations, in gold, the TPW solution is as good as converged, compared to the result after 10 iterations, in grey. As expected the direction of TPW is in the negative m_1 direction. The movement of the rotational axis in the m_2 direction is 3 orders of magnitude smaller than the movement in m_1 direction and comes from the approximation of the point mass on a grid, and numerical errors for the flattening of the Earth after 10 Ma in $\Delta I_{D,23}$. However, the magnitude of TPW is not conform the analytical approach. The TPW converges too fast to a value of ~0.33° in the numerical approach which it should not do.

It now seems as if the equatorial bulge causes too much resistance to the TPW, as described in Section 1.2 in the Introduction. However, there is no high viscosity lithosphere included in the two-layer model and thus TPW should not be counteracted when the surface load remains. The TPW path is not according to expectations. Possible causes need to be identified by isolating components of the code.

In Appendix C is shown that the the part of the code in which the TPW feeds back into the numerical analysis, from the local coordinate system definition for each time step, works correctly. The TPW accuracy to the time step size in the numerical simulation is discussed in Subsection 6.3.3. In Appendix D is shown that the TPW does perform according to expectations for a decrease and increase in mantle viscosity. A higher viscosity mantle material results in less displacements over a certain period of time. A higher mantle viscosity leads to smaller changes in $\Delta \mathbf{I}_D$ and thus in less TPW over that period of time.

Furthermore, the TPW accuracy to the maximum degree for the spherical harmonic decomposition of the surface load and the radial displacements into their coefficients is investigated in Appendix E.2. The TPW solution is overestimated by 1-2% for a low maximum degree of 45. Since the error does not change over time it is safe to perform tests with a low maximum degree for fast computations. However, for a more accurate TPW prediction a high maximum degree is required. Also, in Appendix B.1 is shown that the determination of the change in moment of inertia of the point mass itself $\Delta \mathbf{I}_L$ for a coarse 2° grid of the input surface load only causes a 0.5% error.

These errors still cannot explain the different TPW paths between the numerical and analytical solution. The main reason the TPW from the numerical model does not approach the TPW from the analytical method for a laterally homogeneous Earth lies at the heart of the numerical model, in which the iterations between the radial displacements and centrifugal potential occur simultaneously over all time steps. This will be elaborately discussed in the last Test 9. With the knowledge that the fundamental approach may causes problems in the TPW prediction, the next tests on TPW accuracies described here and in Subsection 6.3.2 and 6.3.3 are performed using the incomplete numerical model.

Important to emphasize is that the change in the rotational rate from the change in length-of-day (LOD) determined from the norm of the perturbed rotational vector elements in the local frame, step 4 of the TPW algorithm implementation in Subsection 5.5.2, is a crucial step for the TPW solution to converge in terms of number of iterations for the radial displacement solution in the FE analysis. The new rotational vector needs to be normalized using the new rotational rate as described by Equation 5.27 and 5.28. This should not be confused with the rotational rate update in the definition of the centrifugal potential which feeds back into the numerical analysis. It is found that this rotational rate update only causes a 0.2% difference in TPW when not included, presented in Appendix E.1.

From Figure 6.18 the initial elastic jump in TPW is investigated. If the first jump is off from what it should be according to Hu et al. (2017b), this could propagate through the next time steps. The TPW result at 1 year after the surface load is applied, is the elastic part of the viscoelastic response to the surface load. In reality the elastic part of the viscoelastic response occurs nearly instantly, but for the numerical method a small time step of 1 year is taken to represents the elastic part of the response. The elastic TPW response is a function of the change in moment of inertia of the point mass $\Delta \mathbf{I}_L$, and of the change in moment of inertia from the deformations, which is caused by the change in centrifugal potential, $\Delta \mathbf{I}_D$. From the approach of Hu et al. (2017b) follows a TPW magnitude of -0.1197° in m_1 direction, and from the numerical model -0.1120° in m_1 direction. For a high mesh resolution of 200 km this initial TPW response is -0.1125° and thus still deviates about 6% from the analytical solution. As previously mentioned, and presented in Appendix B.1, the determination of $\Delta \mathbf{I}_L$ only causes a 0.5% error compared to the analytical approach for a coarse 2° grid of the input surface load.

In the time step which starts at 10 Ma and ends 1 year later, the rotational vector at the start coincides with the z-axis of the initial local frame, at zero TPW. As shown before in Test 5 the $\Delta I_{D,13}$ component of the inertia tensor, describing the change in moment of inertia due to deformations, is not zero after 10 Ma while it should theoretically be zero for a centrifugal potential which is applied to the z-axis of the initial local frame. For the Earth model with a 500 km mesh resolution after 10 Ma this $\Delta I_{D,13}$ equals 8.680e30 kg m^2, and is a numerical error. 1 year later $\Delta I_{D,13}$ equals -1.424e32 kg m^2, due to the surface load applied at 10 Ma which causes TPW and thus a change in deformations from the changed centrifugal potential. The numerical error is 6% of $\Delta I_{D,13}$ after 1 year. However, the ΔI_{13} from Equation 6.11 to compute m_1 also includes the change in moment of inertia from the surface load directly, $\Delta I_{L,13}$, which equals -4.060e32 kg m^2 for the point mass. The total change in moment of inertia ΔI_{13} at 1 year used to compute m_1 is thus -5.483e32 kg m^2. Table 6.9 gives an overview of the change in moment of inertia at 1 year after hydrostatic equilibrium and the numerical error at hydrostatic equilibrium.

Table 6.9: Change in moment of inertia after 5 iterations at 1 year after hydrostatic equilibrium, at 10 Ma, for the two-layer Earth model for a mesh resolution of 500 km.

ΔI	abs. value [kg m^{-2}]	w.r.t ΔI_{13} @ +1 yr
$\Delta I_{D,13}$ @ +1 yr	-1.424e32	26%
$\Delta I_{L,13}$ @ +1 yr	-4.060e32	74%
ΔI_{13} @ +1 yr	-5.483e32	N/A
ΔI_{13} @ 10 Ma	8.680e30	2%

The numerical error at 10 Ma is only 2% of ΔI_{13} at 1 year, and thus cannot fully explain the 6% difference between m_1 at 1 year from the analytical and numerical approach. However, it is not know how the numerical error propagates through time when the rotational axis moves. Thus it could still be well true that the numerical error causes the difference in m_1 between both methods at 1 year.

TPW triggered by a distributed mass

Next to the TPW triggered by a point mass, the TPW triggered by a realistic ice load, a constant ICE-3G LGM minus present day presented in Figure 6.9, is investigated. The main purpose of this test is to check whether the TPW direction triggered by a realistic ice history from the numerical model is conform the TPW direction from analytical methods. This test only concerns the direction and not the magnitude, since it has been shown that the magnitude is not conform analytical approaches. Therefore, there is no need to implement realistic ice cycli. The same test set-up as for the point mass TPW test is used, but the Earth model is the four-layer model (Mitrovica et al., 2001) presented in Table 6.2 with a lithospheric viscosity of $1{\cdot}10^{25}$ Pa s. Figure 6.19 presents the TPW triggered by a constant ICE-3G LGM minus present-day ice load over 5 ka for 10 iterations. The TPW direction can be compared to Figure 6.20 (Mitrovica et al., 2001) which presents the TPW triggered by 8 ICE-3G ice cycli of 100 ka each including an ocean load.

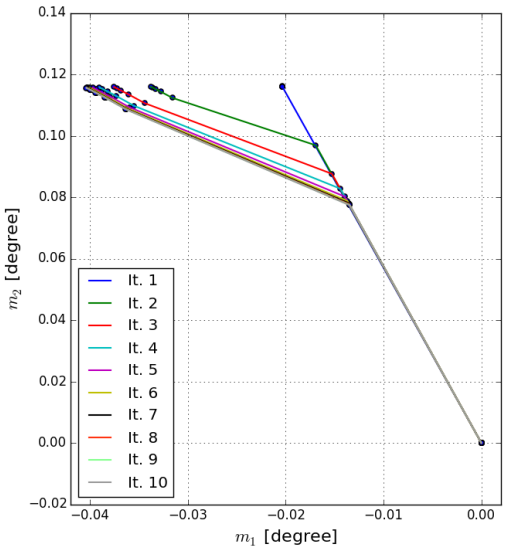

Figure 6.19: TPW triggered by the ICE-3G LGM minus present day ice history over 5 ka for 10 iterations for the four-layer Earth model. Black dots indicate the end of time steps. The pole position reaches the top left of the plot at 5 ka after hydrostatic equilibrium.

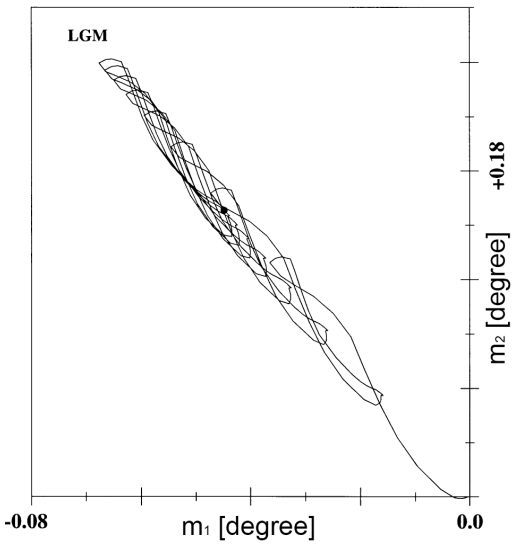

Figure 6.20: TPW triggered by ICE-3G over a period extending from the onset of glaciation, the origin of the plot, through 8 glacial cycli. The pole position reaches the top left portion of the plot at LGM, and the solid dot at present day. (Mitrovica et al., 2001)

In Figure 6.19 the first dot after the dot shown at zero TPW presents the TPW for 1 year after hydrostatic equilibrium, the elastic part of the viscoelastic response of TPW. The TPW direction for the elastic part of the response is different from the viscoelastic response. The elastic TPW response does not necessarily have to be in the same direction as the longer term viscoelastic response. The elastic response is affected by the Young's modulus of the material, whilst the viscoelastic response is more heavily affected by the viscosity of the material, specifically of the lower mantle. Again it can be seen that for each iteration the TPW converges too one value for m_1 and m_2. This problem will be addressed in the last Test 9.

In Appendix B.2 is shown that the determination of the change in moment of inertia of distributed mass itself $\Delta\mathbf{I}_L$ for a coarse 0.7° grid of the ICE-3G input surface load only causes a 0.001% error. Thus, $\Delta\mathbf{I}_L$ is determined with sufficient accuracy for the distributed mass.

For the direction of TPW the numerical results for the viscoelastic TPW response can be compared to Figure 6.20 (Mitrovica et al., 2001). Both TPW predictions move in negative m_1 direction and positive m_2 direction. The slope of TPW from the numerical results is ~-0.34° in m_1 direction for 1° in m_2 direction, and from the analytical results from Mitrovica et al. (2001) ~-0.28° in m_1 direction for 1° in m_2 direction. These slopes show good agreement. Mitrovica et al. (2001) includes a sea load as well, which can cause a difference in TPW direction, since the ocean is not uniformly distributed. Furthermore, the properties of the four-layer Earth model are based on information found in Mitrovica et al. (2001), but not all radii, densities, rigidities, and viscosities of the four layers are mentioned. Therefore, the used four-layer model as presented in Table 6.2 likely deviates from the Earth model used in Mitrovica et al. (2001).

6.3.2. Test 7: TPW accuracy to moment of inertia around the principal axes

The change in moment of inertia around the principal axes is investigated as possible cause for the numerical TPW solution deviating from the analytical solution. The accuracy of the change in moment of inertia at hydrostatic equilibrium, investigated in Test 5, may have an effect on TPW. This test investigates the effect of the moments of inertia around the principal axes, A, B, and C, and of the moment of inertia of the unperturbed spherical body I_0 on TPW. Again, $\Delta\mathbf{I}_{D,L}$ is not taken into account, but $\Delta\mathbf{I}_L$ is for the determination of TPW and $\sigma_{l,m}$ for the determination of the perturbed gravitational potential. After 10 Ma, a constant $2{\cdot}10^{19}$ kg point mass is applied at 0° longitude and 45° colatitude. Four tests are performed to study the effect of A, B, and C on TPW. The dimensionless quantities m_i with i = 1,2,3 of the perturbed rotational vector are investigated. The same test set-up as described in the previous Test 6 is used. The following four tests are performed:

- 7-1: $\Delta A(t)$, $\Delta B(t)$, and $\Delta C(t)$ from the simulation results $\Delta\mathbf{I}_{D,c}(t)$ and I_0 from Hu et al. (2017b).
- 7-2: ΔA, ΔB, and ΔC from the simulation results $\Delta\mathbf{I}_{D,c}$ when the body is in hydrostatic equilibrium at 10 Ma, and I_0 from Hu et al. (2017b). ΔA, ΔB, and ΔC thus remain constant.
- 7-3: ΔA, ΔB, and ΔC from the analytical approach when the body is in hydrostatic equilibrium at 10 Ma, and I_0 from Hu et al. (2017b). ΔA, ΔB, and ΔC thus remain constant.
- 7-4: ΔA, ΔB, and ΔC from the analytical approach when the body is in hydrostatic equilibrium at 10 Ma, and I_0 from the analytical approach. ΔA, ΔB, and ΔC thus remain constant.

I_0 from the approach of Hu et al. (2017b) is used such that it can be compared to the TPW path from this analytical approach. The moment of inertia of the unperturbed spherical body for laterally homogeneous models can analytically be determined according to:

$$I_0 = \frac{8\pi}{3}\rho_0\int_0^{R_0} r^4\,dr + \frac{8\pi}{3}\sum_{i=1}^{N}\rho_i\int_{R_{i-1}}^{R_i} r^4\,dr \tag{6.12}$$

in which the subscript denotes the layer, starting with 0 at the core up to the layer N. First, the TPW results will be compared to each other to see what the accuracies are. The I_0 used in Hu et al. (2017b) equals 7.2458e37 kg m^2 whilst the I_0 from the analytical approach for the two-layer Earth model equals 8.3858e37 kg m^2. Figure 6.21 presents the TPW triggered by a $2{\cdot}10^{19}$ kg point mass at 0° longitude and 45° colatitude over 5 ka for the four test cases. The mesh resolution is set to 500 km, $CETOL$ to 1e-4, and the maximum spherical harmonic degree to 45.

As one can see the TPW results for Test 7-1 and 7-2 are nearly equal to each other. The difference between the two solutions, shown in the upper right plot, is negligible. This indicates that the updating of the changes in moment of inertia around the principal axes through time does not have a significant effect on the TPW path magnitude and direction. Glaciation-induced polar wander on Earth results in small angle TPW. Thus, the changes in moment of inertia around the principal axes do not drastically change through time. Note that for large angle polar wander the changes in moment of inertia around the principal axes will be larger. This may results in significant differences in TPW path, with a result that the changes in moment of inertia around the principal axes do need to be updated through time.

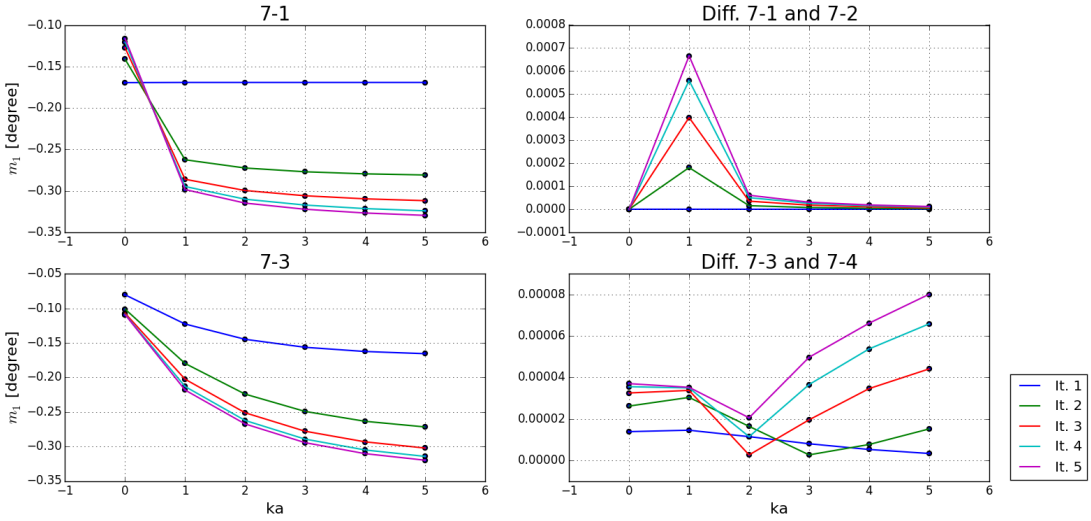

Figure 6.21: TPW triggered by a $2{\cdot}10^{19}$ kg point mass at 0° longitude and 45° colatitude over 5 ka for 5 iterations for the four test cases.

The results for Test 7-3 and 7-4 are also nearly equal to each other. The difference between the two solutions, shown in the lower right plot, is negligible. This indicates that the background spherical model through the moment of inertia of the unperturbed body does not have a significant effect on TPW. From Equation 6.11 can be seen that I_0 cancels out for m_1 and m_2, and that it only has an effect on m_3, the change in length-of-day (LOD), or rotational rate. The perturbations in the rotational vector in the local frame are converted to the rotational vector in the initial local frame. The new local coordinate systems for the next iteration are based on the rotational vector. Apparently a different I_0, ~7.25e37 or ~8.40e37 kg m^2, does not have a significant effect on TPW through the change in LOD or new local coordinate system definitions for the next iteration, while I_0 is ~100 times larger than ΔC. This may indicate that the change in rotational rate does not have a large effect on the TPW path. This is confirmed in Appendix E.1, in which the effect of the rotational rate in the centrifugal potential definition is investigated.

The difference in TPW paths between 7-1 and 7-3 are a result of the differences in ΔA, ΔB, and ΔC which propagate to the rotational vector $\boldsymbol{\omega}$. The different TPW paths can be a result of the direct effect in $\boldsymbol{\omega}$, from which the new local coordinate systems are defined, or of the change in magnitude of the centrifugal potential through Ω. The change in magnitude of the centrifugal potential through Ω expresses itself in the radial displacements of the nodes. Therefore, $\Delta\mathbf{I}_{D,c}$ changes, which is used in the polar wander Equation 6.11. In Appendix E.1 is shown that for the point mass the change in rotational rate only results in a 0.2% change in the TPW path. Thus, the difference in TPW paths between 7-1 and 7-3 are mainly a result of the differences in ΔA, ΔB, and ΔC propagating to m_1 and m_2.

The choice for changes in moment of inertia around the principal axes, from the simulation results $\Delta\mathbf{I}_{D,c}(t)$ or from the analytical approach, does have a significant effect on TPW. As shown earlier in Test 5 there is a 2% difference in the ΔA, ΔB, and ΔC from the simulation at 10 Ma, when the model is in hydrostatic equilibrium, and from the analytical approach for a 400 km mesh resolution. The rotational vector $\boldsymbol{\omega}(t)$ defines the new local coordinate system for each time step used in the next iteration. Figure 6.22 and 6.23 present the unit vector elements of the x-axis in the initial local frame for each time step and for 5 iterations for test 7-1 and test 7-3, respectively.

As shown, the difference in ΔA, ΔB, and ΔC propagates to $\boldsymbol{\omega}$ which in their turn propagates to the local coordinate system definition, to which the centrifugal potential is applied. The choice of ΔA, ΔB, and ΔC, from the simulation results $\Delta\mathbf{I}_{D,c}(t)$ or from the analytical approach, is thus of importance for the TPW path. No conclusions can be drawn on which approach is better, since the numerically determined TPW cannot yet be verified with analytical TPW results. Components of the code need to be isolated to be able to identify why the numerical TPW results are not conform the analytical results. As mentioned earlier, a large contributor to this mismatch will be discussed in Test 9.

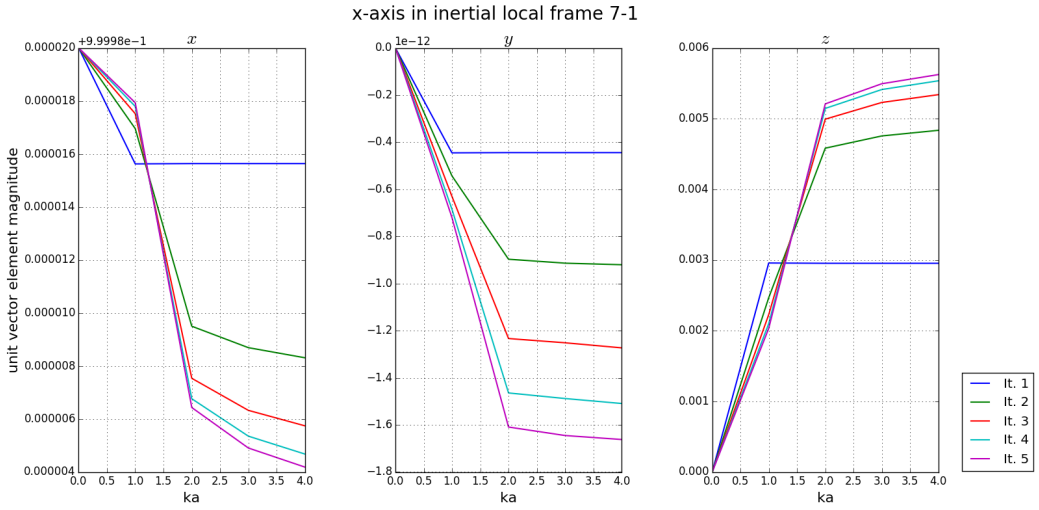

Figure 6.22: The unit vector elements of the x-axis in the initial local frame for each time step and for 5 iterations for test 7-1.

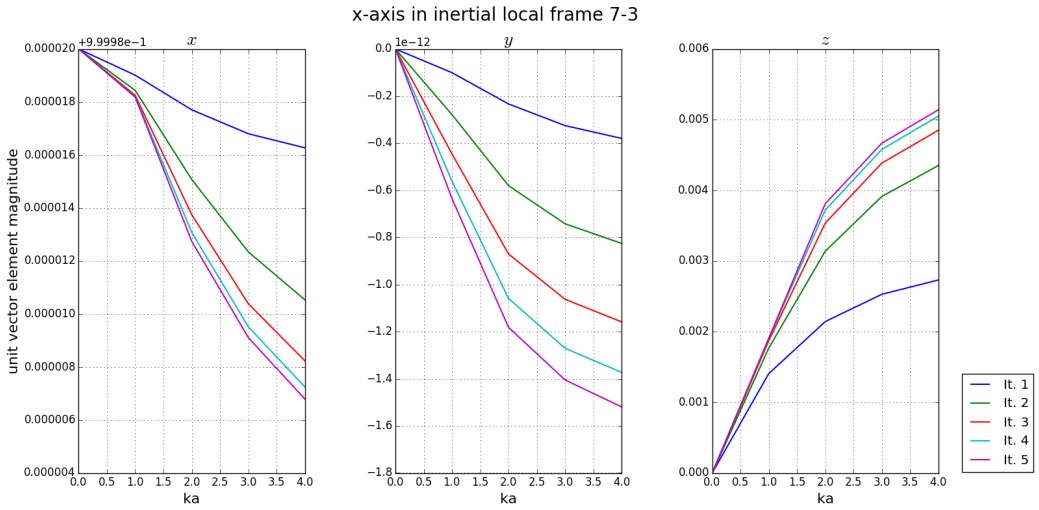

Figure 6.23: The unit vector elements of the x-axis in the initial local frame for each time step and for 5 iterations for test 7-3.

6.3.3. Test 8: TPW accuracy to time step size

In this test the accuracy of TPW to the size of the time steps is investigated. When time steps are taken too large the predicted TPW at the end of the simulation at t_{end} might be different from when smaller time steps are used. When a surface load is applied when the model is in hydrostatic equilibrium this load will trigger TPW. The centrifugal potential is then applied to the new position of the rotational axis. Together with the equatorial bulge readjustment the load will move towards the equator. However, one can imagine if the time steps are too large the TPW prediction at t_{end} deviates from what is expected because no sufficient updates are applied of the centrifugal potential on new positions of the rotational axis between the start and the end of the simulation. Figure 6.24 presents a visualization of TPW triggered by a point mass for two different choices of time step size. In the upper blue sequence 2 time steps are taken and in the lower green sequence only 1 to reach t_3. With more time steps the centrifugal potential is updated more regularly. This may cause a different TPW prediction than when less time steps are taken as shown at t_3 in Figure 6.24.

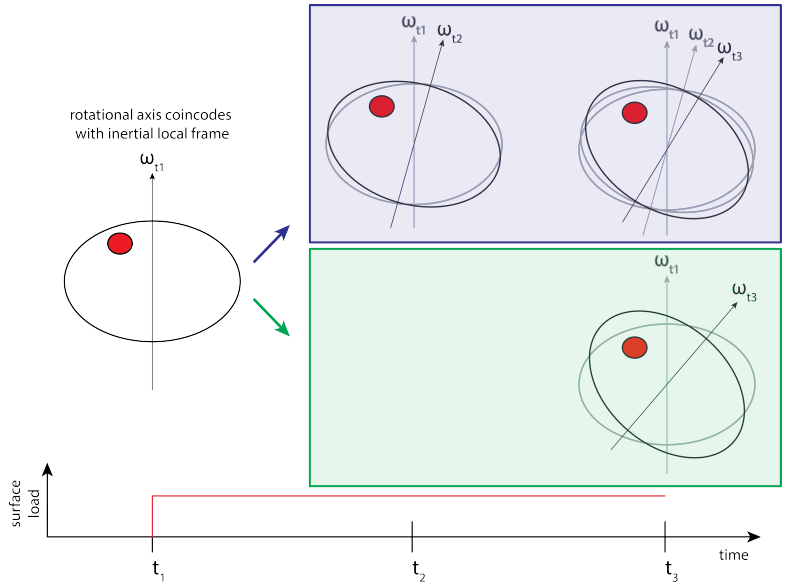

Figure 6.24: Visualization of TPW triggered by point mass for different time step sizes.

Figure 6.25 presents the TPW triggered by a $2{\cdot}10^{19}$ kg point mass at 0° longitude and 45° colatitude over 5 ka after 5 iterations for 0.25 ka time steps, 0.5 ka time steps, and 1.0 ka time steps.

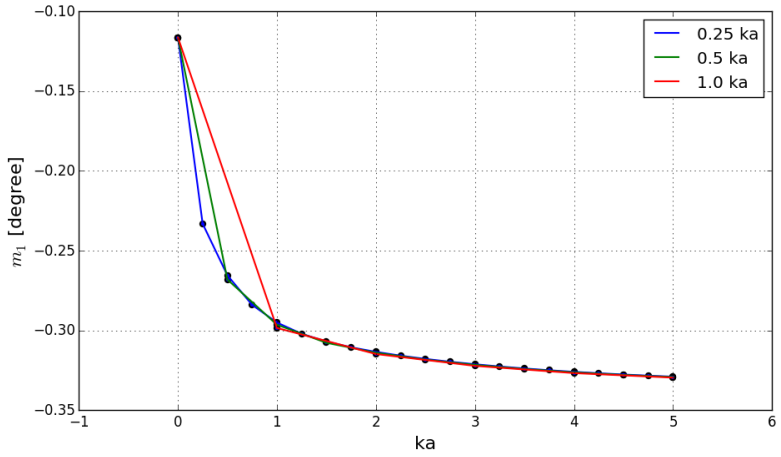

Figure 6.25: TPW triggered by a $2{\cdot}10^{19}$ kg point mass at 0° longitude and 45° colatitude over 5 ka after 5 iterations for 0.25 ka time steps, 0.5 ka time steps, and 1.0 ka time steps.

The TPW solution for 0.25 ka is smoother than the other two solution because more time steps are taken, allowing for more gradual changes. Again the TPW converges to a value of ~0.33° which is not expected for the constant load without deformations from the load taken into account. However, also visible is that at 0.5 ka after equilibrium the TPW prediction with 0.5 ka time steps is 1.0% larger than with 0.25 ka time steps. At 1.0 ka after equilibrium the TPW prediction with 0.5 ka time steps is 0.5% larger than with 0.25 ka time steps, and the TPW prediction with 1.0 ka time steps is 1.2% larger than with 0.25 ka time steps. This shows the effect the time step size can have on TPW, as the errors propagate through time. This error propagation is not clearly visible in this test because the TPW solution wrongly converges to a value of ~0.33°. However, it is of importance to find an optimum time step size for which the solution does not significantly change when taking a smaller time step size. The TPW accuracy to the time step size in the numerical simulation has been shown, but this effect still does not explain the difference in numerical and analytical results.

6.3.4. Test 9: simultaneous iteration of the centrifugal and gravitational potential

Test 6 showed that for the constant point mass the TPW from the numerical model does not correspond to the analytical solution of Hu et al. (2017b) or Wu and Peltier (1984). The stress in the body is a function of the radial displacements and the perturbed gravitational potential. From the solution to the Laplace equation follows that the perturbed gravitational potential is a function of the radial displacements. Therefore, iterations are required to solve for the radial displacements in the body (Wu, 2004). There iterations occur for all time steps simultaneously. Next to surface loading, a centrifugal potential can also be applied to model a rotating body (Wu and Wang, 2006). The surface loading affects the rotational state of the body, through a change in the rotational axis position with respect to the surface and through a change in the rotational rate. When this coupling of surface load and rotational state is taken into account, iterations are also required for the centrifugal potential. The existing numerical model within the research group is based on the simultaneous iteration over all time steps for the perturbed gravitational potential and radial displacements (Wu, 2004). Since this model is expanded with the coupling between surface load and rotational state, the iterations for the centrifugal potential and perturbed gravitational potential also occur simultaneously for all time steps.

One can imagine that when over the first time step of 10 Ma the body has not reached its equilibrium yet for a low number of iterations that this may affect the perturbed gravitational potential in the following time steps. Thus, the perturbed gravitational potential may be wrongly estimated based on the centrifugal potential that has not fully converged yet. More importantly, when TPW takes place in the time steps after the first 10 Ma time step, the centrifugal potential changes based on the new position of the rotational axis, and this also affects the perturbed gravitational potential for the following time steps.

To investigate whether the centrifugal potential and perturbed gravitational potential can be iterated for simultaneously over all time steps the following tests are proposed. The TPW path will be investigated for when the perturbed gravitational potential is fully converged before continuing to the next time step. In order to do this using the numerical model, several simulations are required. The converged gravitational potential of the first time step of the first simulation is used as force input for the second simulation. Then, the converged gravitational potential of the first and second time step of the second simulation is used as force input for the third simulation, and so on until the last time step. The time array starting at zero and defining the end of the time steps is as follows: [10000.0, 10000.001, 10001.0, 10002.0, 10003.0, 10004.0, 10005.0] ka, as in the previous tests. The first time step takes 10 Ma and is determined in Test 4 and 5 for the body in hydrostatic equilibrium. The second step is only 1 year such that the elastic response of TPW from the surface load can be determined. The following step are all 1 ka until 5 ka after hydrostatic equilibrium. A constant $2{\cdot}10^{19}$ kg point mass is applied at 45° colatitude and 0° longitude from 10 Ma onwards. The deformation due to the surface load is not taken into account. One test is the reference test and is performed according to the TPW algorithm described in Chapter 5, as the previous tests. Then the following test are performed:

1. 9-1: the converged solution of the perturbed gravitational potential ϕ_1 for each layer of time step 1 of the reference test is used as load input for time step 1 at the start of the simulation.
2. 9-2: the converged solution of the perturbed gravitational potential ϕ_1 for each layer of time step 1 and 2 of Test 9-1 are used as load input for time step 1 and 2 at the start of the simulation.
3. 9-3: the converged solution of the perturbed gravitational potential ϕ_1 for each layer of time step 1, 2, and 3 of Test 9-2 are used as load input for time step 1, 2, and 3 at the start of the simulation.
4. 9-4: the converged solution of the perturbed gravitational potential ϕ_1 for each layer of time step 1, 2, 3, and 4 of Test 9-3 are used as load input for time step 1, 2, 3, and 4 at the start of the simulation.
5. 9-5: the converged solution of the perturbed gravitational potential ϕ_1 for each layer of time step 1, 2, 3, 4, and 5 of Test 9-4 are used as load input for time step 1, 2, 3, 4, and 5 at the start of the simulation.
6. 9-6: the converged solution of the perturbed gravitational potential ϕ_1 for each layer of time step 1, 2, 3, 4, 5, and 6 of Test 9-5 are used as load input for time step 1, 2, 3, 4, 5, and 6 at the start of the simulation.

In these tests it is ensured that the perturbed gravitational potential in and before step i is fully converged before continuing to the next time step $i+1$. Thus, the iterations are performed per time step until convergence is reached before continuing to the next time step. When the TPW paths from these tests correspond to the TPW path of the reference test, in which the iterations for the centrifugal potential and perturbed gravitational potential occur simultaneously over all time steps, the simultaneous iteration procedure is not the cause for the difference in TPW paths between the numerical and analytical approaches (Hu et al., 2017b; Wu and Peltier, 1984). Figure 6.26 presents the TPW paths of the reference test and the 6 tests described above for a $2{\cdot}10^{19}$ kg point mass at 0° longitude and 45° colatitude over 5 ka after 12 iterations.

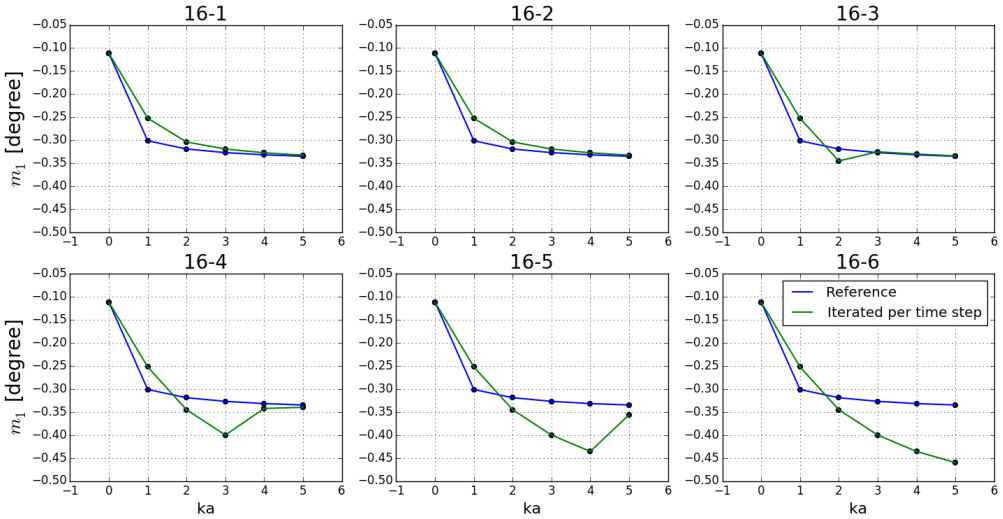

Figure 6.26: TPW triggered by a $2{\cdot}10^{19}$ kg point mass at 0° longitude and 45° colatitude over 5 ka after 12 iterations for the reference test and the 6 tests in which the iterations do not occur for all time steps simultaneously for the centrifugal and perturbed gravitational potential.

The TPW paths differ for the reference test and the tests described above. For Test 9-1 the converged perturbed gravitational potential of the first time step, from 0 to 10 Ma, is used as load input before the start of the simulation. In the first iteration of Test 9-1 the body has thus already reached hydrostatic equilibrium. The body not having reached its equilibrium position yet will therefore not affect the perturbed gravitational potential in the following time steps. The TPW path using this approach differs from the reference test TPW path, indicating that the not yet converged perturbed gravitational potential affects TPW predictions in future time steps. For Test 9-2 the converged perturbed gravitational potential of the first and second time step are used as load input before the start of the simulation. Since at the start of the first and second time step the rotational axis still coincides with the z-axis of the initial local reference frame, no TPW has taken place, the TPW path predictions of Test 9-1 and Test 9-2 are equal to each other. However, at the start of the third time step at 1 year after 10 Ma the rotational axis has moved. For Test 9-3 for which also the perturbed gravitational potential for time step 3 of Test 9-2 is used as load input before the simulation, the TPW differs from the ones predicted in Test 9-1 and Test 9-2. Test 9-4 to 9-6 then show that the TPW path predictions up to the time step for which the fully converged solution is used from the previous tests, differ from the reference test.

Now it is of interest to see how the TPW path from Test 9-6, in which up to 5 ka the iterations are not performed simultaneously for the centrifugal potential and the perturbed gravitational potential over all time steps, compares to the analytical TPW solution of Hu et al. (2017b). Figure 6.27 presents the TPW paths from the analytical approach of Hu et al. (2017b) and the numerical approach from Test 9-6, and the reference test in which the iterations occur over all time steps simultaneously. As shown the TPW paths from Test 9-6 and the analytical methods do not correspond. But by performing the iterations per time step in Test 9-6 the TPW path does come closer to the analytical solution than for iterating over all time steps simultaneously in the reference test. Also, using this approach, the TPW solution does not converge to a constant value as fast as the reference approach. The TPW cannot be determined using the algorithm in which the centrifugal potential and the perturbed gravitational potential are iterated for simultaneously over all time steps. One needs to iterate per time step before continuing to the next step.

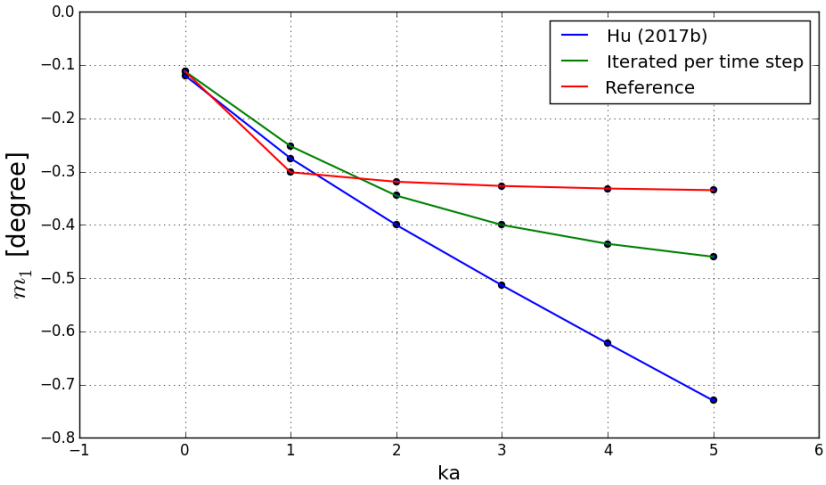

Figure 6.27: TPW triggered by a $2{\cdot}10^{19}$ kg point mass at 0° longitude and 45° colatitude over 5 ka after 12 iterations for the analytical approach from Hu et al. (2017b), and Test 9-6 and the reference test in which the iterations do and do not occur for all time steps simultaneously, respectively, for the centrifugal potential and the perturbed gravitational potential.

For the TPW results from the numerical model the problem lies in that the change in moment of inertia from the deformations of the body converges to a constant value whilst it should keep changing. However, it is hard to find where this problem starts since TPW, the position of the rotational axis, the centrifugal force applied to the rotational axis, and the change in moment of inertia from the deformations due to the centrifugal force are all closely linked, and affect each other in the coming time steps. In Test 9 is found that the centrifugal potential and the perturbed gravitational potential cannot be iterated for simultaneously over all time steps. The iterations need to occur per time step. Since the model within the research group, which is expanded with TPW, is build in such a way that the iterations occur for all time steps simultaneously, the model needs to be rebuild for the application of TPW. With an adjusted model which can iterate per time step, it would much improve the ability to perform research on the implementation of the TPW algorithm in the numerical model. However, one unavoidable consequence of iterating per time step is that the simulation time will increase by a factor of the number of time steps compared to how the model is currently build up.

7

Conclusion

In this chapter the answers to the research question and its subquestions are provided and conclusions are drawn based on the results of the research. The subquestions will be discussed one by one in consecutive order as presented in the Introduction.

What is the accuracy of the numerical model for the response to a forced movement of the rotational axis?
Before coupling a surface load to the Earth's rotational behavior, it is important to understand how the numerical model behaves for the two cases separately. Therefore, the solution for the change in moment of inertia from the numerical model for a forced movement of the rotational axis, in which a surface load is not introduced, is compared to analytical solutions for laterally homogeneous Earth models. For the case with purely a forced movement of the rotational axis the numerical solution of the change in moment of inertia shows good agreement with the analytical solution with a 1% or 1e32 kg m^2 error in the theoretically non-zero components, the diagonal components, of the inertia tensor.

However, for the numerical solution the theoretically zero components, the off-diagonal components, of the inertia tensor are not zero but 4 orders of magnitude smaller than the other components, in the order of 1e30 kg m^2. This is a numerical error as a result of the discretization and numerical integration in FEM. True polar wander is a function of the ΔI_{13}, ΔI_{23}, and ΔI_{33} components of the inertia tensor. The numerical errors in these components need to be taken into consideration for the effect on TPW. Also shown is that for accurate change in moment of inertia estimates a fine time array should be used in the numerical simulation at times with large gradients in the change in moment of inertia.

What is the accuracy of the numerical model for the response to surface loading?
The solution for the change in moment of inertia from the numerical model for a surface load, in which rotation is not introduced, is compared to analytical solutions for laterally homogeneous Earth models. For the case with purely a surface load the numerical solution of the change in moment of inertia is very sensitive to the mesh resolution. A 200 km mesh resolution shows the best resemblance with the analytical solution with little improvement for a higher resolution than 200 km. However, there is a 4% or 5e30 kg m^{-2} error between the numerical and analytical solutions. This error could be due to the use of incompressible materials causing a phenomenon called pressure checkerboarding or due to the interpolation of the pressure loads in the FEM application suite. Pressure checkerboarding is the effect of large oscillating hydrostatic stresses interacting with the displacements and is most likely to occur for hydrostatic stresses in nearly incompressible materials in confined elements in regular meshes. When including the deformation due to the surface load in TPW this error needs to be taken into consideration as well.

The largest radial displacements from a realistic ice history, a constant ICE-3G at LGM minus present day load for 90 ka before linearly decreasing to zero load over 10 ka, deviate by 2% after 90 ka and by 9% after 100 ka for a 400 km mesh resolution. This difference can partly be overcome by using a higher mesh resolution, as concluded before, and potentially by decreasing the time increment size to decrease the strain error in the numerical integration.

What is the accuracy of the numerical model for the Earth in hydrostatic equilibrium?
To be able to study the Earth's rotational behavior induced by surface loads, the model needs to be in hydrostatic equilibrium. The centrifugal potential needs to be applied for a long enough time to the initial local frame such that the model is flattened and does not change shape anymore after that time, or within certain boundaries, under the centrifugal forcing. It is found that the time for the model to have reached hydrostatic equilibrium is dependent on the Earth model properties regarding relaxation, which are the viscosity and the radius of the layers. The analytical fluid Love number can be approached for 98.4% for the two-layer Earth model for a 400 km mesh resolution. For when a realistic ice history is implemented of 8 ice cycli of 100 ka each, the degree 2 tidal Love number changes by less than 0.001% after 10 Ma, and thus this Earth model is considered to have reached hydrostatic equilibrium after 10 Ma.

Another measure for the flattening of the Earth is the change in moment of inertia. The analytical solution for the change in moment of inertia around the principal axes is better approached with a higher mesh resolution. The error in the diagonal components of the inertia tensor at equilibrium decreases by half from a mesh resolution of 400 km to 300 km, and is 1%. The off-diagonal components, which should be zero, are in the order of 1e30-1e31 kg m^2, which is a numerical error as mentioned before. For a 0.8 Ma glaciation history the diagonal components change by about 1e28 kg m^2 and the off-diagonal components by about 1e26 kg m^2 over this time period, which is negligible compared to the numerical error of 1e32 kg m^2 and 1e30 kg m^2, respectively, at equilibrium. However, it is not known how the numerical error propagates through time when the position of the rotational axis changes. From the degree 2 tidal Love number and the change in moment of inertia is concluded that the model has reached hydrostatic equilibrium after 10 Ma, because the 2 parameters change a negligible amount compared to the numerical errors over the next 0.8 Ma, representing the glaciation history. Also, It is found that one time step can be used up to hydrostatic equilibrium, which results in a faster computation due to less evaluations of the nodal displacements.

What is the accuracy of the numerical model for true polar wander?
A $2{\cdot}10^{19}$ kg point mass is considered in the x-z plane at 45° colatitude. The change in moment of inertia from the deformation of the surface load $\Delta\mathbf{I}_{D,L}$ is not taken into account. Only the changes in moment of inertia from the direct effect of the surface load $\Delta\mathbf{I}_L$ and from deformations due to the centrifugal force $\Delta\mathbf{I}_{D,c}$ are considered. The TPW direction for the point mass in the x-z plane can be fully described by m_1, which is a function of ΔI_{13}. The movement of the rotational axis in the m_2 direction is 3 orders of magnitude smaller than the movement in the m_1 direction and comes from the approximation of the point mass on a grid, and from numerical errors in the $\Delta I_{D,23}$ component when the model is in hydrostatic equilibrium. However, the numerical TPW magnitude is not conform the analytical solution, as it converges too fast to a value of -0.33°. For a constant point mass for an Earth model without a high viscosity lithosphere, TPW should continue until the point mass has reached the equator. Possible causes for this mismatch need to be identified by isolating parts of the code for testing purposes.

The elastic part of the viscoelastic response to the surface load is captured 1 year after the application of the surface load at hydrostatic equilibrium. Here, the elastic part of the TPW response is discussed. ΔI_{13} is used in the TPW determination for m_1. ΔI_{13} is a summation of the change in moment of inertia from the surface load itself $\Delta I_{L,13}$ and from the deformations of the model $\Delta I_{D,13}$. 1 year after equilibrium, $\Delta I_{L,13}$ and $\Delta I_{D,13}$ make up 74% and 26% of the total ΔI_{13}, respectively. For the model with a 500 km mesh resolution the numerical error at hydrostatic equilibrium in $\Delta I_{D,13}$ contributes for 2% to the TPW prediction. The analytical TPW solution for the elastic part of the response is -0.1197° in the m_1 direction whilst the numerical solution is -0.1120°, and can be improved to -0.1125° for a 200 km mesh resolution, deviating by 6% from the analytical solution. The numerical error of 2% cannot fully explain the 6% difference between the numerical and analytical solution. However, it is not known how the numerical error propagates through time when the position of the rotational axis changes. The remaining 4% difference in m_1 at 1 year after equilibrium cannot come from an error in the determination of the change in moment of inertia from the surface load itself $\Delta\mathbf{I}_L$. $\Delta\mathbf{I}_L$ introduces a 0.5% error for a coarse 2° grid of the input surface load.

Here a constant ICE-3G LGM minus present-day load is considered to investigate the TPW direction for realistic ice surface loads. Again, the change in moment of inertia from the deformation of the surface load $\Delta\mathbf{I}_{D,L}$ is not taken into account. The slope of the TPW from the numerical results is -0.34° in m_1 direction for 1° in m_2 direction, and from the analytical results -0.28° in m_1 direction for 1° in m_2 direction. The slopes show good agreement. The change in moment of inertia from the surface load itself $\Delta\mathbf{I}_L$ for the distributed mass only introduces a ~0.001% error. Differences can come from that the analytical approach includes a sea load and from the different properties, such as layer radii, density, rigidity, and viscosity, of the four-layer Earth model used in the numerical and analytical approaches.

Here, the TPW path is considered from the viscoelastic response of the model to the point mass. Important to emphasize is that the change in the rotational rate from the change in length-of-day (LOD), determined from the norm of the perturbed rotational vector elements in the local frame, is a crucial step for the TPW solution to converge in terms of number of iterations for the radial displacement solution in the FE analysis. The new rotational vector needs to be normalized using the new rotational rate. This should not be confused with the rotational rate update in the definition of the centrifugal potential which feeds back into the numerical analysis. This rotational rate update only causes a 0.2% difference in TPW when not included.

The accuracy of the change in moment of inertia around the principal axes, ΔA, ΔB, and ΔC, at hydrostatic equilibrium is investigated as possible cause for the numerical TPW solution deviating from the analytical solution. The updating of the change in moment of inertia around the principal axes through time does not have a significant effect on TPW for small angle TPW. However, a 2% difference in the change in moment of inertia around the principal axes between the analytical solution and the numerical solution for a 400 km mesh resolution does have a large effect on the TPW path, by affecting m_1 and m_3. The changes in these inertia tensor components are small due to small angle polar wander. The definition of the new local coordinate systems for each time step is a function of m_1, whilst the centrifugal potential is a function of m_3 through the update of the rotational rate. The different path is mainly a result of the direct effect of ΔA, ΔB, and ΔC in the rotational vector which is used to define the local coordinate system. It is shown that the different path can only marginally be attributed to the change in magnitude of the centrifugal potential through the rotational rate. It is important to have an accurate hydrostatic equilibrium of the body since the error in the change in moment of inertia affects the TPW path through the local coordinate system definition for each time step.

Furthermore, it is shown that the time step size in the numerical simulation has a significant effect on TPW. It is of importance to find an optimum time step size for which the solution does not significantly change when taking a smaller time step size. The TPW accuracy to the time step size still does not explain why in the numerical model the rotational axis does not keep moving for a constant surface load.

The existing numerical model within the research group is based on the simultaneous iteration over all time steps for the perturbed gravitational potential and radial displacements. Since this model is expanded with the coupling between surface load and rotational state, the iterations for the centrifugal potential and perturbed gravitational potential also occur simultaneously for all time steps. One can imagine that when in the spin-up phase, from non-rotating to rotating body, the body has not reached equilibrium yet for a low number of iterations, this may affect the perturbed gravitational potential in the following time steps. The perturbed gravitational potential may be wrongly estimated based on the centrifugal potential which has not fully converged yet. Furthermore, when TPW takes place after the first time step, the centrifugal potential changes based on the new position of the rotational axis, and this also affects the perturbed gravitational potential for the following time steps.

It is found that when it is ensured that the perturbed gravitational potential in and before a step is fully converged before continuing to the next time step, the TPW path is different from what is found in the original approach and more closely resembles the analytical TPW solution. Also, using this approach, the TPW solution does not converge to a constant value as fast as the reference approach in which the iteration occurs simultaneously over all time steps. Therefore, the TPW cannot be determined using the algorithm in which the centrifugal potential and the perturbed gravitational potential are iterated for simultaneously over all time steps. One needs to iterate per time step. One unavoidable consequence of iterating per time step is that the simulation time will increase by a factor of the number of time steps compared to how the model is currently build up.

The subquestions help to answer the research questions which is there to accomplish the research objective. The research question is repeated here:

How to implement true polar wander in a numerical model based on the finite element method?

Multiple factors affect the TPW prediction: the accuracy of the change in moment of inertia for a movement of the rotational axis and for a surface load, the accuracy of the changes in moment of inertia at hydrostatic equilibrium, and the accuracy to the time step size in the simulation.

The numerical model could not be verified due to the following reason. For the TPW results from the numerical model the problem lies in the converging of the change in moment of inertia from the deformations of the body to a constant value whilst it should keep changing for a constant surface load. However, it is hard to find where this problem starts since the position of the rotational axis, the centrifugal force applied to the rotational axis, and the change in moment of inertia from the deformations are all closely linked, and affect each other in the coming time steps. The simultaneous iteration of the centrifugal potential and the perturbed gravitation potential has shown to be most problematic for the code verification. It is shown that the iterations for the perturbed gravitational potential and centrifugal potential need to occur per time step. The existing model withing the research group is based on the simultaneous iteration over all time steps for the perturbed gravitational potential and radial displacements. The recommendations regarding the TPW implementation in the numerical model based on these findings are presented in the next chapter.

8

Recommendations

This chapter discusses recommendations for further research on true polar wander using numerical modeling. The recommendations are ranked from highest to lowest priority.

From the conclusion that the centrifugal potential and perturbed gravitational potential cannot be iterated simultaneously over all time steps follows that the model needs to be rebuild for the application of TPW such that iterations are performed per time step before continuing to the next time step. It is not known whether the approach with iterations occurring per time step will result in a correct determination of the changes in moment of inertia, because the position of the rotational axis, the centrifugal force applied to the rotational axis, and the change in moment of inertia from the deformations are all closely linked. But the approach with iterations occurring per time step will much improve the ability to perform further research on the implementation of TPW in a numerical model. One unavoidable consequence of iterating per time step is that the simulation time will increase by a factor of the number of time steps compared to how the model is currently build up. However, the numerical model is valuable for research on TPW, including deformations due to surface loads, including lateral viscosity variations of the Earth model, and for large angle TPW incorporating non-stationary loads. Accurate glaciation-induced TPW predictions can provide a realistic range for the spherical harmonic coefficients $C_{2,1}$ and $C_{2,-1}$ and thereby improve the consistency of GIA models, which are of importance for climate change studies.

The accuracy tests as performed in this research should be repeated to find whether the same conclusions on the accuracies still hold and for code verification purposes. Once the TPW path is verified with an analytical method for homogeneous Earth models, one can continue with research on the effect of lateral viscosity variations on glaciation-induced true polar wander. The mesh elements need to be defined from the numerical model and the temperature data needs to be converted to diffusion and dislocation parameters for each element. From the diffusion and dislocation parameters the viscosity for each element is determined and coupled to the mesh elements in the numerical model. This procedure is already available within the research group and thus does not call for new code development. When different viscosities are assigned to the mesh elements, one can first investigate TPW triggered by a constant point mass to see whether the TPW deviates from the solution for the homogeneous model which closest resembles the laterally varying Earth model. By doing this, intermediate results, for an unrealistic ice load, on the effect of lateral viscosity variations on TPW can be found.

Subsequently, the deformation due to the surface load as well as multiple ice cycli can be taken into account. For this, the effect of the time step size on the TPW solution needs to be researched. The ice history for the last deglaciation period is more accurately known than for the previous ice cycli. The time step size for the earliest ice cycli perhaps could be taken larger than for more recent cycli such that the simulation time decreases. Also important for incorporating the deformation due to the surface load is the mesh resolution and the creep error tolerance, which effects on the TPW solution need to be further investigated. Furthermore, the potential effect of pressure checkerboarding on the radial displacements may be reduced by using an irregular mesh.

From these recommendations follows the capability of the numerical model for research on the effect of lateral viscosity variations on glaciation-induced rotational behavior of the Earth by using realistic Earth models with a lithosphere. For TPW on the Earth the numerical model can provide a range of $C_{2,1}$ and $C_{2,-1}$ corrections to be used in GIA models for the retrieval of accurate present-day surface mass changes.

Other recommendations with a lower priority are including an excess ellipticity and including a realistic ocean basin and sea level. The background oblateness of the Earth is a function of the hydrostatic equilibrium and of non-hydrostatic signals coming from long-term geophysical processes such as mantle convection and fossil rotational effects, causing an excess ellipticity which effect should be investigated (Mitrovica et al., 2005). The excess ellipticity can be included in the denominator of the expressions for the m_1 and m_2 components of TPW. For including a realistic ocean basin and sea level the elements of the code already exist but are not tested in conjunction with rotation, only with the Earth's deformation.

The model can also be expanded to TPW research on other planetary bodies. The approach is not restricted to small angle polar wander. For slowly rotating bodies the time derivative of the changes in moment of inertia cannot be ignored in the equations for the perturbed rotational vector elements.

Bibliography

G. A, J. Wahr, and S. Zhong. Earth to surface loading: an application to Glacial Isostatic Adjustment in Antarctica and Canada. *Geophys. J. Int.*, 192:557–572, 2013. doi: 10.1093/gji/ggs030.

Abaqus. `Abaqus` 6.14 scripting reference guide. `http://ivt-abaqusdoc.ivt.ntnu.no:2080/v6.14/books/ker/default.htm`, April 2014.

J. Arvo. Fast Random Rotational Matrices. In *Graph. Gems III*, chapter 4, pages 117–120. Academis Press Professional, Inc., Dan Dieog, California, 1992.

G. Cambiotti, Y. Ricard, and R. Sabadini. New insights into mantle convection true polar wander and rotational bulge readjustment. *Earth Planet. Sci. Lett.*, 310(3):538–543, 2011. doi: 10.1016/j.epsl.2011.08.009.

L. M. Cathles. *The Viscosity of the Earth's Mantle*. Princeton University Press, Princeton, NJ, 1975.

J. L. Chen, C. R. Wilson, J. C. Ries, and B. D. Tapley. Rapid ice melting drives Earth's pole to the east. *Geophys. Res. Lett.*, 40:2625–2630, 2013. doi: 10.1002/grl.50552.

S. R. Dickmann. Secular trend of the Earth's rotation pole: consideration of motion of the latitude observatories. *Geophys. J. Int.*, 51(1):229–244, 1977. doi: 10.1111/j.1365-246X.1977.tb04198.x.

R. Direen. *SpherePy 0.0.9*. GNU General Public License v3 (GPLv3) (GPLv3), 2015.

W. E. Farrell. Deformation of the Earth's surface loads. *Rev. Geophys. Sp. Phys.*, 10(3):761–797, 1972. doi: 10.1029/RG010i003p00761.

P. Gasperini and R. Sabadini. Finite element modeling of lateral viscosity heterogeneities and post-glacial rebound. *Tectonophysics*, 179:141–149, 1990.

T. Gold. Instability of the Earth's axis of rotation. *Nature*, 175(4456):526–529, 1955. doi: 10.1038/175526a0.

W. A. Heiskanen and F. A. Vening Meinesz. *The Earth and Its Gravity Field*. McGraw-Hill Book Company Inc., New York, USA, 1958.

H. Hu. *Rotational Dynamics of Viscoelastic Planetary Bodies*. PhD thesis, Delft University of Technology, 2018.

H. Hu, W. Van der Wal, and L. L. A. Vermeersen. A numerical method for reorientation of rotating tidally deformed viscoelastic bodies. *J. Geophys. Res. Planets*, 122:228–248, 2017a. doi: 10.1002/2016JE005114.

H. Hu, W. van der Wal, and L. L. A. Vermeersen. A Full-Maxwell Approach for Large-Angle Polar Wander of Viscoelastic Bodies. *J. Geophys. Res. Planets*, 122(12):2745–2764, 2017b. doi: 10.1002/2017JE005365.

E. R. Ivins and T. S. James. Antarctic glacial isostatic adjustment: a new assessment. *Antarct. Sci.*, 17(4): 541–553, 2005. doi: 10.1017/S0954102005002968.

H. Jeffreys. *The Earth: Its Origin, History, and Physical Constitution*. Cambridge University Press, New York, USA, 1924.

G. Kaufmann, P. Wu, and D. Wolf. Some effects of lateral heterogeneities in the upper mantle on postglacial land uplift close to continental margins. *Geophys. J. Int.*, 128:175–187, 1997. doi: 10.1111/j.1365-246X.1997.tb04078.x.

G. Kaufmann, P. Wu, and G. Li. Glacial isostatic adjustment in Fennoscandia for a laterally heterogeneous earth. *Geophys. J. Int.*, 143:262–273, 2000. doi: 10.1046/j.1365-246x.2000.00247.x.

V. Klemann, P. Wu, and D. Wolf. Compressible viscoelasticity: stability of solutions for homogeneous plane-Earth models. *Geophys. J. Int.*, 153:569–585, 2003. doi: 10.1046/j.1365-246X.2003.01920.x.

K. Latychev, J. X. Mitrovica, J. Tromp, M. E. Tamisiea, D. Komatitsch, and C. C. Christara. Glacial isostatic adjustment on 3-D Earth models: a finite-volume formulation. *Geophys. J. Int.*, 161:421–444, 2005. doi: 10.1111/j.1365-246X.2005.02536.x.

Z. Martinec, V. Klemann, W. Van der Wal, R. E. M. Riva, G. Spada, Y. Sun, D. Melini, S. B. Kachuck, V. Barletta, K. Simon, and T. S. James. A benchmark study of numerical implementations of the sea level equation in GIA modelling. *Geophys. J. Int.*, 215:389–414, 2018. doi: 10.1093/gji/ggy280.

I. Matsuyama, F. Nimmo, and J. X. Mitrovica. Planetary Reorientation. *Annu. Rev. Earth Planet. Sci.*, 42(1): 605–634, 2014. doi: 10.1146/annurev-earth-060313-054724.

J. C. Maxwell. On the dynamical theory of gases. *Philos. Trans. R. Soc. London*, 157:49–88, 1867. doi: 10.1098/rstl.1867.0004.

G. A. Milne and J. X. Mitrovica. Postglacial sea-level change on a rotating Earth. *Geophys. J. Int.*, 133(1):1–19, 1998. doi: 10.1046/j.1365-246X.1998.1331455.x.

J. X. Mitrovica and W. R. Peltier. On Postglacial Geoid Subsidence Over the Equatorial Oceans. *J. Geodyn.*, 96: 53–71, 1991. doi: 0.1029/91JB01284.

J. X. Mitrovica, G. A. Milne, and J. L. Davis. Glacial isostatic adjustment on a rotating earth. *Geophys. J. Int.*, 147(3):562–578, 2001. doi: 10.1046/j.1365-246x.2001.01550.x.

J. X. Mitrovica, J. Wahr, I. Matsuyama, and A. Paulson. The rotational stability of an ice-age earth. *Geophys. J. Int.*, 161(2):491–506, 2005. doi: 10.1111/j.1365-246X.2005.02609.x.

W. H. Munk and G. J. F. MacDonald. *The Rotation of the Earth: A Geophysical Discussion.* Cambridge University Press, 1960. doi: 10.1017/S0016756800036578Pu.

S. M. Nakiboglu and K. Lambeck. Deglaciation effects on the rotation of the Earth. *Geophys. J. R. Astron. Soc.*, 62(1):49–58, 1980. doi: 10.1111/j.1365-246X.1980.tb04843.x.

A. Paulson. *Inference of the Earth's Mantle Viscosity from Post-glacial Rebound.* Dissertation, University of Colorado, 2006.

A. Paulson, S. Zhong, and J. Wahr. Inference of mantle viscosity from GRACE and relative sea level data. *Geophys. J. Int.*, 171(2):497–508, 2007. doi: 10.1111/j.1365-246X.2007.03556.x.

W. R. Peltier. The Impulse Response of a Maxwell Earth. *Review*, 12:649–669, 1974. doi: 10.1029/RG012i004p00649.

W. R. Peltier. Glacial-Isostatic Adjustment-II. The Inverse Problem. *Geophys. J. R. Astron. Soc.*, 46:669–705, 1976. doi: 10.1111/j.1365-246X.1976.tb01253.x.

W. R. Peltier. Global Glacial Isostasy and the Surface of the Ice-Age Earth: The ICE-5G (VM2) Model and GRACE. *Annu. Rev. Earth Planet. Sci.*, 32:111–149, 2004. doi: 10.1146/annurev.earth.32.082503.144359.

W. R. Peltier, D. F. Argus, and R. Drummond. Space geodesy constrains ice age terminal deglaciation: The global ICE-6G_C(VM5a) model. *J. Geophys. Res. Planets*, 120:450–487, 2015. doi: doi:10.1002/2014JB011176d.

A. Purcell, P. Tregoning, and A. Dehecq. An assessment of the ICE6G_C (VM5a) glacial isostatic adjustment model. *J. Geophys. Res. Solid Earth*, 121:3939–3950, 2016. doi: 10.1002/2015JB012742.

Y. Ricard, G. Spada, and R. Sabadini. Polar wandering of a dynamic earth. *Geophys. J. Int.*, 113(2):284–298, 1993. doi: 10.1111/j.1365-246X.1993.tb00888.x.

R. Sabadini and W. R. Peltier. Pleistocene deglaciation and the Earth's rotation: implications for mantle viscosity. *Geophys. J. R. Astron. Soc.*, 66(3):553–578, 1981. doi: 10.1111/j.1365-246X.1981.tb04890.x.

R. Sabadini, D. A. Yuen, and E. Boschi. Polar wandering and the forced responses of a rotating, multilayered, viscoelastic planet. *J. Geophys. Res.*, 87(B4):2885, 1982. doi: 10.1029/JB087iB04p02885.

R. Sabadini, L. L. A Vermeersen, and G. Cambiotti. *Global Dynamics of the Earth: Applications of Viscoelastic Relaxation Theory to Solid-Earth and Planetary Geophysics*. Springer, second edition, 2016. doi: 10.1017/CBO9781107415324.004.

G. Spada, Y. Ricard, and R. Sabadini. Excitation of true polar wander by subduction. *Nature*, 355:472–475, 1992. doi: 10.1038/355242a0.

G. Spada, R. Sabadini, and E. Boschi. Long-term rotation and mantle dynamics of the Earth, Mars, and Venus. *J. Geophys. Res.*, 101:2253–2266, 1996. doi: 10.1029/95JE03222.

J. Tromp and J. X. Mitrovica. Surface loading of a viscoelastic planet - III . Aspherical models. *Geophys. J. Int.*, 140:425–441, 2000. doi: 10.1046/j.1365-246x.2000.00027.x.

A.M. Tushingham and W. R. Peltier. ICE-3G: A new global model of Late Pleistocene deglaciation based upon geophysical predictions of post-glacial relative sea level change. *J. Geophys. Res. Solid Earth*, 96(B3):4497–4523, 1991. doi: 10.1029/90JB01583.

L. L. A. Vermeersen and J. X. Mitrovica. Gravitational stability of spherical self-gravitating relaxation models. *Geophys. J. Int.*, 142(2):351–360, 2000. doi: 10.1046/j.1365-246x.2000.00159.x.

L. L. A. Vermeersen and R. Sabadini. A new class of stratified viscoelastic models by analytical techniques. *Geophys. J. Int.*, 129:531–570, 1997. doi: 10.1111/j.1365-246X.1997.tb04492.x.

P. L. Whitehouse, M. J. Bentley, G. A. Milne, M. A. King, and I. D. Thomas. A new glacial isostatic adjustment model for Antarctica: calibrated and tested using observations of relative sea-level change and present-day uplift rates. *Geophys. J. Int.*, 190:1464–1482, 2012. doi: 10.1111/j.1365-246X.2012.05557.x.

R. J. Willemann. Reorientation of planets with elastic lithospheres. *Icarus*, 60(3):701–709, 1984. doi: 10.1016/0019-1035(84)90174-X.

P. Wu. Viscoelastic versus viscous deformation and the advection of pre-stress. *Geophys. J. Int.*, 108(1):35–51, 1992. doi: 10.1111/j.1365-246X.1992.tb00844.x.

P. Wu. Using commercial finite element packages for the study of earth deformations , sea levels and the state of stress. *Geophys. J. Int.*, 158:401–408, 2004. doi: 10.1111/j.1365-246X.2004.02338.x.

P. Wu and W. R. Peltier. Viscous gravitational relaxation. *Geophys. J. R. Astron. Soc.*, 70(2):435–485, 1982. doi: 10.1111/j.1365-246X.1982.tb04976.x.

P. Wu and W. R. Peltier. Pleistocene deglaciation and the Earth's rotation: a new analysis. *Geophys. J. R. Astron. Soc.*, 76(3):753–791, 1984. doi: 10.1111/j.1365-246X.1984.tb01920.x.

P. Wu and W. Van der Wal. Postglacial sealevels on a spherical, selfgravitating viscoelastic earth: Effects of lateral viscosity variations in the upper mantle on the inference of viscosity contrasts in the lower mantle. *Earth Planet. Sci. Lett.*, 211:57–68, 2003. doi: 10.1016/S0012-821X(03)00199-7.

P. Wu and H. Wang. Effects of mode coupling and location of rotational axis on glacial induced rotational deformation in a laterally heterogeneous viscoelastic earth. *Geophys. J. Int.*, 167:853–859, 2006. doi: 10.1111/j.1365-246X.2006.03103.x.

X. Wu, J. Ray, and T. van Dam. Geocenter motion and its geodetic and geophysical implications. *J. Geodyn.*, 58:44–61, 2012. doi: 10.1016/j.jog.2012.01.007.

S. Zhong, M. T. Zuber, L. Moresi, and M. Gurnis. Role of temperature-dependent viscosity and surface plates in spherical shell models of mantle convection. *J. Geophys. Res.*, 105:11063–11082, 2000. doi: 10.1029/2000JB900003.

S. Zhong, A. Paulson, and J. Wahr. Three-dimensional finite-element modelling of Earth's viscoelastic deformation: effects of lateral variations in lithospheric thickness. *Geophys. J. Int.*, 155:679–695, 2003. doi: 10.1046/j.1365-246X.2003.02084.x.

A

Appendix A

A.1. Number of time steps until hydrostatic equilibrium

In this test is investigated whether there is a difference in change in moment of inertia at 10 Ma, at hydrostatic equilibrium, when only one time step and when multiple time steps are used. Less time steps will result in a faster computation due to less evaluations of the nodal displacements. Note that with less time steps, thus larger time steps, the minimum increment time for the numerical integration has to be adjusted as they are defined as a fraction of the length of the time step, or the creep error tolerance needs to be increased. Table A.1 presents the change in moment of inertia for a simulation using multiple time steps (MS) and for a simulation using one time step (OS) for the two-layer Earth model for a 400 km mesh resolution after 12 iterations. The solutions for the multiple step approach come from the simulation also used in Test 4 and Test 5, thus with the time array [0.0001, 1.0, 5.0, 10.0, 50.0, 100.0, 500.0, 1000.0, 5000.0, 10000.0] ka until 10 Ma.

Table A.1: Change in moment of inertia at 10 Ma for a simulation using multiple time steps (MS) and for a simulation using one time step (OS) for the two-layer Earth model for a 400 km mesh resolution after 12 iterations.

ΔI_{ij}	Multiple steps [kg m^2]	One step [kg m^2]	|MS - OS| [%]
ΔI_{11}	-9.40888e34	-9.44616e34	0.39
ΔI_{22}	-9.56099e34	-9.55402e34	0.07
ΔI_{33}	1.88989e35	1.89315e35	0.17
ΔI_{12}	-7.61388e30	9.78621e27	77702.13
ΔI_{13}	1.00911e30	1.39023e31	1277.68
ΔI_{23}	-3.38240e30	1.42508e31	321.32

For the diagonal components of the inertia tensor there is not much difference between the multiple step and the one step approach. The percentages for the difference between the approaches for the off-diagonal components of the inertia tensor seem worrying. However, these are still numerical errors as they are supposed to be zero. The effect of these numerical errors of TPW is investigated in Test 7, along with the effect of the little deviations in the diagonal components. For now the one step approach is used as the diagonal components show good agreement and the off-diagonal components are still at least 3 orders of magnitude smaller than the theoretically non-zero diagonal components. Using one step from 0 to 10 Ma decreases the simulation time drastically from using multiple steps, because the displacements of the nodes are only evaluated per time step.

B

Appendix B

In this appendix the code is tested which transforms the input surface load to the change in moment of inertia of the load $\Delta \mathbf{I}_L$. The code transforms the grid which describes the ice height to the change in moment of inertia according to the procedure described in Section 4.2 and in Test 2. Figure B.1 presents the part of the code tested in the bigger scheme. The grid approach is tested for a point mass in Section B.1 and for a distributed mass in Section B.2.

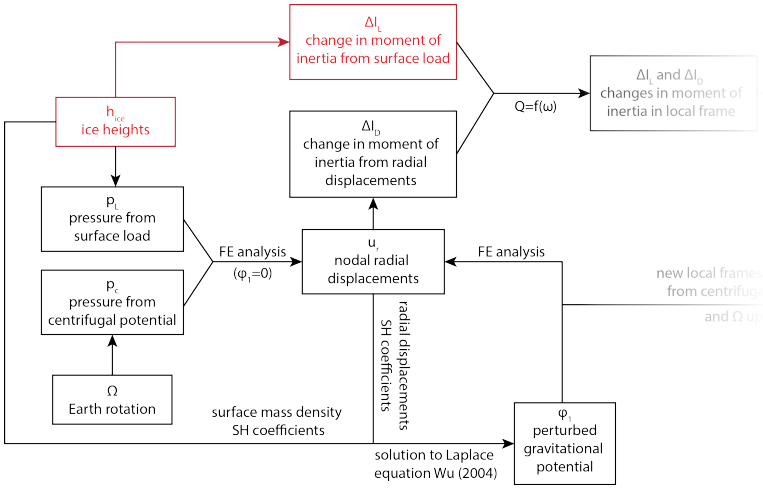

Figure B.1: Schematic overview of the parts of the code tested in Test B.1 and B.2 on the surface load to the change in moment of inertia from the load $\Delta \mathbf{I}_L$, for a point mass and distributed mass respectively.

B.1. Change in moment of inertia of a point mass

For the test on the change in moment of inertia from a point mass $\Delta \mathbf{I}_L$ a point mass is assumed with a mass M of $2{\cdot}10^{19}$ kg at 45° colatitude in the x-z plane, so 0° longitude. Analytically the change in moment of inertia from the point mass can be determined according to:

$$\begin{aligned} \Delta I_{L,11} &= M\left(y^2+z^2\right) & \Delta I_{L,12} &= -Mxy \\ \Delta I_{L,22} &= M\left(x^2+z^2\right) & \Delta I_{L,13} &= -Mxz \\ \Delta I_{L,33} &= M\left(x^2+y^2\right) & \Delta I_{L,23} &= -Myz \end{aligned} \tag{B.1}$$

in which x, y, and z are determined according to Equation 4.5. For the numerical model the input surface load has to be an ice height on a grid and therefore the point mass is converted to an ice height on a constant grid. For this approach one also needs to take into account the area of the grid cell, because the mass is a function of the ice height, ice density, and area of the grid cell. For a 2° grid the mass is divided over the two grid cells at 44° and 46° colatitude. However, the area of the grid cell is a function of latitude. The mass can be split in half and divided over the two grid cells, but because the area of the grid cells is different, the ice

height will be different as well. The grid cell areas A_i for this 2° constant grid can be determined as described in Subsection 3.2.7. The ice heights h for the two colatitudes can then be determined through:

$$\begin{aligned} M &= \rho_{ice} \sum_{i=1}^{2} h_i A_i \\ M_1 = M_2 &= \frac{M}{2} \qquad & h_1 &= \frac{M}{2\rho_{ice} A_1} \\ \rho_{ice} h_1 A_1 &= \rho_{ice} h_2 A_2 \qquad & h_2 &= \frac{M}{2\rho_{ice} A_2} \end{aligned} \tag{B.2}$$

in which the subscript 1 indicates the grid cell at 46° colatitude and the subscript 2 the grid cell at 44° colatitude. For a $2{\cdot}10^{19}$ kg point mass, the ice height at the grid point at 46° colatitude is ~304 km and at 44° colatitude ~314 km. The ice height at 46° colatitude is smaller because the grid cell areas are larger for grid cells closer to the equator. Table B.1 presents the change in moment of inertia of the input surface load for a point mass of $2{\cdot}10^{19}$ at 45° colatitude in the x-z plane, from the analytical approach and from the grid approach of the code.

Table B.1: Change in moment of inertia of the input surface load for a point mass of $2{\cdot}10^{19}$ at 45° colatitude in the x-z plane, from the analytical approach and from the grid approach of the code.

$\Delta I_{L,ij}$	Analytical approach [kg m^2]	Grid approach code [kg m^2]	|An. - Grid| [%]
$\Delta I_{L,11}$	4.058964e32	4.082136e32	0.57%
$\Delta I_{L,22}$	8.117928e32	8.164271e32	0.57%
$\Delta I_{L,33}$	4.058964e32	4.082136e32	0.57%
$\Delta I_{L,12}$	0	-4.999174e16	N/A
$\Delta I_{L,13}$	-4.058964e32	-4.079649e32	0.51%
$\Delta I_{L,23}$	0	4.996129e16	N/A

The grid approach change in moment of inertia of the surface load closely resembles the theoretically non-zero components, with only a 0.57% error maximum, for a 2° grid. The reason they do not match perfectly is because the point mass is divided over two grid cells. However, even for a 1° constant grid the grid points do not lie at the center of the grid cells, as can be seen in Figure 3.8, and thus the point mass does not lie exactly at 0° longitude. It is expected that for a finer grid, and when the grid point is assumed to lie at the center of the grid cell, the analytical changes in moment of inertia can be approximated even closer. The theoretically zero components of the inertia tensor are 16 orders of magnitude smaller than the other components. Also, their magnitude is much smaller than the numerical errors introduced in the off-diagonal components when the spherical model is in hydrostatic equilibrium as described in Section 6.2. Thus, the change in moment of inertia of the point mass $\Delta\mathbf{I}_L$ is determined with sufficient accuracy.

B.2. Change in moment of inertia of a distributed mass

Here the change in moment of inertia of the surface load is investigated for a realistic distributed mass as ice history. The change of moment of inertia of the ICE-3G ice history (Tushingham and Peltier, 1991) at the Last Glacial Maximum (LGM) minus the present day, as presented in Figure 6.9, is computed from the grid approach from the code and compared to an analytical approach from Milne and Mitrovica (1998) for the $\Delta I_{L,13}$, $\Delta I_{L,23}$, and $\Delta I_{L,33}$ components. Milne and Mitrovica (1998) gives the change in moment of inertia of an arbitrary surface load based on its spherical harmonics decomposition for the $\Delta I_{L,13}$, $\Delta I_{L,23}$, and $\Delta I_{L,33}$ components for when the sea load is not taken into account:

$$\Delta I_{L,13} = \frac{4}{3}\sqrt{\frac{6}{5}} a^4 \pi \rho_{ice} \Re(\bar{C}_{2,1}) \tag{B.3a}$$

$$\Delta I_{L,23} = \frac{4}{3}\sqrt{\frac{6}{5}} a^4 \pi \rho_{ice} \Im(\bar{C}_{2,1}) \tag{B.3b}$$

$$\Delta I_{L,33} = \frac{8}{3} a^4 \pi \rho_{ice} \left(\Re(\bar{C}_{0,0}) - \frac{1}{\sqrt{5}} \Re(\bar{C}_{2,0}) \right) \tag{B.3c}$$

in which $\Re(x)$ denotes the real part and $\Im(x)$ the imaginary part of x. These inertia tensor components can be compared to the ones from the grid approach used in the code. For the analytical approach the surface load is converted to spherical harmonic coefficients using the `SpherePy` package. However, the spherical harmonic coefficients these equations are based on, are different from the spherical harmonic coefficients from `Spherepy` because a different normalization technique is used. Milne and Mitrovica (1998) adopt the following normalization:

$$\oiint |Y_{l,m}(\theta,\lambda)|^2 d\Omega = 4\pi \tag{B.4a}$$

$$\iint_{\Omega} Y^*_{l',m'}(\theta,\lambda)\, Y_{l,m}(\theta,\lambda) \sin\theta d\theta d\lambda = 4\pi\delta_{l',l}\delta_{m',m} \tag{B.4b}$$

$$Y_{l,m}(\theta,\lambda) = \sqrt{2l+1\frac{(l-m)!}{(l+m)!}} P_{l,m}(\cos\theta)\, e^{im\lambda} \tag{B.4c}$$

in which $*$ denotes the complex conjugate. The `SpherePy` package adopts the following normalization:

$$\oiint |Y_{l,m}(\theta,\lambda)|^2 d\Omega = 1 \tag{B.5a}$$

$$\iint_{\Omega} Y^*_{l',m'}(\theta,\lambda)\, Y_{l,m}(\theta,\lambda) \sin\theta d\theta d\lambda = \delta_{l',l}\delta_{m',m} \tag{B.5b}$$

$$Y_{l,m}(\theta,\lambda) = \sqrt{\frac{2l+1}{4\pi}\frac{(l-m)!}{(l+m)!}} P_{l,m}(\cos\theta)\, e^{im\lambda} \tag{B.5c}$$

First the `SpherePy` package is used to find the spherical harmonic coefficients of the distributed ICE-3G surface load. To make the two approaches equivalent the spherical harmonic coefficients are multiplied with a factor $\sqrt{1/(4\pi)}$, coming from the difference in the normalization, before the coefficients are applied in Equation B.3. Table B.2 presents the change in moment of inertia for the $\Delta I_{L,13}$, $\Delta I_{L,23}$, and $\Delta I_{L,33}$ components, from the analytical approach (Milne and Mitrovica, 1998) and the grid approach of the code.

Table B.2: Change in moment of inertia of the input surface load for a distributed mass being the ICE-3G ice history (LGM-present day), from the analytical approach (Milne and Mitrovica, 1998) and from the grid approach of the code.

$\Delta I_{L,ij}$	Analytical approach [kg m^2]	Grid approach code [kg m^2]	|An. - Grid| [%]
$\Delta I_{L,13}$	4.866694e31	4.866754e31	0.00125%
$\Delta I_{L,23}$	-2.763478e32	-2.763513e32	0.00126%
$\Delta I_{L,33}$	3.173726e32	3.173766e32	0.00126%

The inertia tensor components results are very similar for the analytical approach from Milne and Mitrovica (1998) and for the grid approach in the code for a distributed mass. The part of the code which transforms the surface load into its change in moment of inertia $\Delta\mathbf{I}_L$, as presented in Figure B.1, functions properly.

For the spherical harmonic decomposition a maximum spherical harmonic degree of 180 is used. A maximum degree of 30 gives the same results because the coefficients of interest are of low degree, and because the distributed mass does not have very abrupt spatial ice height changes. It is also investigated that for a point mass, the changes in moment inertia of the load are equal to each other using the Milne and Mitrovica (1998) approach for a maximum spherical harmonic degree of 30 and of 180. The low degree coefficients are determined sufficiently accurate for these maximum spherical harmonic degree settings. However, the maximum spherical harmonic degree is of importance for the perturbed gravitational potential determination from the radial displacements using Equation 4.11, as is investigated in Appendix E.2, because then all coefficients are used and not only a few low degree coefficients.

C

Appendix C

C.1. Local coordinate systems implementation

This appendix covers the part of the code tested in which TPW feeds back into the numerical analysis by defining new local coordinate systems for each time step to which the centrifugal potential is applied. The new local coordinate systems for each time step is based on $\boldsymbol{\omega}$, as explained in step 6 of the TPW algorithm implementation in Subsection 5.5.2. For the definition of the local coordinate systems for each time step in `Abaqus` the origin, a point on the x-axis, and a point on y-axis need to be defined, with respect to the global coordinate system. As described in Subsection 5.5.2, the coordinate transformation matrix $\mathbf{Q}$ is used to find the x- y- and z-coordinates in the initial local coordinate system of the new x- and y-axis. Figure C.1 presents a schematic overview of the parts of the code tested.

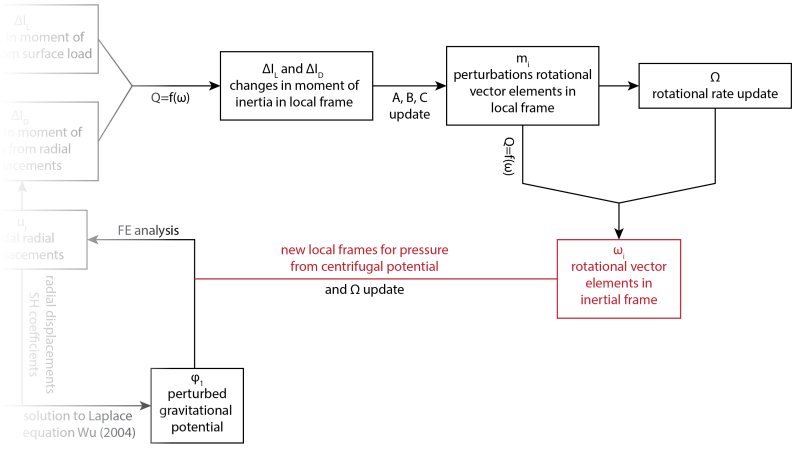

Figure C.1: Schematic overview of the parts of the code tested in Test C.1 on the implementation of the local coordinate systems for each time step to which the centrifugal potential is applied.

This part of the code will be tested with a forced movement of the rotational axis as in Test 1. However, now the movement of the rotational axis is not constrained to within a certain plane. The new local coordinate systems definition is based on the rotational vector and the coordinate transformation matrix $\mathbf{Q}$. The movement of the rotational axis is prescribed with 45° over 5000 years. The colatitude of the z-axis can be determined from the prescribed movement of the rotational axis. The elements of the rotational vector $\boldsymbol{\omega}$ are then determined through Equation 6.3.

The rotational vector elements are used to define the coordinate transformation matrix **Q**. The coordinates of the x- and y-axis in the initial local coordinate system, x' and y' respectively, are then determined using Equation 5.32 and 5.33, respectively. Note that for the coordinate system definition in `Abaqus` the point on the x- and y-axis need to be defined with respect to the global coordinate system, as presented in Figure 3.4. The local coordinate system can be defined with respect to the global coordinate system according to the following expressions:

$$\begin{aligned} \text{Origin:} \quad & (0,0,0) \\ \text{Point on the } x\text{-axis:} \quad & (x'_y(t), x'_z(t), x'_x(t)) \\ \text{Point on the } x\text{-}y \text{ plane:} \quad & (y'_y(t), y'_z(t), y'_x(t)) \end{aligned} \tag{C.1}$$

Figure C.2 presents the change in moment of inertia from the analytical approach and from the numerical approach using the local coordinate system implementation as in Test 1, and using the 'new' local coordinate system implementation based on $\boldsymbol{\omega}$ and **Q**. The time array is 'Time 1' as defined in Test 1. *Res* is set to 10, *Seeds* to 400 km, *Degree* to 45, and *CETOL* to 1e-5.

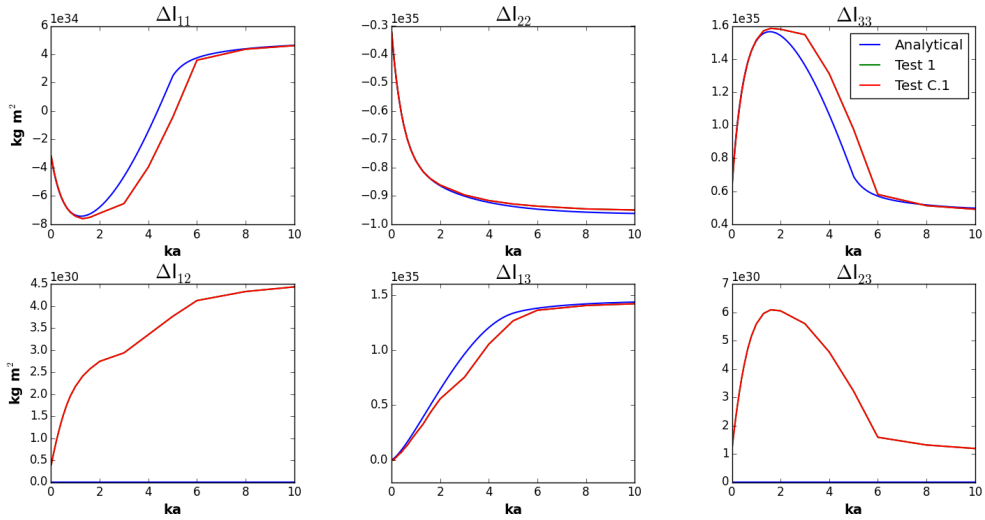

Figure C.2: Change in moment of inertia for a two-layer Earth model with the rotation axis drifting from 0° to 45° colatitude in the x-z plane over 5000 years with a constant speed with the analytical solution in blue, and the numerical solutions after 10 iterations using the original local coordinate system implementation in green, and the 'new' local coordinate system implementation in red.

As shown earlier in Test 1 the analytical solution is better approached with a finer time array. The two solutions for the different local coordinate system implementation overlay each other. Thus, it can be concluded that the coordinate transformation matrix correctly determines the axes positions per time step in the initial local coordinate system, and that the centrifugal potential is applied correctly to the new local coordinate systems per time step. Therefore, the part of the code in which the position of the rotational vector feeds back into the numerical model, for a new application of the centrifugal potential per time step, functions properly.

Appendix D

D.1. TPW sensitivity to mantle viscosity

This test investigates the effect of the mantle viscosity on the TPW prediction, to find whether the TPW path is according to expectations for a change in mantle viscosity. If so, then the difference in analytical and numerical TPW solution cannot be attributed to a wrongly modeled physical phenomenon. Stress relaxation is the decrease in stress in response to strain, deformation in terms of relative displacements, in the body. The viscosity has a direct effect on the relaxation time of the material, as shown in Equation 3.6 and repeated here for incompressible material, thus for $E = 3G$:

$$\tau_i^G = \frac{\mu}{G} = \frac{3\mu}{E} \tag{D.1}$$

For smaller mantle viscosities the relaxation time of the material becomes shorter, meaning that the stress in the body decreases faster for constant strain coming from the constant surface load, and a zero stress state is reached faster. In other words, a higher viscosity mantle material results in less displacements over a certain period of time. A higher mantle viscosity leads to smaller changes in $\Delta \mathbf{I}_D$, and thus in less TPW over that period of time. Figure D.1 present the TPW triggered by a $2{\cdot}10^{19}$ kg point mass at 0° longitude and 45° colatitude over 15 ka after 5 iterations for mantle viscosities of 1e20 Pa s, 1e21 Pa s, and 1e22 Pa s.

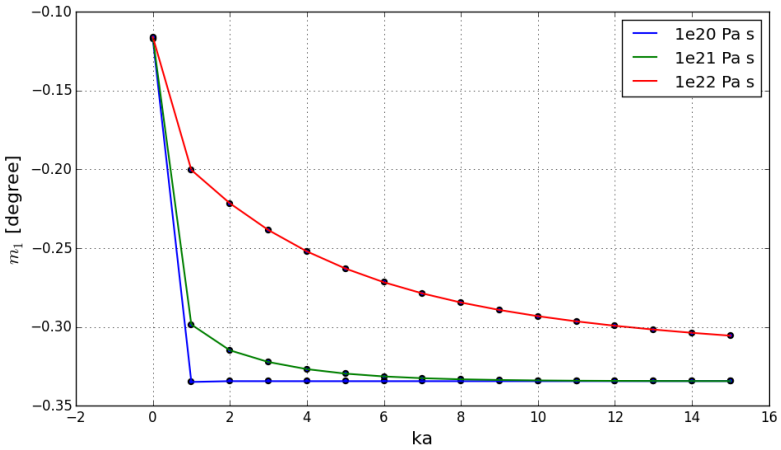

Figure D.1: TPW triggered by a $2{\cdot}10^{19}$ kg point mass at 0° longitude and 45° colatitude over 15 ka after 5 iteration for mantle viscosities of 1e20 Pa s, 1e21 Pa s, and 1e22 Pa s.

As can be shown the TPW is slower for higher mantle viscosities, as explained. Again, the TPW stops whilst it should continue for the constant load, further discussed in Test 9. However, regarding the mantle viscosities the TPW prediction is according to the expectations.

Appendix E

In this appendix the accuracy of TPW is investigated to the Earth's rotational rate update in the definition of the centrifugal potential in Section E.1, and to the maximum degree for the spherical harmonic decomposition of the surface load and radial displacements into their coefficients in Section E.2.

E.1. TPW accuracy to the Earth's rotational rate update

It has been stated that the change in the rotational rate from the change in length-of-day (LOD) determined from the norm of the perturbed rotational vector elements in the local frame, step 4 of the TPW algorithm implementation in Subsection 5.5.2, is a crucial step for the TPW solution to converge in terms of number of iterations for the radial displacement solution in the FE analysis. The new rotational vector needs to be normalized using the new rotational rate, as described by Equation 5.27 and 5.28. The TPW solution does not converge throughout the iterations when this step in the algorithm is not included. In this test is investigated whether updating the rotational rate Ω in the definition of the centrifugal potential has an effect on TPW. Figure E.1 presents the TPW triggered by a $2{\cdot}10^{19}$ kg point mass at 0° longitude and 45° colatitude over 5 ka for 5 iterations for a constant Ω on the left and for an updated Ω on the right for the centrifugal potential definition.

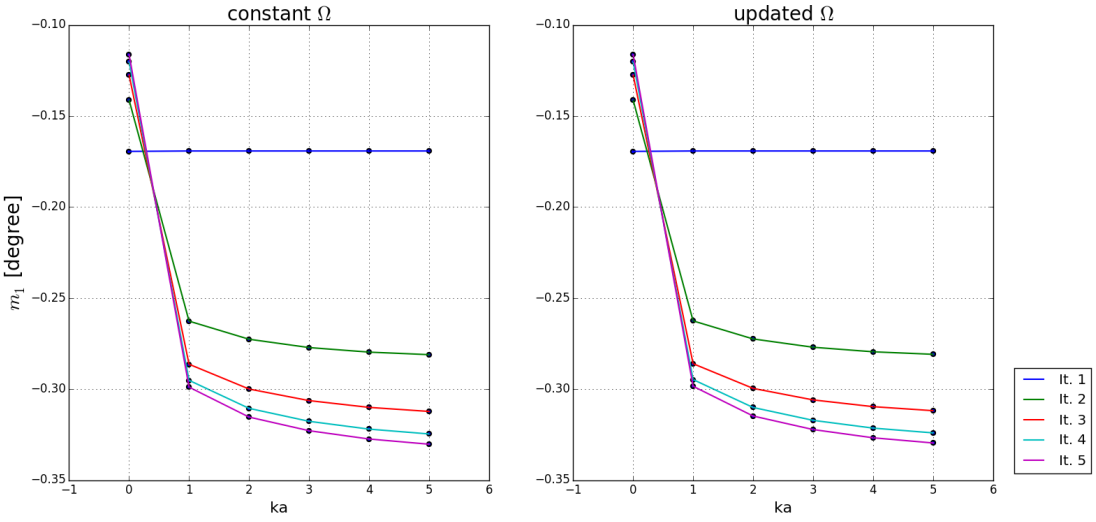

Figure E.1: TPW triggered by a $2{\cdot}10^{19}$ kg point mass at 0° longitude and 45° colatitude over 5 ka for 5 iterations for a constant Ω and updated Ω for the centrifugal potential definition.

As expected there is no large difference in TPW for both cases. The changes in rotational rate are very small and will therefore not significantly change the magnitude of the centrifugal potential. Thus there will be no large differences in radial displacements of the body, no significant difference in $\Delta\mathbf{I}_{D,c}$ and thus no significant difference in TPW. For iteration 5 at 5 ka m_1 differs with 0.21% between the two cases. One can imagine that when looking at longer time periods the TPW solutions may differ from one another and thus it is important to update the rotational rate in the definition of the centrifugal potential. However, for Test 7 it can be concluded that the difference in TPW paths between 7-1 and 7-3 comes from the direct effect of $\boldsymbol{\omega}$ on the new local coordinate systems definition and not from the new centrifugal potential magnitude.

E.2. TPW accuracy to maximum spherical harmonic degree

In this test is investigated what the effect is of the spherical harmonic decomposition of the surface load into its coefficients on TPW. In Test 2 is found that the change in moment of inertia of the deformations due to a surface load $\Delta\mathbf{I}_{D,L}$ did not change with maximum spherical harmonic degrees of 30, 45, and 100 for the spherical ice cap as surface load. However, for a surface load which spatially changes not as smoothly as the spherical ice cap, such as a point mass, the maximum spherical harmonic degree may have an effect on the solution. When $\Delta\mathbf{I}_{D,L}$ is affected, TPW will be affected as well. The deformation due to the surface load is not taken into account here. The focus here is on the TPW accuracy to the maximum spherical harmonic degree when the surface load is taken into account in the equations for the perturbed gravitational potential in the form of the spherical harmonic coefficients of the surface mass density $\sigma_{l,m}$. Here, an extreme case is considered, a point mass, because it spatially changes very abruptly over the grid. Before investigating the TPW, first the $2{\cdot}10^{19}$ kg point mass at 0° longitude and 45° colatitude on a 1° grid is converted to its coefficients and back to the spatial domain using the `SpherePy` package. Figure E.2 presents the spatial signal of the point mass after it is converted back to the spatial domain using a maximum degree of 45, 90, and 180.

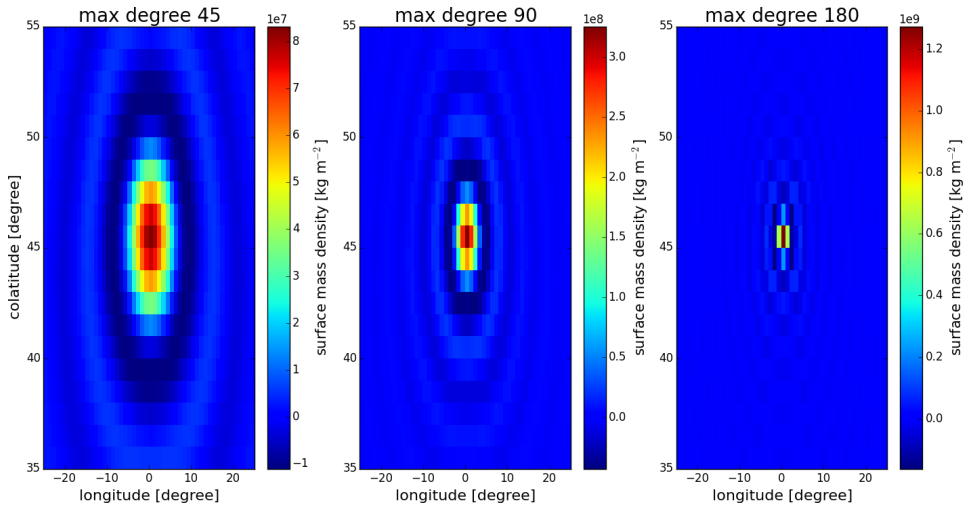

Figure E.2: The spatial signal of a $2{\cdot}10^{19}$ kg point mass at 0° longitude and 45° colatitude on a 1° grid converted to spherical harmonic coefficients and back to the spatial domain using a maximum degree of 45, 90, and 180.

Note that the colorbar range for each of the plots is different. A higher maximum degree is much better at capturing the signal. Also, for a higher degree there is less signal leakage to other coefficients in the spectral domain, and thus less leakage to other grid points in the spatial domain. The spherical harmonic coefficients of the surface mass density $\sigma_{l,m}$ are used in the definition of the perturbed gravitational potential as presented in Equation 4.11 (Wu, 2004). Now it is investigated what the effect of the accuracy of the surface load decomposition into its spherical harmonic coefficients is on TPW. For this test the TPW paths for a maximum degree of 45 and of 180 are compared. Note that also the radial displacements are decomposed into their coefficients $U_{l,m}$ according to the same maximum degree as is defined for the surface mass density. Figure E.3 presents the TPW triggered by the point mass over 5 ka for 5 iterations for a maximum spherical harmonic degree of 45 and 180 for the surface mass density.

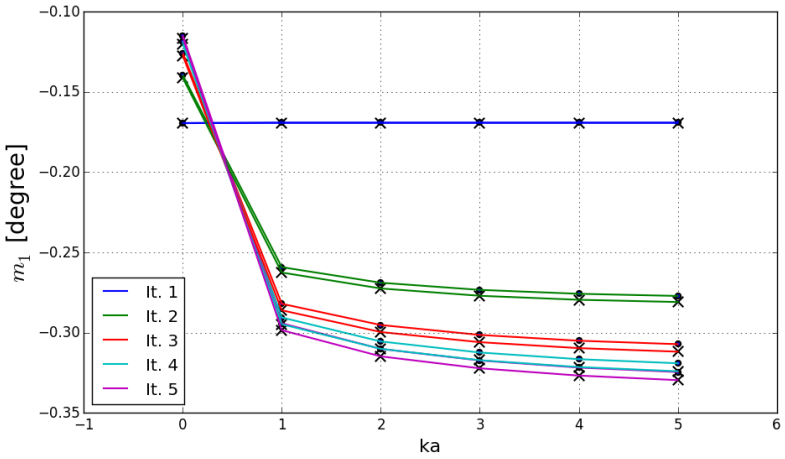

Figure E.3: TPW triggered by a $2{\cdot}10^{19}$ kg point mass at 0° longitude and 45° colatitude over 5 ka for 5 iterations for a maximum spherical harmonic degree of 45 (crosses) and 180 (dots) for the surface mass density in the perturbed gravitational potential definition.

The crosses and dots indicate the TPW solution for when a maximum spherical harmonic degree of 45 and 180 is used, respectively. The TPW solution is overestimated with a lower maximum degree by 1-2% after 5 iterations. By using a higher maximum degree for the spherical harmonic decomposition of the surface mass density and the radial displacements, the accuracy of the solution increases. It seems as if the error between the two solution does not increase over time and thus it is safe to perform tests with a maximum degree of 45. However, for a more accurate TPW prediction a higher maximum degree is required.